Wave Propagation in Thin-walled Composite Structures: Application to Structural Health Monitoring

Wave Propagation in Thin-walled Composite Structures: Application to Structural Health Monitoring

PROEFSCHRIFT

ter verkrijging van de graad van doctor
aan de Technische Universiteit Delft,
op gezag van de Rector Magnificus prof. ir. K.C.A.M. Luyben,
voorzitter van het College voor Promoties,
in het openbaar te verdedigen op donderdag 20 december 2012 om 15:00 uur
door

Lotfollah Pooria Pahlavan

master of science in Mechanical Engineering,
Ferdowsi University of Mashhad, Iran
geboren te Mashhad, Iran

Dit proefschrift is goedgekeurd door de promoter:

Prof. dr. Z. Gürdal

Samenstelling promotiecommissie:

Rector Magnificus:	Voorzitter
Prof. dr. Z. Gürdal	Technische Universiteit Delft, promotor
Dr. C. Kassapoglou	Technische Universiteit Delft, copromotor
Prof. dr. V. Giurgiutiu	University of South Carolina
Prof. dr. I.E. Elishakoff	Florida Atlantic University
Prof. dr. A. de Boer	University of Twente
Prof. dr. A. Metrikine	Technische Universiteit Delft
Dr. A.W.F. Volker	Nederlandse Organisatie voor Toegepast Natuurwetenschappelijk Onderzoek
Prof. dr. Ir. L.J. Sluys	Technische Universiteit Delft, reservelid

Keywords: composite materials, guided waves, ultrasonics, structural health monitoring, wavelets, wavelet-Galerkin, time reversal, damage detection

ISBN 978-94-6203-267-5

برخیز و مخور غم جهان گذران
خوش باش و دمی به شادمانی گذران
در طبع جهان اگر وفایی بودی
نوبت به تو خود نیامدی از دگران

رباعیات خیام

Get up and forget the cares of the ephemeral world,
Enjoy yourself and spend your brief moment in fun,
For if the world were faithful by nature,
Your turn would not come before others.

Rubaiyat of Omar Khayyäm
Tanslated by K. Emami

Summary

In order for the increased use of fiber-reinforced composite structures to be financially feasible, employment of reliable and economical systems to detect damage and evaluate structural integrity is necessary. This task has traditionally been performed using off-line non-destructive testing (NDT) techniques. Safety enhancement programs and cost minimization schemes for repairs, however, have substantially increased the demand for real time integrity monitoring systems, i.e. *structural health monitoring* (SHM) systems in the past few years. The real time feature imposes an additional constraint on SHM systems to be fast and computationally efficient. Among the existing approaches fulfilling these requirements, guided ultrasonic wave (GUW)-based methods are of particular interest, since they provide the possibility of finding small size defects, both at the surface and internal, and covering relatively large areas with reasonable hardware costs. Next to theses appealing features, there are certain complexities in utilizing GUWs for SHM of fiber-reinforced composites, that mainly arise from the multi-layer, anisotropic, and non-homogeneous nature of the material. In addition, the multi-mode character of GUWs further increases the complexity of the SHM problem in these materials. It is believed that computationally efficient methods for simulation of GUWs in composite structures can substantially contribute to the field of SHM. Such numerical tools do not only improve the understanding of the propagation of ultrasonic waves and their interaction with different damage types and boundary conditions, but can also make model-based damage identification techniques feasible in the context of on-line SHM.

In this dissertation an improved framework for simulation of GUWs in composite structures is developed. The improvements are mainly brought about through the use of (i) physical constraints that reduces the dimensionality of the problem, (ii) improved approximation bases for spatial and temporal discretization of the governing equations, and (iii) efficient mathematical tools to enable the possibility of parallel computation. The formulated approach is a wavelet-based spectral finite element method (WSFEM), which offers the possibility of complete decoupling of the spatial and temporal discretization schemes, and results in parallel implementation of the temporal solution. Although the concept of the WSFEM was introduced a few years prior to this research, to the author's best knowledge, no general framework was proposed for dealing with 2D and 3D problems with inhomogeneity, anisotropy, geometrical com-

plexity, and arbitrary boundary conditions. These issues are addressed in this dissertation in multiple steps as described below.

1. Improvement of the temporal discretization using compactly-supported wavelets, by computing the operators of the wavelet-Galerkin method over finite intervals, and demonstrating about 50% reduction in the number of sampling points, with the same accuracy, compared to the conventional wavelet-based approach.

2. Extension of the existing formulation of the 1D WSFEM based on an in-plane displacement field to 1D waveguides based on a 3D displacement field. In the 1D finite element formulation, spectral shape functions are employed which satisfy the governing equations, in which shear deformation and thickness contraction effects are also incorporated. The minimum number of elements for modeling 1D waveguides is used in this approach.

3. Formulation of a novel 2D WSFEM in which frequency-dependent basis functions are suggested for spatial discretization. Contrary to the conventional WSFEM, the presented scheme discretizes the spatial domain with 2D elements and does not require extra treatments for non-periodic boundary conditions. Superior properties of the formulation are shown in comparison with some time domain FEM schemes.

4. Generalization of the WSFEM and extension to 3D geometries. It is demonstrated that the standard spatial discretization schemes can be combined with the wavelet-Galerkin approach, to fully parallelize the temporal solution. A higher-order pseudo-spectral finite element method, i.e. spectral element method (SEM), is further adopted to attain spectral convergence properties over space and time.

The developed WSFEM is subsequently employed in the passive time reversal (TR) method, which is a model-based approach for detection of load and damage location, and operates based on the time invariance of linear elastodynamic equations. It is shown that using the passive TR scheme, the problem of load and damage detection, which is essentially an inverse problem, can be solved in the form of a forward problem, thereby alleviating uniqueness and stability issues. A number of case studies and examples, numerical and experimental, are presented throughout this dissertation to better demonstrate the applicability of the proposed framework.

Samenvating

Teneinde het toegenomen gebruik van vezelversterkte composieten financieel haalbaar te doen zijn, is de beschikbaarheid van betrouwbare en economische systemen om schade te detecteren en het beoordelen van de structurele integriteit noodzakelijk. Deze taak wordt traditioneel uitgevoerd met behulp van technieken voor off-line niet-destructief onderzoek (NDT). Veiligheidsverhogingsprogramma's en overwegeningen van kostenminimalisatie van reparaties hebben echter de vraag naar real-time integriteit monitoring systemen, i.e. *structural health monitoring* (SHM) systemen, aanzienlijk doen toenemen in de afgelopen jaren. De real-time functie legt een extra beperking op aan SHM-systemen om snel en computationeel efficiënt te zijn. Onder de bestaande benaderingen die aan deze eisen tegemoetkomen, zijn methoden gebaseerd op geleide ultrasone golf (GUW) van bijzonder belang, aangezien zij voorzien in de mogelijkheid van het vinden van kleine defecten (zowel aan de oppervlakte als intern) en dekking van relatief grote gebieden met redelijke hardware kosten. Naast deze aantrekkelijke functies is er een zekere complexiteit in het gebruik van GUW's voor SHM van vezelversterkte composieten, die voornamelijk voortkomt uit het multi-layer, anisotroop, en niet-homogene karakter van het materiaal. Bovendien verhoogt het multi-mode karakter van GUW's de complexiteit van het SHM probleem in deze materialen. Er wordt aangenomen dat rekentechnisch efficiënte methoden voor simulatie van GUW's in composietstructuren substantieel kan bijdragen aan het gebied van SHM. Dergelijke numerieke tools verbeteren niet alleen het begrip van de voortplanting van ultrasone golven en hun interactie met verschillende soorten schade en randvoorwaarden, maar kunnen ook het gebruik van model-gebaseerde schade-identificatietechnieken mogelijk maken in het kader van on-line SHM.

In dit proefschrift wordt een verbeterd kader voor de simulatie van GUW's in composietstructuren ontwikkeld. De verbeteringen worden voornamelijk bereikt door het gebruik van (i) fysieke constraints dat de dimensionaliteit van het probleem kan verminderen, (ii) verbeterde approximatiebases voor ruimtelijke en tijd-discretisatie van de vergelijkingen, en (iii) efficiënte mathematische technieken die de mogelijkheid van parallelle berekening bieden. De geformuleerde benadering is een op wavelets gebaseerde spectrale eindige-elementenmethode (WSFEM) die de mogelijkheid biedt van volledige ontkoppeling van de ruimtelijke en tijd-discretisatie schema's, en parallelle uitvoering van de temporele oplossing. Hoewel het concept van de WSFEM geïntroduceerd werd in de jaren vooraf-

gaand aan dit onderzoek, werd er naar beste weten van de auteur geen algemeen kader voorgesteld voor 2D en 3D problemen met inhomogeniteit, anisotropie, geometrische complexiteit, en willekeurige randvoorwaarden. Deze issues worden behandeld in dit proefschrift in meerdere stappen zoals hieronder beschreven.

1. Verbetering van de tijd-discretisatie met behulp van compactly-supported wavelets, door het berekenen van de operatoren van de wavelet-Galerkin methode over eindige intervallen en leidend tot ongeveer 50% vermindering van het aantal bemonsteringspunten, met dezelfde nauwkeurigheid in vergelijking met de conventionele benadering.

2. Uitbreiding van de bestaande formulering van de 1D WSFEM gebaseerd op een in-plane verplaatsingsveld tot 1D golfgeleiders gebaseerd op een 3D verplaatsingsveld: in de 1D eindige-elementenformulering worden spectrale vormfuncties gebruikt die voldoen aan de vergelijkingen waarin effecten van afschuiving en dikte-krimp ook worden opgenomen. Het minimum aantal elementen voor het modelleren van 1D golfgeleiders wordt gebruikt in deze benadering.

3. Formulering van een nieuw 2D WSFEM waarin frequentie-afhankelijke basisfuncties worden voorgesteld voor ruimtelijke discretisatie: anders dan conventionele WSFEM discretiseert de onderzoeksmethode het ruimtelijke domein met 2D elementen en heeft geen extra behandelingen nodig voor niet-periodieke randvoorwaarden. De superieure eigenschappen van de formulering worden aangetoond in vergelijking met een tijdsdomein FEM-schema.

4. Generalisatie van de WSFEM en uitbreiding naar 3D configuraties: er wordt aangetoond dat de standaard ruimtelijke schema's gecombineerd kunnen worden met de wavelet-Galerkin methode om de temporele oplossing volledig te parallelliseren. Een hogere-orde pseudo-spectrale eindige-elementenmethode, i.e. spectrale elementenmethode (SEM), wordt verder aangepast om spectrale convergentie-eigenschappen te bereiken in ruimte en tijd.

De ontwikkelde WSFEM wordt vervolgens gebruikt in de methode van passieve tijdsomkering (TR), die een model-gebaseerde benadering is voor de detectie van de locatie van de belasting en de schade, en werkt op basis van de tijdinvariantie van lineaire elastodynamische vergelijkingen. Er wordt aangetoond met de behulp van het passieve TR schema, dat het probleem van belasting- en defectlocalizatie dat in wezen een inverse probleem is, kan worden opgelost in de vorm van een voorwaarts probleem, waardoor het verlichten van uniciteit en stabiliteitsissues bereikt wordt. Een aantal case studies en voorbeelden, numerieke en experimentele, worden gepresenteerd in dit proefschrift om de toepasselijkheid van het voorgestelde kader beter aan te tonen .

Acknowledgements

During a period of three and a half years, from August 2008 till February 2012, that I served as a PhD researcher at the department of Aerospace Structures and Computational Mechanics of TU Delft, I tried to contribute in the area of structural health monitoring (SHM) of thin-walled composite structures using guided ultrasonic waves, and I hope my research has provided some improved computational aspects for modeling ultrasonic waves in anisotropic and heterogeneous media with potential applications in real SHM systems. On my way to this point, I was honored to have a lovely wife "Laleh", my family, friends, colleagues, and not the least, supervisors who helped me directly and/or indirectly to finish the journey, and gain invaluable experiences that I will carry with me for a lifetime. The fear of missing out names and not properly saying what I am thankful for, however, left me the single choice of only mentioning a few people who had a very direct impact on my thesis. This, certainly, does not mean any lower degree of importance for the supports that I failed to mention here, and I hope this excuse is generously accepted by all those people whom I am indebted to for being so supportive and patient in my hard times, for the time that they spent listening to me, and for the inspiration that they gave me, without which it would have been almost impossible to get to this point. With my most sincere feelings, this book is dedicated to them.

Next, I would like to acknowledge a number of people who devoted priceless time and effort to helping me improve the quality of my PhD research and thesis. What follows is not necessarily in order of importance.

Christos Kassapoglou: every minute of talking to you has always been, and still is, the best lesson on communication, morality, professionalism, and indeed composite materials! that I could ever attend. In the moments of frustration, you were the first one that I always turned to, and you always, with your incredible understanding of cultural/personal matters, showed me the origin of and the solution to the problem. Besides the technical supervision of my PhD work, you helped me grow up and become a better person in my professional and personal life, and for this I will always be indebted to you.

Zafer Gürdal: I am grateful for all your support and supervision during my PhD. I know that I was probably not the easiest student to deal with and when I look back, I admit that I was sometimes too stubborn, mainly due to the lack of experience. However, you always magnanimously and patiently gave me the opportunity of learning by experiment. I will never forget this and hope that I

deserved the chance given. I am honored to be your student.

In addition to the above, there is a group of people to whom I am grateful: Eelco Janssen and Akke Suiker for being co-supervisors in different periods of my PhD and helping me to improve the scientific level of my research, J.N. Reddy for his valuable feedbacks and suggestions to improve the formulation of my wavelet-based finite element method, Victor Giurgiutiu for his constructive and insightful comments on the work in several stages during my PhD, members of the promotion committee for their kind support and help in bringing up the quality of this book, Miranda Aldham-Breary for teaching me how to get my Engish to read and sound like English, Jan Gerbrands for helping me to translate my propositions and summary into Dutch, and Ardavan Khorsand for designing the cover of the book. My heartfelt thanks.

Pooria

Contents

List of Figures

Nomenclature

Abbreviations

nD	n-dimensional, n=1,2,3
CWT	Continuous wavelet transform
DFT	Discrete Fourier transform
DOFs	Degrees of freedom
DWG	Decoupled wavelet-Galerkin method
DWT	Discrete wavelet transform
FEM	Finite element method
FEM-L	FEM with linear basis functions
FEM-L	FEM with quadratic basis functions
FFT	Fast Fourier transform
FSDT	First-order shear deformation theory
FSFEM	Fourier-based spectral finite element method
GLL	Gauss-Lobatto-Legendre
GUWs	Guided ultrasonic waves
MRA	Multi-resolution analysis
NDT	Non-destructive testing
ODE	Ordinary differential equation
PDE	Partial differential equation
RMS	Root mean square
SEM	Spectral element method

SHM	Structural health monitoring
SNR	Signal-to-noise ratio
TD	Time domain
TOF	Time of flight
TR	Time reversal
WGM	Wavelet-Galerkin method
WSFEM	Wavelet-based spectral finite element method

Greek Letters

$\boldsymbol{\epsilon}$	Strain tensor
$\boldsymbol{\Gamma}_n$	nth-order connection coefficient matrix of wavelets
$\boldsymbol{\sigma}$	Stress tensor
δ_{ij}	Kronecker delta
Γ_j^n	jth connection coefficients of order n of wavelets
ν_{ij}	Poisson's ratio, i, j=1,2,3
Ω	Physical domain
ω	Fourier frequency
Ω_e	Element domain
ψ	Wavelet function
$\psi_{j,k}$	Translated and scaled wavelet function
ρ	Material density
φ	Scaling function of wavelets
$\varphi_{j,k}$	Translated and dialated scaling function of wavelets
$\bar{\omega}_j$	Wavelet frequency at the jth wavelet point

Roman Letters

$\bar{\mathbf{f}}_j$	Wavelet-transformed external force vector at the jth wavelet point
$\bar{\mathbf{K}}_j$	Dynamic stiffness matrix at the jth wavelet point
$\bar{\mathbf{q}}_j$	Wavelet-transformed global nodal displacement vector at the jth wavelet point

$\bar{\mathbf{u}}_j$	Wavelet-transformed dependent variables at the jth wavelet point
$\mathbf{q}$	Global nodal displacement vector in the time domain
$\mathbf{u}$	Dependent variables in the time domain
$\mathbf{C}$	Material stiffness matrix
$\hat{\mathbf{u}}$	Dependent variables in the space of approximation coefficients
$\hat{f}_k$	kth approximation coefficient of temporally-discretized function f
τ	Dimensionless time
A_{ij}	Laminate in-plane stiffness coefficients, $i, j = 1, 2, ..., 6$
B_{ij}	Laminate bending-extension coupling stiffness coefficients, $i, j = 1, 2, ..., 6$
c_g	Group velocity
c_p	Phase velocity
C_{ij}	Stiffness coefficient, i, j=1,2,...,6
D_{ij}	Laminate bending stiffness coefficients, $i, j = 1, 2, ..., 6$
E_i	Young's modulus, i=1,2,3
G_{ij}	Shear modulus, i, j=1,2,3
h	Thickness
I_i^η	ith moment of inertia about η-axis
K	Curvature
k_η^n	Wavenumber in $\eta-$ direction at the nth transformed domain point
L	Number of temporal sampling points
N	Wavelet order
N_η	SEM order in η-direction
R	Radius
t	time
u	Displacement in x-direction
v	Displacement in y-direction
w	Displacement in z-direction

$\mathbf{q}^e$	Nodal displacement vector at the element level in the time domain
$\mathbf{f}$	External forces in the time domain
$\mathbf{K}$	Global stiffness matrix
$\mathbf{M}$	Global mass matrix

Other Symbols

Δt	Time step size
$\mathbb{R}$	Set of real numbers
$\mathbb{R}^+$	Set of positive real numbers
$\mathbb{Z}$	Set of integer numbers
Ai	Anti-symmetric Lamb waves of mode i, $i = 1, 2, 3, ...$
A0	Fundamental anti-symmetric guided waves
P-waves	Pressure waves
Si	Symmetric Lamb waves of mode i, $i = 1, 2, 3, ...$
S-waves	Shear waves
S0	Fundamental symmetric guided waves
SHi	Shear-horizontal waves of mode i, $i = 1, 2, 3, ...$
SH0	Fundamental shear-horizontal waves

Chapter 1

Introduction

Autonomous systems which can evaluate structural integrity in real time are known as structural health monitoring (SHM) systems [Staszewski et al., 2004, Giurgiutiu, 2008, Boller et al., 2009, Balageas et al., 2006]. The primary objectives of SHM systems, in general, are reducing the cost of maintenance and repairs, and most importantly in the context of transportation, improving safety. These objectives are mainly achieved by detection of structural defects at an early stage, and monitoring the load history applied on the structure [Staszewski et al., 2004]. The cost-saving potential of SHM systems deals with reducing (i) the direct costs, e.g. design and fabrication of repairs, and (ii) the indirect costs induced by implementation of repairs for which the system has to be taken out of service [Staszewski et al., 2004]. Structural health monitoring systems may ideally replace scheduled maintenance programs with as-needed maintenance schemes [Giurgiutiu, 2008, Boller, 2000] to reduce the indirect costs.

Traditionally, non-destructive testing (NDT) techniques have been used for monitoring structural integrity of metallic and composite structures [Adams et al., 1986, Cawley, 1985, Summerscales, 1990, Blitz and Simpson, 1996]. When similar operations are implemented in an unmanned fashion with permanently-installed sensors and actuators, the integrity evaluation technique falls into the category of structural health monitoring [Giurgiutiu, 2008]. Since SHM systems are meant to work in an online fashion, they should meet additional requirements compared to NDT systems, such as a short processing time. During the operation, structures are interrogated by SHM systems, to transfer the information required to assess the structural integrity.

Structural health monitoring can be generally performed in two main ways; passive SHM, and active SHM [Giurgiutiu, 2008]. In passive SHM, there is a one-way communication between the structure and the SHM system: the SHM system only listens to the structure and uses an external model, e.g. numerical or statistical, to evaluate structural integrity. Active SHM systems however, listen and talk to the structure to directly examine if/how the structure has been damaged. Different levels of SHM methods can be distinguished based on the information that the SHM system can provide about the existence of the

damage, extent of the damage, location of the damage, and remaining life of the structure [Boller, 2000].

1.1 SHM of Composite Structures

In order for the increased use of fiber-reinforced composite structures to be financially feasible, development of reliable, efficient, and economical SHM systems to detect and evaluate damage is necessary. Structural health monitoring of composites is generally a more challenging issue than SHM of metallic structures. The challenge can be ascribed to the complexity in the mechanical behavior of fiber-reinforced composites in comparison with metallic structures, e.g. anisotropy and multi-layer structure, and also barely-visible to non-visible delaminations, which may, at their current or a later stage, adversely affect the mechanical properties of the structures [Su and Ye, 2009, Summerscales, 1990]. Since impact is a major source of delamination initiation in composites, the importance of load history monitoring is also more pronounced in the SHM of composite structures than in metals.

1.2 Components of SHM Systems

Structural health monitoring systems work based on the fact that damage changes the mechanical or electromechanical properties of structures. Every SHM system, regardless of the physical principle based on which it operates, is generally composed of a number of components. These components, as shown in Figure 1.1, are data acquisition parts, signal processing tools, forward models, i.e. predictive models, and identification algorithms. Depending on the type of the SHM tool, each of these components may gain a higher or a lower significance than the others.

In an SHM system, data needs to be gathered from the actual hardware at the first step using a data acquisition system. Next, the signals, which are often contaminated with noise, need to be processed carefully. Certain features may have to be extracted from the signals in the signal processing package. Furthermore, a predictive model can be used to (i) improve the understating of the user in correlating the obtained data to possible structural defects, and (ii) improve the design and optimization of the SHM hardware, e.g. location of the sensors and actuators. The damage identification part, which can be model-based, or based on signal processing approaches, is finally used to identify defects or history of external loads. For quantitative assessment of structural integrity, the use of model-based approaches is rapidly growing, which signifies the importance of accurate and computationally-efficient forward models.

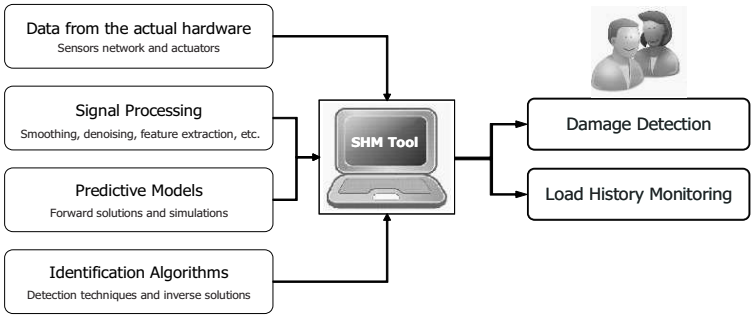

Figure 1.1: Schematic view of an SHM system.

1.3 SHM Methods

Structural health monitoring methods can be classified based upon the physical principle behind the SHM methodology. The most extensively-used SHM approaches are based on modal data, electro-mechanical impedance, static measurement, acoustic emission, and elastic waves. Su and Ye [2009] have provided a concise description of each method along with its applications, merits, and limitations, as listed in Table 1.1 on Page 6. For a detailed review of these methods, the reader is referred to Staszewski et al. [2004], Balageas et al. [2006], Boller et al. [2009].

1.4 Motivation

Among the well-established SHM methodologies listed in Table 1.1, the elastic wave-based SHM has gained a special attention in the past decade based on its merits: being cost-effective, fast and repeatable, able to inspect a large area in a short time, sensitive to small damage, no need for motion of transducers, low energy consumption, and able to detect both surface and internal damage [Su and Ye, 2009]. For thin-walled structures, since the frequency of the diagnostic waves, which are guided by the free surfaces of the structure, lie in the ultrasonic regime, these waves are often referred to as guided ultrasonic waves (GUWs). Although GUWs are efficient tools for evaluation of structural integrity, certain complexities exist in implementation of GUW-based SHM systems, as listed in Table 1.1. One of these major complexities is interpretation of the signals gathered from the experiment. The complexity mainly comes from the multi-layer structure, anisotropy, and possible non-homogeneity of advanced composite structures, which cannot be readily dealt with in many conventional NDT techniques.

Proper understanding of the underlying physics of GUWs in composite thin-walled structures, based on which signal processing tools and the identification scheme can also be enhanced, may be achieved using numerical models. Extensive studies have been carried out on modeling the GUWs, e.g. Doyle [1989],

Gopalakrishnan et al. [2008], Gaul et al. [2003], Delsanto et al. [1992], Ha and Chang [2010], Hong and Kennett [2002a], Zhang et al. [2006]. The commonly-used methods however, often require intensive computations for typical elastic wave problems in composite structures, or are inflexible in dealing with geometrical and material complexities. For example, finite element tools using first- and second-order elements and an explicit Newmark time integration scheme for wave propagation problems, often suffer from a low convergence rate due to the low quality of the approximation functions. Furthermore, mesh refinement, even locally at a damaged zone, adversely influences the time step size and further increases the solution time, see Gopalakrishnan et al. [2008] and Chapter 2 of this thesis for more elaborate discussions. Despite the fact that any method serving sufficient accuracy can be used in design of SHM systems, lack of computational efficiency remains an obstacle for the growth of model-assisted SHM methods for composite structures. It is believed that certain improvements in computational efficiency of simulation of GUWs can be still brought about. These improvements can be applied through (i) using more physical constraints to reduce the dimensions of the problem while still providing the desirable accuracy, and (ii) using efficient mathematical tools and techniques which can enable us to use the available computational resources more effectively, e.g. parallel computation.

The focus of the developments in this dissertation is on a computationally-efficient method, namely the wavelet-based spectral finite element method (WSFEM) which offers the possibility of complete decoupling of the spatial and temporal discretization schemes, and parallel implementation of the solution. Despite the notable progress so far in formulating the WSFEM as reported in Gopalakrishnan and Mitra [2010] , there are still difficulties in dealing with 2D and 3D problems with inhomogeneity, anisotropy, geometrical complexity, and arbitrary boundary conditions, solutions to which are addressed in this dissertation.

1.5 Scope of the Thesis

The main contribution of this dissertation is improvement/development of the WSFEM for simulation of GUWs in 1D, 2D, and 3D structures, and their applications to SHM. In Chapter 2, some background knowledge in GUWs-based SHM is presented. Chapter 3 is devoted to the mathematical foundation of compactly-supported wavelets, multiresolution analysis, and the wavelet-Galerkin method for spectral analysis of wave equations. The WSFEM is formulated for simulation of GUWs in 1D waveguides in Chapter 4. The Wavelet-Galerkin method is used for temporal discretization of the governing equations, whereas a finite element discretization of the spatial domain is carried out with spectral shape functions extracted from the waveguide characteristics of the structure. Chapter 5 deals with the extension of the formulation of the WSFEM to 2D waveguides. In the proposed approach, contrary to the conventional spectral methods, the problem is discretized with 2D elements the basis func-

tions of which are functions of the corresponding wavenumbers in the wavelet-transformed domain. Generalization of the WSFEM and extension to arbitrary 3D waveguides is presented in Chapter 6, where it is demonstrated that any standard FEM can be adopted in the WSFEM for spatial discretization. In Chapter 7, a model-based SHM methodology, i.e. the passive time reversal, is implemented in which the models developed in chapters 4, 5, and 6 are employed in damage/load location monitoring applications. Finally, conclusions and some recommendations for the future research are presented in Chapter 8.

Table 1.1: A review of commonly-used SHM methods [Su and Ye, 2009].

Approach	**Mechanism**	**Merits and applications**	**Demerits and limitations**
Modal-data-based (eigen-frequency, mode shape and curvature, strain energy, flexibility, sensitivity, damping properties, etc.)	Presence of structural damage reduces structural stiffness, shifts eigen-frequencies, and changes frequency response function and mode shapes.	Simple and low cost; particularly effective for detecting large damage in large infrastructure or rotating machinery.	Insensitive to small damage or damage growth; difficult to excite high frequencies; need for a large number of measurement points; hypersensitive to boundary and environmental changes.
Electro-mechanical impedance-based	The composition of a system contributes a certain amount to its total electrical/mechanical impedance of the system, and presence of damage modifies the impedance in a high frequency range, normally higher than 30 kHz.	Low cost and simple for implementation; particularly effective for detecting defects in planar structures.	Unable to detect damage distant from sensors; not highly accurate; accurate for large damage only.
Static-parameter-based (displacement, strain, etc.)	Presence of damage causes changes in displacement and strain distribution in comparison with benchmark.	Locally sensitive to defects; simple and cost-effective.	Relatively insensitive to undersized damage or the evolution of deterioration.
Acoustic emission	Rapid release of strain energy generates transient waves, whereby presence or growth of damage can be evaluated by capturing damage-emitted acoustic waves.	Able to triangulate damage in different modalities including matrix crack, fibre fracture, delamination, microscopic deformation, welding flaw and corrosion; able to predict damage growth; surface mountable and good coverage.	Prone to contamination by environmental noise; complex signal; for locating damage only; passive method; high damping ratio of the wave, and therefore suitable for small structures only.
Elastic-wave-based (Lamb wave tomography, etc.)	Structural damage causes unique wave scattering phenomena and mode conversion, whereby quantitative evaluation of damage can be achieved by scrutinising the wave signals scattered by damage.	Cost-effective, fast and repeatable; able to inspect a large structure in a short time; sensitive to small damage; no need for motion of transducers; low energy consumption; able to detect both surface and internal damage.	Need for sophisticated signal processing due to complex appearance of wave signals, multiple wave modes available simultaneously; difficult to simulate wave propagation in complex structures; strong dependence on prior models or benchmark signals.

Chapter 2

Background on Ultrasonic Wave Propagation in Thin-walled Structures

The commonly-used methods for analysis and simulation of wave propagation in thin-walled structures applied to structural health monitoring (SHM) are reviewed in this chapter. Analysis and simulation are clearly distinguished in this dissertation as the former, by convention in wave propagation, refers to the extraction of the characteristics of waves in a waveguide, whereas the latter deals with simulation of wave motion in the time domain.

As mentioned in Chapter 1, ultrasonic wave propagation-based methods form an important class of damage detection and identification schemes in the engineering fields. The minimum detectable size of a defect has an inverse relation with the frequency of the diagnostic waves[1]. Up to few hundreds of kilohertz are often required for diagnostic waves in SHM of thin-walled structures[2]. In such frequency ranges, multiple modes of waves propagate in a structure. These wave modes can be associated with a motion which is symmetric or anti-symmetric with respect to the mid-plane of the thin-walled structure, respectively known as *symmetric waves* and *anti-symmetric waves* [Viktorov, 1967]. The higher the excitation frequency, the more non-uniform the distribution of the displacements becomes through the thickness of a thin-walled structure. When there are multiple modes of low and high order, a different behavior than that which is captured by elementary plate and shell theories in conventional structural analysis is often observed. The difference is predominantly due to the poor quality of the approximation of the assumed displacement fields used

[1] In a non-dispersive waveguide, the wavelength of the diagnostic waves is inversely proportional to the excitation frequency. The minimum detectable damage size is often considered to be half of the wavelength [Boller et al., 2009].

[2] Detecting a crack of 10mm in a steel plate of 1mm thick requires the excitation frequency to be at least 250kHz, roughly speaking.

in these theories [Wang and Yua, 2007], as a result of which the assumed displacements in the thickness-wise direction are not able to capture the material motion required to convey the waves. For example, neglecting the thickness contraction mode in the displacement field of a plate structure modeled in 2D, will result in a constant speed for the fundamental, i.e. the lowest mode, symmetric waves, irrespective of the frequency of the excited waves [Doyle, 1989]. As another example, the propagation speed of the fundamental antisymmetric waves may be miscomputed to be significantly larger than the actual speed of that particular mode in the absence of the shear deformation and rotary inertia [Gopalakrishnan et al., 2008]. In non-destructive testing (NDT) and SHM, it is therefore essential to identify the validity range of the model used to avoid inaccurate interpretation of the diagnostic waves in the integrity monitoring system.

In wave propagation analysis, by assuming a harmonic motion and iterating the solution procedure for a set of discrete frequencies, the behavior of the propagating and non-propagating waves can be described. This description is mostly provided in form of spectrum relations and dispersion relations, which are briefly discussed later in this chapter. Using these relations, the speed of the present wave modes and their wavelengths at different frequencies can be determined. This information may be significant in some wave propagation-based SHM approaches, since the arrival time of a wave packet along with its corresponding propagation speed can be used to specify the distance from a disturbance source. In this chapter, after presenting the general theory of wave propagation in anisotropic media and introducing the basic definitions, an insightful case study of wave propagation in a curved composite waveguide is provided. This example highlights some important aspects of elastic wave propagation in composite structures which are discussed throughout this dissertation. Some key considerations in using ultrasonic waves in SHM systems are subsequently reviewed.

Simulation methods can alternatively be used to provide the time domain solution of wave equations. This can be a challenging problem for SHM applications due to the high driving frequencies. A robust, accurate, flexible, and computationally-efficient procedure is required to handle the physical and mathematical complexities of ultrasonic wave motion in a reasonable amount of time. The most commonly-used methods are transformed domain methods and the time domain methods, discussed in this chapter.

2.1 Guided Ultrasonic Waves in Thin-walled Structures

Depending on the boundary conditions, geometry, and material properties, various types of waves may propagate through a solid body [Viktorov, 1967, Staszewski et al., 2004]. Bulk waves, for example, travel within the interior of a material and exhibit a finite number of wave modes. Waves propagating

in thin-walled structures at ultrasonic frequency regimes are known as guided ultrasonic waves (GUWs). Guided ultrasonic waves remain guided between two free surfaces of a thin-walled structure viewed as a waveguide. Since GUWs are confined inside the outer walls of a thin-walled structure, in both flat plate and curved shells, they can travel over large distances. This feature makes GUWs well-suited for the ultrasonic inspection of engineering structures such as aircraft parts [Dalton et al., 2001, Gao and Rose, 2009, Rose and Soley, 2000, Salamone et al., 2009, Puthillath and Rose, 2010], pressure vessels and oil tanks [Jiangong et al., 2007, Rose et al., 1994, Feng et al., 2010], pipelines [Cawley et al., 2003, Demma et al., 2004, Na and Kundu, 2002, Siqueira et al., 2004, Volker and Bloom, 2011, Bloom et al., 2008, Breon et al., 2007, Ledesma et al., 2009, Pan et al., 1999], and railways [di Scalea and McNamara, 2003, di Scalea et al., 2005, McNamara and Lanza di Scalea, 2002, Rose et al., 2002, Wilcox et al., 2003]. Guided ultrasonic waves obey the wave equations derived from continuum mechanics laws, with appropriate stress boundary conditions at the two surfaces of a thin-walled structure [Achenbach, 1993].

Damage, as a local discontinuity, can be identified in GUW-based SHM, by studying the waves scattered by the discontinuity. Once a GUW packet propagating at a certain speed encounters a damaged area, depending on the damage type and configuration, a part of the wave packet may travel through this zone and get refracted, and a part of it can get reflected by the damage. In GUW-based SHM, in general, the information from the reflected and refracted wave packets is used to investigate the integrity of the structure under interrogation. As discussed in Chapter 1, the exciting and measuring of GUWs is usually a reasonably cost-effective, fast and repeatable processes [Giurgiutiu, 2008].

In plates-like structures, GUWs travel as Lamb waves, i.e. a combination of the pressure (P) waves and shear-vertical (SV) waves, and shear horizontal (SH) waves [Viktorov, 1967][3]. The SV waves are vertically polarized, thus dominated by out-of-plane motion, while SH waves are horizontally polarized, thus dominated by in-plane motion. Both Lamb waves and SH waves can be symmetric or antisymmetric with respect to the plate mid-plane. The modes of Lamb waves are conventionally called A0, S0, A1, S1, A2, S2, etc., where A(n) and S(n), for $n \in \{0, 1, 2, \cdots\}$, respectively denote the anti-symmetric and symmetric modes. Higher values of n indicate higher-order modes. Shear-horizontal waves are called similarly, e.g. SH0, SH1, SH2, however, the even and odd values of n in SH(n), denote the symmetric and anti-symmetric SH waves, respectively. Note again that the governing equations of GUWs are generally derived from traction-free boundary conditions on both surfaces of the thin-walled structure. The propagation speed of these waves depends on the product of excitation frequency and plate thickness [Achenbach, 1993].

The dependence of the propagation speed of waves on the frequency may make the waveguide dispersive. In a dispersive waveguide, a disturbance with a certain frequency bandwidth does not retain its shape throughout the propa-

[3]The term *Lamb waves* is commonly used when the structure is flat. Following the convention, in this dissertation, the generic term GUW is used when the structure is curved, or when both Lamb waves and SH waves are meant.

gation, as waves at each frequency travel at different speeds. These issues will be explained concisely in the next sections.

2.2 Spectral Analysis and Basic Definitions

An alternative approach to the analysis of mathematical functions or signals in time is to use a transformed domain and, in particular, the frequency domain. A frequency domain analysis, which is also known as a *spectral analysis*, decomposes a time series into a spectrum of cycles of different lengths [Doyle, 1989]. In wave propagation, spectral analysis is utilized to understand the wave mechanics in a waveguide by extracting the interrelations of wave properties, e.g. frequency, wavenumber, wave velocities, [Su and Ye, 2009, Giurgiutiu, 2008, Balageas et al., 2006, Boller et al., 2009, Kundu, 2004], and will be briefly discussed in this section.

2.2.1 Wave Equations in the Frequency Domain

The linear partial differential equations (PDE)s describing the wave motion in a heterogeneous anisotropic elastic medium can be stated as [Achenbach, 1993]:

$$\mathfrak{L}\mathbf{u} + \mathbf{f} = \mathcal{J}\ddot{\mathbf{u}}, \text{ in } \Omega, \tag{2.1}$$

accompanied by some prescribed boundary conditions. In Equation (2.1), $\mathfrak{L}$ is a continuous differential operator, $\mathcal{J}$ is a matrix containing inertial properties of the medium, $\mathbf{u} = (u^1, u^2, \cdots, u^m)^T$ is the vector of m dependent variables, Ω denotes the material body, and the over-dots show differentiation with respect to time. If a classical continuum mechanics model is considered, the dependent variables will be translational degrees of freedom (DOFs). Rotational degrees of freedom however, will be added to the translational DOFs, if the waveguide is a Cosserat continuum[4] [Suiker et al., 2001]. The vector $\mathbf{f} = (f^1, f^2, \cdots, f^m)^T$ specifies the given external excitation. The transformed form of the above equation in the frequency domain can be sampled at L points in time, and subsequently approximated using the discrete Fourier transform (DFT), or its more computationally-efficient version known as *fast Fourier transform* (FFT), see Appendix 1. Therefore,

$$\sum_{n=0}^{L-1} \left(\mathfrak{L}\hat{\mathbf{u}}_n + \hat{\mathbf{f}}_n \right) e^{i\omega_n t} = \sum_{n=0}^{L-1} -\omega_n^2 \mathcal{J}\hat{\mathbf{u}}_n e^{i\omega_n t}, \tag{2.2}$$

where the $\hat{(\cdot)}_n$ shows the FFT coefficients corresponding to the nth discrete frequency ω_n. Since each $e^{i\omega_n t}$ is independent, Equation (2.2) must be satisfied for each n. To determine the characteristics of the medium as a waveguide, the

[4]The Cosserat theory of elasticity, also known as micropolar elasticity, incorporates a local rotation of points as well as the translation assumed in classical elasticity, and a moment stress as well as the force stress.

homogenous form of Equation (2.2), i.e. $\hat{\mathbf{f}}_n = 0$, is considered for each n. In the Cartesian coordinate system for example, the solution to this equation is of the type:

$$\hat{\mathbf{u}}_n = \hat{\mathbf{U}}_n \exp\left(i\left[\omega t - (k_x^n x + k_y^n y + k_z^n z)\right]\right), \tag{2.3}$$

where the vector $\hat{\mathbf{U}}_n$ contains unknown constants, which have to be determined in accordance with the boundary conditions, and k_x^n, k_y^n, and k_z^n denote the wavenumbers in x-, y-, and z- directions, respectively, corresponding to the nth discrete frequency ω_n. The wave vector defined by:

$$\mathbf{k}_n = \left[k_x^n,\, k_y^n,\, k_z^n\right]^T, \tag{2.4}$$

points to the direction of the wave propagation [Wang and Yua, 2007].

2.2.2 Spectrum and Dispersion Relations

The *characteristic equation* of the waveguide can be obtained by substituting Equation (2.3) in the governing equations (2.1). The characteristic equation can be symbolically represented by an implicit functional form:

$$\mathscr{G}(\omega_n, \mathbf{k}_n) = 0, \tag{2.5}$$

or by an explicit form, i.e. *dispersion relation*:

$$\omega_n = \mathscr{W}(\mathbf{k}_n). \tag{2.6}$$

The exact solution of the dispersion relation for a continuum often requires solving transcendental equations [Wang and Yua, 2007]. When using reduced models however, e.g. plate theories, the dispersion relation will appear as a polynomial eigenvalue problem (PEP), which can be solved straight-forwardly using standard techniques [Gopalakrishnan et al., 2008].

In the presence of dispersion, which can be regarded as frequency-dependent effects in wave propagation, wave velocity is no longer uniquely defined, giving rise to the distinction of phase velocity, i.e. velocity at which individual harmonics move, and group velocity, i.e. velocity at which a wave packet or envelope, being localized in both time and frequency, propagates through space. In the Cartesian coordinate system, the *group velocity* $\mathbf{c}_g^n$ corresponding to ω_n is defined by:

$$\mathbf{c}_g^n = \boldsymbol{\nabla}\mathscr{W} = \frac{\partial \mathscr{W}}{\partial \mathbf{k}_n}, \tag{2.7}$$

where $\boldsymbol{\nabla}$ denotes the gradient operator, and the *phase velocity* $\mathbf{c}_p^n$ by:

$$\mathbf{c}_p^n = \frac{\mathscr{W}}{k_n}\frac{\mathbf{k}_n}{|\mathbf{k}_n|} \tag{2.8}$$

with k_n denoting the magnitude of the wave vector $\mathbf{k}_n$. It can be realized from the two equations above that, if the relation between the frequency and the wavenumbers is linear, the group and phase velocities will be equal.

2.2.3 Case Study: A Higher-order Model for GUWs in Composite Cylindrical Shells

The generic forms and solutions presented so far in this section are employed for analysis of wave propagation in composite curved panels. The main reason for presenting this section here is not to study the waveguide behavior of particular specimens, but to clarify the definitions and explanations of the wave mechanics provided in previous and those that will be made in future sections. Besides the insightful role of this example in extracting the waveguide characteristics of an anisotropic medium, the formulation may also be useful in the design of GUWs-based SHM systems.

Various methods such as analytical solutions [Nayfeh and Chimenti, 1989, Nayfeh, 1991, Wang and Yuan, 2007, Yuan and Hsieh, 1998], higher-order plate theories [Chitnis et al., 2001, Wang and Yua, 2007, Whitney and Sun, 1973, Pahlavan, 2011], and semi-analytical finite element method (SAFEM) [Bartoli et al., 2006, Dong and Nelson, 1972, Marzani et al., 2008, Nelson et al., 1971, Rattanawangcharoen et al., 1992], have been developed by researchers to extract the spectrum and dispersion relations for metallic and composite structures from the generic form of the wave equation. Although analytical solutions can be found in some cases, they require highly intensive computations, since the exact solutions often involve solving transcendental equations [Wang and Yua, 2007, Giurgiutiu, 2008]. A higher-order theory for multi-layered composite cylindrical shells is formulated in this section, from which analysis of guided waves in flat composite panels and flat and curved isotropic panels can also be extracted. This work extends the model proposed by Wang and Yua [2007] for composite flat plates, to cylindrical shells. In this model, antisymmetric and symmetric waves are captured using third- and second-order expansion of the displacement field, respectively. This model can also be regarded as an extension of the Mindlin plate theory, which is a first-order plate theory and only captures the lowest anti-symmetric wave mode [Whitney and Sun, 1973], to a third-order plate theory.

The following displacement field was considered to implement the model:

$$\begin{pmatrix} u_r \\ u_\theta \\ u_z \end{pmatrix} = \begin{pmatrix} u_r^0 + (r-R)\,\chi_1 + (r-R)^2\,\chi_2 \\ u_\theta^0 + (r-R)\,\varrho_1 + (r-R)^2\,\varrho_2 + (r-R)^3\,\varrho_3 \\ u_z^0 + (r-R)\,\phi_1 + (r-R)^2\,\phi_2 + (r-R)^3\,\phi_3 \end{pmatrix} \tag{2.9}$$

in the cylindrical coordinate system (r, θ, z). The radius of the cylinder is denoted by R, and u_r^0, u_θ^0, and u_z^0 are the displacements of the mid-plane of the shell in r-, θ-, and z- directions, respectively. Also χ_i, ϱ_i, and ϕ_i, $i \in \{1, 2, 3\}$, are the associate higher-order degrees of freedom. The odd-order terms with respect to r in u_θ and u_z together with even-order terms in u_r describe anti-symmetric wave modes; the other terms capture symmetric wave modes. The vector of the dependent variables is defined by:

$$\mathbf{u} = \begin{pmatrix} u_r^0, & \chi_1, & \chi_2, & u_\theta^0, & \varrho_1, & \varrho_2, & \varrho_3, & u_z^0, & \phi_1, & \phi_2, & \phi_3 \end{pmatrix}^T. \tag{2.10}$$

The assumed through-the-thickness distribution of the displacement field in Equation (2.9) is accompanied by a 2D wave propagation pattern that only takes place in the $\theta - z$ plane. To determine the wave propagation characteristics, a harmonic motion was considered as:

$$\mathbf{u} = \hat{\mathbf{U}} \exp\left(i\left[\omega t - (k_\theta r\theta + k_z z)\right]\right) \tag{2.11}$$

where k_θ and k_z are the wavenumbers in the circumferential and longitudinal directions, ω denotes the angular frequency, and $\mathbf{u}$ is the vector of dependent variables the amplitude of which is shown by $\hat{\mathbf{U}}$. For a prescribed propagation direction γ,

$$k_\theta = k\sin\gamma \quad , \quad k_z = k\cos\gamma. \tag{2.12}$$

To derive the equations of motion, the strain-displacement and stress-strain relations of the medium are required . The stress-strain relations for each layer of the composite laminate follow the Hooke's law for linear elastic materials [Reddy, 1997]. The strain-displacement in the cylindrical coordinate system [Yuan and Hsieh, 1998], when the radius R is reasonably larger than the thickness of the laminate, can be expressed by:

$$\boldsymbol{\epsilon} = \begin{pmatrix} \frac{\partial}{\partial r} & \frac{1}{r} & 0 & 0 & \frac{\partial}{\partial z} & \frac{1}{r}\frac{\partial}{\partial \theta} \\ 0 & \frac{1}{r}\frac{\partial}{\partial \theta} & 0 & \frac{\partial}{\partial z} & 0 & \frac{\partial}{\partial r} - \frac{1}{R} \\ 0 & 0 & \frac{\partial}{\partial z} & \frac{1}{r}\frac{\partial}{\partial \theta} & \frac{\partial}{\partial r} & 0 \end{pmatrix}^T \begin{pmatrix} u_r \\ u_\theta \\ u_z \end{pmatrix}, \tag{2.13}$$

where $\boldsymbol{\epsilon}$ denotes the strain field in the reduced Voigt notation. Given the stress-strain and strain-displacement relations, the equations of motion, i.e. Equation (2.1), can be obtained using the Hamilton's principle or balance of linear and angular momentum [Reddy, 1997]. For the sake of brevity, the expanded form of these equations is not shown here. Substituting the harmonic response in the equations of motion, the problem was formulated as a polynomial eigenvalue problem (PEP), the procedure for which is as outlined in Wang and Yua [2007]. It should be noted that contrary to flat plates with balanced layups, the symmetric and anti-symmetric wave modes are coupled in a cylindrical composite shell.

The presented model was validated numerically, not shown here, and the results exactly match those of Wang and Yua [2007] when $R \to \infty$. Next, wave modes in a flat Graphite-Epoxy panel with stacking sequence $[0, 90, 0, 90]_s$ were studied at 50kHz. The material properties of each layer of the laminate are: $E_1 = 118$GPa, $E_2 = 9.0$GPa, $E_3 = 9.0$GPa, $\nu_{12} = .029$, $\nu_{13} = .02$, $\nu_{23} = .049$, $G_{12} = 5.97$GPa, $G_{13} = 5.97$GPa, $G_{23} = 3.75$GPa, $\rho = 1570\text{kg/m}^3$, where for $i, j \in 1, 2, 3$, E_i denotes the Young's modulus in i-direction, G_{ij} denotes the shear modulus in the ij-plane, and ν_{ij} and ρ respectively denote the Poisson's ratio and the density. In this notation, the lamina is considered in the 1-2-plane, where fibers are along the 1-axis.

The group speed *wave curves* demonstrating good agreement between theory and experiments conducted by Melo Mota [2011], are shown in Figure 2.1. The difference between theory and experiment does not exceed 5%, and is attributed

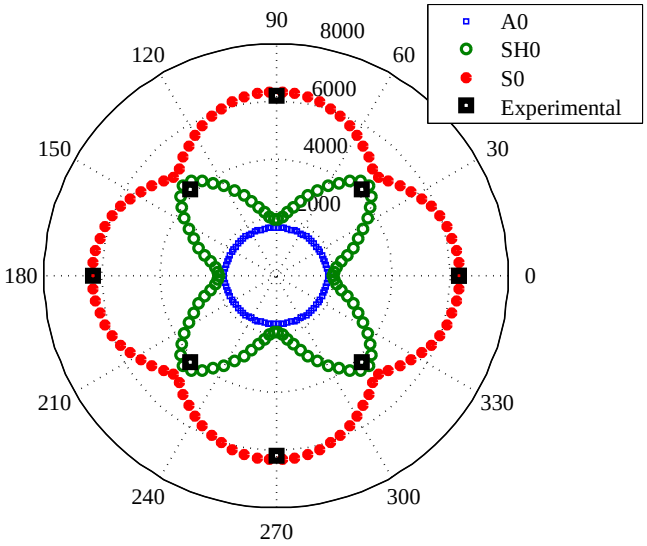

Figure 2.1: The group speed wave curves, $R \to \infty$.

to the uncertainties in the material properties and the test apparatus. The wave curves illuminate the frontier of waves of different modes, i.e. fundamental antisymmetric A0, fundamental symmetric S0, and fundamental shear-horizontal SH0, at 50kHz. As mentioned earlier, the wave front in anisotropic waveguides is not circular. At this frequency, S0 waves are the fastest waves in all directions, with the maximum speed along the direction(s) of the fibers. The A0 mode, which propagates uniformly in all directions, is the slowest mode, hence, it has the smallest wavelength and may be more sensitive to small-sized damage. The reason for the direction-independent speed of A0 is that the fundamental anti-symmetric mode is highly dominated by the bending stiffness of a panel, which is almost equal in all directions.

The phase speed dispersion curves for a cylindrical shell made of the same material and stacking sequence with $R = 500$mm are shown in Figure 2.2, where the multi-mode nature of the guided waves can be clearly observed. The presented model was compared to a lower order theory, in which only the first order terms in Equation (2.9) were considered. It should be noted that this model is different from that used in classical plate theories, as it still captures a first-order deformation through the thickness of the laminate, i.e. *thickness contraction*. The frequency varies between 0 and 2000kHz and different symmetric and anti-symmetric waves propagate in this frequency regime. Following the convention, symmetric, anti-symmetric, and shear-horizontal waves are respectively denoted by S, A, and SH, with a subscript showing the mode number. The cut-off frequency of various wave modes can be observed in the figure. The term *cut-off frequency* refers to the frequency at which a certain wave mode starts to propagate. For example, the cut-off frequency of the second anti-symmetric waves A1

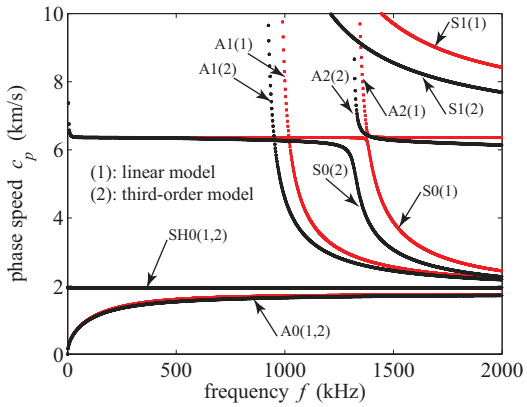

Figure 2.2: The phase dispersion curves for the composite cylindrical shell, $R = 500$mm.

is about 1000kHz. Without further adjustments and corrections, the presented third-order model provides accurate results up to the cut-off frequency of the A2 mode [Wang and Yua, 2007].

The presented formulation provides a fast and computationally-efficient analysis tool for understanding the physics of guided waves in thin-walled structures. This third-order model model presents accurate results if at the effective frequency range of the excitation, the displacement distribution can be captured with a third-order polynomial expansion. For alternative approaches and elaborate discussions on the analysis of wave propagation in composite structures, the reader is referred to [Su and Ye, 2009, Giurgiutiu, 2008, Wang and Yua, 2007, Yuan and Hsieh, 1998].

2.3 Some Considerations in Using Guided Ultrasonic Waves

In order to minimize the issues arising from the multi-mode nature and the dispersion of the GUWs in SHM systems, certain techniques such as modulation of the excitation pulse and tuning of GUWs may be employed.

2.3.1 Wide-bandwidth Excitation versus Narrow-bandwidth Excitation

In SHM, it is often desired that a diagnostic wave packet is a short-duration pulse, such that its reflections from the structural discontinuities and edges do not overlap, and hence, can be distinguished. If the diagnostic wave packet and its reflections are separate envelopes, travel times can be computed in a

straight-forward manner thereby facilitating the damage identification procedure. Making a signal narrow in time however, generally, makes it wide in the frequency domain, i.e. *wide-banded signal*. When a wide-banded signal with a large frequency range is used in a dispersive medium, since waves at different frequencies propagate at differing phase velocities, the observed pulse will change shape while traveling. As a result, the experimentally-measured signals from such waveguides become fuzzy and difficult to interpret. To cope with this issue, the signals in the frequency domain can also be narrowed [Gopalakrishnan et al., 2008]. Making the signals narrow in the frequency domain implies that different frequencies in the signal, which lie within a narrow range and thus, very close to each other, propagate at nearly equal phase speeds. In other words, in a short frequency interval, the group speed, which is generally a nonlinear function of frequency, varies almost linearly with respect to frequency. Minimizing the dispersion of the signals in general, can improve the robustness and accuracy of the signal processing for the arrival time picking of the diagnostic waves.

Modulation is a standard technique for making narrow-banded pulses [Giurgiutiu, 2008]. A monochromatic signal with the carrier frequency of ω_c is multiplied by a Hanning window[5] banded in both time and frequency. This multiplication keeps the central frequency of the pulse unchanged. The frequency band of the signal however, depends on the temporal localization of the Hanning window. The resulting signal, referred to as a *narrow-banded pulse*, is extensively used in NDT and SHM. Different wide- and narrow-banded signals will be used in chapters 4, 5, 6, and 7 of this dissertation.

2.3.2 Tuning of Guided Waves

The multimode nature of GUW can make their application for SHM very complicated since at least two modes, with generally different dispersion characteristics, can exist and propagate simultaneously. Each propagating mode may interact with the structural discontinuities, e.g. damage and the boundaries, and also with the other propagating mode(s), as a result of which interpretation of the wavefield becomes difficult to impossible. Although subtraction of the response of the intact structure, i.e. *baseline response*, may alleviate the complexity of the data interpretation, it introduces a more drastic issue for SHM systems: the need to obtain an accurate baseline signal, which is a function of environmental and operational conditions also [Xu and Giurgiutiu, 2007]. Some of the challenges regarding the baseline response will be addressed in chapter 7 of this dissertation.

Tuning of GUW is one of the well-established solutions to the problem of the multimode appearance of GUW [Giurgiutiu, 2008, Xu and Giurgiutiu, 2007].

[5]The Hanning function, also called the Hann function, is frequently used to window signals, and also to reduce aliasing in Fourier transforms. The Hanning function is given by:

$$H(t) = \begin{cases} \cos^2\left(\frac{\pi t}{2a}\right) & ; -a < t < a \\ 0 & ; \text{elsewhere.} \end{cases}$$

Based on the physical characteristics of the actuator(s), the coupling of the actuator(s) to the structure surface, excitation of the actuator(s), and the mechanical properties of the structure to be interrogated, one of the fundamental wave modes may be deactivated at a specific driving frequency. This mode deactivation process, which is known as tuning of GUW, is often an essential task in the design and optimization of real SHM systems. By tuning the GUW, the group speed of the activated mode will be, before interaction with structural discontinuities, the only speed at which the energy and information is transferred. Since this dissertation does not deal with modeling of sensors and actuators, i.e. the input signals on, and the output signals from the structure are respectively forces and displacements, GUW tuning is not dealt with explicitly. The interested reader is referred to [Giurgiutiu, 2008] for detailed information on this subject.

2.4 Simulation Methods for Propagation of Guided Ultrasonic Waves

Simulation methods for propagation of GUWs can be categorized into time domain methods, and transformed domain methods [Gopalakrishnan et al., 2008]. The transformed domain methods, also known as *spectral methods*, predominantly use global orthogonal bases in a weighted residual scheme, to reduce a system of multi-dimensional partial differential equations (PDEs) to a set of ordinary differential equations (ODEs). This is carried out by successively transforming the temporal and spatial domains to the frequency and the wavenumber domains, respectively [Doyle, 1989, Gopalakrishnan et al., 2008]. The basis functions in spectral methods are often infinitely differentiable, and used in a Galerkin weighted residual scheme to solve the governing equations of a waveguide. A classical example of such methods, which will be further discussed in this section, is the Fourier spectral method.

Time domain methods for simulation of GUWs are, on the other hand, mostly based on a weighted residual scheme for discretization of the physical spatial domain, and finite difference formulas for numerical time integration. A number of time domain approaches have been applied for simulation of GUWs, e.g. the finite element method (FEM), [Koshiba et al., 1984, Belytschko and Hughes, 1983, Oden and Reddy, 1976, Zienkiewicz and Cheung, 1967, Hughes, 1987] the boundary element method (BEM) [Cho and Rose, 1996, Wang and Achenbach, 1994, Gaul et al., 2003], the finite difference method (FDM) [Virieux, 1986, Gsell et al., 2004], the finite strip element method [Bergamini and Biondini, 2004, Dawe, 2002], and the local interaction simulation approach (LISA) [Delsanto et al., 1992, Lee and Staszewski, 2007, Nadella and Cesnik, 2011]. Among all these methods, FEM seems to be, by far, the most extensively-used approach, since it effectively deals with geometrically complex, inhomogeneous, and anisotropic structures. In FEM, a waveguide domain is subdivided into elements, and basis functions, which are local in character, i.e. confined

to an element, are used in a Galerkin approximation of the dependent variables of the governing equations of the waveguide. Time integration in FEM is predominantly performed through an implicit or an explicit Newmark integration method [Hughes, 1987]. For details of FEM, the reader is referred to Belytschko and Hughes [1983], Oden and Reddy [1976], Zienkiewicz and Cheung [1967], Hughes [1987]. A specific version of FEM known as the *(pseudo)spectral finite element method*[6] employs higher-order basis functions and is equipped with an explicit time integration scheme. This approach, which alleviated a number of shortcomings in the conventional FEM and offered an improved convergence rate and accuracy [Komatitsch et al., 2000, Peng et al., 2009, Ha et al., 2010, Kim and Chang, 2005], is outlined later in this section.

2.4.1 Fourier-based Spectral Finite Element Method

The fast Fourier transform (FFT)-based spectral method is the most well-established transformed domain method, and was mainly introduced by Doyle [1989]. In this approach, as discussed earlier, successive Fourier transforms are employed for transformation of the governing equation from the physical temporal and spatial domains to the frequency and the wavenumber domains, respectively [Doyle, 1989, Gopalakrishnan et al., 2008]. As a result of using the Fourier transforms, the temporal and spatial variables in the governing equation are replaced with the transformation parameters, i.e. frequencies and wavenumbers. In the Fourier-based spectral finite element method (FSFEM), the successive transformations stop once the governing equations are expressed in terms of a single spatial coordinate, usually selected based on the geometry, loading and the boundary conditions. The remaining equations then, which can often be solved exactly, are expressed in terms of nodal coordinates as a result of which, the problem is formulated as a set of 1D finite element systems [Gopalakrishnan et al., 2008]. Various applications of the FSFEM in simulation of wave propagation can be found in the literature, see for example Farris and Doyle [1989], Chakraborty and Gopalakrishnan [2004, 2006], Gopalakrishnan et al. [1992], Krawczuk et al. [2003], Krawczuk [2002], Mahapatra and Gopalakrishnan [2003, 2004], Mahapatra et al. [2000, 2006], Ostachowicz [2008], Palacz and Krawczuk [2002], Palacz et al. [2005a], Rizzi and Doyle [1992].

The FFT-based spectral methods offer the possibility of parallel computation of the system response to a set of monochromatic inputs with different frequencies. Compared to polynomial approximation bases, Fourier bases provide a more accurate expression of the dependent variable and their derivatives due to their spectral nature [Gopalakrishnan et al., 2008]. Two major issues however, limited the growth of the applications of Fourier-based spectral methods; (i) the periodicity assumption in the discrete Fourier transform and the subsequent drawback being the need to introduce artificial damping at the boundaries of the domain [Doyle, 1989, Gopalakrishnan et al., 2008], (ii) the global basis

[6]It is emphasized that the (pseudo)spectral finite element method and spectral methods are completely different in nature, and should not be mistaken.

of the Fourier space making the method inefficient in dealing with complex geometries. Later, Mitra and Gopalakrishnan [2005] suggested using the discrete wavelet transform (DWT) [Daubechies, 1992] to be applied in a Galerkin sense, as an alternative to FFT to alleviate some of these issues.

2.4.2 Wavelet-based Spectral Finite Element Method

Daubechies compactly-supported wavelets [Daubechies, 1992], which will be discussed in detail in Chapter 3 of this dissertation, are powerful tools for solving partial differential equations (PDEs) on bounded regions with strong gradients. This characteristic of Daubechies wavelets comes from the fact that they possess several appealing properties such as orthogonality, compact support, exact representation of polynomials up to a certain degree, and an ability to represent functions at different resolutions [Amaratunga and Williams, 1997, Amaratunga et al., 1994, Beylkin, 1992, Chen and Hwang, 1996, Chen et al., 1996, Han et al., 2006, Ko et al., 1995, Ma et al., 2003, Patton and Marks, 1996, Qian and Weiss, 1993]. The idea of using Daubechies compactly-supported wavelets [Daubechies, 1992] for spectral analysis of wave propagation in 1D and 2D waveguides has mainly been pursued by Mitra and Gopalakrishnan [Mitra and Gopalakrishnan, 2006d, 2007, 2005, 2006a,b]. They have shown computational improvements with DWT in comparison to the Fourier-based analysis by taking advantage of the removed periodicity assumption and the compact support of Daubechies wavelets [Mitra and Gopalakrishnan, 2005]. Formulation of the wavelet-based spectral finite element method (WSFEM) by Mitra and Gopalakrishnan, which is referred to as the *conventional* WSFEM in this dissertation, is analogous to the FSFEM, i.e. the FFT in the formulation is replaced with the wavelet-Galerkin approximation. This topic is discussed in a more elaborate fashion in chapters 3 and 5.

Despite the significant progress achieved by Mitra and Gopalakrishnan, there are still difficulties in dealing with 2D and 3D problems that have geometrical complexity and arbitrary boundary conditions, some solutions to these problems are given in this dissertation in chapters 3 to 6. Note that a different application of wavelets to solve wave equations based on representation on the spatial derivative operators has also been extensively reported in the literature, see for example [Faccioli et al., 1997, Hong and Kennett, 2002a,b, Amaratunga and Sudarshan, 2006, Sudarshan et al., 2006, Han et al., 2006, Qian and Weiss, 1993, Amaratunga et al., 1994, Ko et al., 1995, Patton and Marks, 1996, Ma et al., 2003], however, this is not aligned with the interest demonstrated in the present dissertation for spectral formulation of the elastic wave equation.

2.4.3 Spectral Element Method

The psudospectral element method, also known as the spectral element method (SEM), is a spectrally-convergent[7] higher-order finite element method for solv-

[7] Given p the order of a polynomial basis, a method is spectrally-convergent if the numerical errors decay faster than any power of $1/p$ [Canuto, 2007].

ing partial differential equations. The SEM was developed by Patera [1984] to solve fluid dynamics problems with slow convergence. Patera introduced SEM as a method which combines the generality of the finite element method with the accuracy of spectral techniques. Unlike the spectral methods however, which transform the governing equations from the physical space to the spectral space, orthogonal interpolating polynomials preserving partition of unity are employed in SEM, which keep the discretized governing equations in the physical space [Patera, 1984, Canuto, 2007]. In addition, in contrast to the spectral methods, the interpolating polynomials in SEM are applied at the element level, giving rise to the possibility of obtaining convergence by increasing the number of elements, i.e. h-refinement, or by increasing the degree of the polynomials, i.e. p-refinement. These polynomials can be either Chebyshev-Gauss-Lobatto-Lagrange or Legendre-Gauss-Lobatto-Lagrange polynomials. The latter however, lead to a diagonal mass matrix in the FEM formulation, and are preferable in most applications [Canuto, 2007]. The advantage of a diagonal mass matrix is that it makes the SEM very efficient for solving transient problems when combined with the explicit time integration, i.e. the Newmark-β, scheme [Komatitsch et al., 2000]. In this dissertation, the term SEM always refers to the spectral element method based on Legendre-Gauss-Lobatto-Lagrange polynomials.

Application of SEM in elastic wave propagation simulation seems to have been first introduced in Geophysics by Seriani [Seriani, 1998, Priolo et al., 1994, Seriani and Oliveira, 2008, Seriani and Priolo, 1994], and its use has been continued by several researchers, see for example [Komatitsch et al., 2000, Komatitsch and Tromp, 1999, 2002a,b, Komatitsch and Vilotte, 1998]. In simulation of GUWs for SHM applications, it took the scientific community a few years to import the SEM from Fluid Mechanics and Geophysics [Kim and Chang, 2005]. Various applications of SEM in modeling waveguides with and without damage, sensors, and actuators have been reported in the literature, see for example Kudela et al. [2007], Palacz and Krawczuk [2002], Peng et al. [2009], Ha et al. [2010], Kim and Chang [2005], Kim et al. [2008], Moll et al. [2010].

In SEM, numerical integration over the element domain is performed using a nodal quadrature, i.e. the integration points are the same as the element nodes. In one dimension, these nodes are located on the unequally-spaced Gauss-Lobatto-Legendre (GLL) points, as the $N+1$ roots of:

$$(1-\xi^2)P'_N(\xi) = 0\,,\ \xi \in [-1,1], \tag{2.14}$$

where $P'_N(\xi)$ is the first derivative of the Legendre polynomial of degree N. A 3D master SEM element with $N_\xi = 5$, $N_\eta = 5$, and $N_\gamma = 2$ is shown in Figure 2.3, where ξ, η, and γ denote the local coordinates.

Following the standard FEM [Hughes, 1987], the mass and the stiffness matrices can be constructed. The only difference in computation of these matrices will be that the GLL integration rule is used instead of the Gauss quadrature. Note that if $N = 1$ or $N = 2$, a standard Galerkin FEM is retrieved based on linear or quadratic elements, respectively. The reader is referred to [Canuto, 2007]

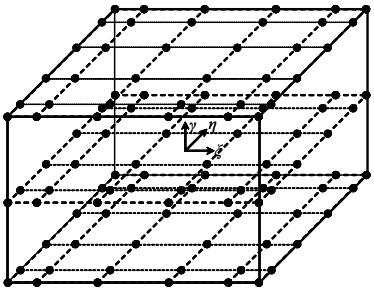

Figure 2.3: A 3D SEM element with $N_\xi = 5$, $N_\eta = 5$, and $N_\gamma = 2$.

for detailed information on numerical aspects of SEM, accuracy, and convergence. Note that accurately capturing the geometry through the isoparametric formulation is also possible using SEM due to the higher order basis functions in SEM [Komatitsch et al., 2000].

Having assembled the global mass and stiffness matrices, the explicit Newmark time integration scheme based on the central difference formulas can be adopted. Therefore:

$$\left(\frac{1}{\Delta t^2}\mathbf{M} + \frac{1}{2\Delta t}\mathbf{C}\right)\mathbf{q}_{t+\Delta t} = \mathbf{f}_t - \left(\mathbf{K} - \frac{2}{\Delta t^2}\mathbf{M}\right)\mathbf{q}_t - \left(\frac{1}{\Delta t^2}\mathbf{M} - \frac{1}{2\Delta t}\mathbf{C}\right)\mathbf{q}_{t-\Delta t} \tag{2.15}$$

where $\mathbf{K}$, $\mathbf{M}$, and $\mathbf{C}$ respectively denote the global stiffness, mass, and damping matrices, $\mathbf{q}$ is the global nodal displacement vector, and $\mathbf{f}$ is the vector of external point loads. The subscript shows the time step, and Δt denotes the time interval. It can be observed in the equation above that the solution at each time step depends only on the quantities at the previous time steps. Explicit methods are very efficient when the mass and the damping matrices have diagonal structures. The damping matrix hence, is often considered to be proportional to the mass matrix, to avoid inversion of a non-diagonal matrix [Komatitsch et al., 2000]. The disadvantage of explicit methods is the limitation of the time step size due to a stabilization criterion [Hughes, 1987]: there is a critical time step size Δt_{cr} above which the integration scheme becomes unstable. This critical time step size is determined by the stiffest element in the entire model.

2.5 Motivation of Using Wavelets for Spectral Finite Element Simulation of GUWs

The application of guided ultrasonic waves in SHM of thin-walled structures was briefly reviewed in this chapter. The basic concepts and terms required for GUWs-based SHM were defined, and some of the more-commonly used simulation methods for GUWs in anisotropic structures, i.e. FEM and SEM, Fourier-based spectral FEM, and wavelet-based spectral FEM, were also discussed. It

is believed that there are certain aspects of these methods, which can be improved, or constructively combined with other available approaches, to provide more computationally-efficient tools. Following this notion, the next four chapters of this dissertation are devoted to the development of spectral finite element schemes for simulation of GUWs. The key idea behind the proposed approaches to simulate GUWs in this dissertation is to take advantage of the complementary features of the wavelet-based spectral analysis with the Galerkin finite element discretization of the spatial domain. In the next chapter, i.e. Chapter 3, the mathematical foundation of the wavelet transform and the wavelet-Galerkin discretization will be considered. Construction of 1D, 2D and 3D WSFEM will be presented in chapters 4, 5, and 6, respectively. These models will be used in Chapter 7 to develop an SHM methodology for load and damage monitoring in composite structures.

Chapter 3

Wavelet Transform and Applications

A wavelet is a wave-like oscillation which has compact support[1]. Wavelet analysis allows a square-integrable function[2] over an interval to be expressed in terms of orthonormal compactly-supported function bases. Wavelets are designed to exhibit specific properties that make them ideal candidates for signal processing in the time-frequency domain, data compression, and solving partial differential equations (PDEs).

The first mention of the wavelet analysis appears to be in an appendix of the thesis of Alfred Haar [1910]. After Haar, separate studies, which did not appear to be parts of a coherent theory, were performed until Zweig's discovery of the continuous wavelet transform (CWT) [Zweig et al., 1976]. This was a notable contribution to wavelet theory [Meyer, 1993]. Wavelet analysis was developed further in the 1980's by Goupillaud et al. [1984] and their formulation of the CWT, Daubechies [1988] and her construction the orthogonal compactly-supported support wavelets, and Mallat's introduction of multiresolution framework for wavelets [Mallat, 1989].

Wavelets, as a mathematical concept, have extensive applications in various disciplines [Williams and Amaratunga, 1997]. They can be used to analyze nonstationary time series, whereas Fourier analysis generally can not be. In wavelet-based image processing for example, if one removes the highest frequencies of the transformed image, the reconstructed image still looks like a low resolution version of the full picture, while when Fourier analysis or other global functional

[1] The support of a function is the set of points where the function is not zero. A function has compact support if it is zero outside of a compact set.

[2] A square-integrable function, also called a quadratically integrable function, is a real- or complex-valued measurable function for which the integral of the square of the absolute value is finite, i.e.

$$\int_{-\infty}^{\infty} |f(t)|^2 dt < \infty \ , t \in \mathbb{C}$$

bases are used, the image may lose all resemblance to the original picture, after a few harmonics are removed [Williams and Amaratunga, 1997]. The FBI uses wavelets to compress and store fingerprints information [Bradley et al., 1993]. In structural health monitoring (SHM), wavelets multi-resolution analysis (MRA) is frequently used in damage detection algorithms [Giurgiutiu, 2008, Grabowska et al., 2008, Rizzo and di Scalea, 2006a,b, Staszewski et al., 2004]. Wavelets are also widely employed to improve the efficiency of solving partial differential equations (PDEs) [Amaratunga and Williams, 1997, Amaratunga et al., 1994, Beylkin, 1992, Chen and Hwang, 1996, Chen et al., 1996, Qian and Weiss, 1993]. They are for instance, applied to the analysis of propagation of waves in various disciplines, such as in fluid dynamics [Chen and Hwang, 1996, Qian and Weiss, 1993] and electromagnetics [Fujii and Hoefer, 2003, Karumpholz and Katehi, 1996].

Wavelets also appear in different contexts of structural dynamics. As one application, they are utilized to form the basis functions in finite element analysis (FEA) [Ko et al., 1995, Ma et al., 2003, Patton and Marks, 1996]. Alternatively, they are employed to block-diagonalize the finite element mass matrix, to improve the efficiency of the time integration scheme [Goswami et al., 1995]. The idea of using compactly-supported wavelets [Daubechies, 1992] for spectral analysis of wave propagation was suggested and has mainly been pursued by Mitra and Gopalakrishnan [2006d, 2007, 2005, 2006a,b]. They have shown how the wavelet-Galerkin approach can be used to improve the computation time and accuracy compared to Fourier-based analysis.

In this chapter, a concise review of the wavelet transform, and some improved aspects of the wavelet-Galerkin method suggested by the present work, are provided. The materials presented in this chapter are essential for the rest of this dissertation, from solving PDEs of wave motion, to denoising the signals gathered from real hardware. At the beginning, the CWT, the Daubechies compactly-supported wavelets, and the MRA are described. Further, the wavelet-Galerkin method (WGM) and the decoupled wavelet-Galerkin method (DWG) for solution of linear wave equations are presented in a general fashion. Subsequently, an improved approach for elimination of the so-called *edge effects* of the WGM as a well-known drawback of using Daubechies wavelets on bounded domains is presented. The chapter ends with some numerical examples to clarify the concept of the DWG, and illustrate the improvements brought in by the formulation presented here.

3.1 The Continuous Wavelet Transform

The continuous wavelet transform (CWT), also known as the integral wavelet transform, maps a one-dimensional signal to a time-frequency or time-scale joint representation. The CWT is, in general, defined in reference to a mother function $\psi \in \mathbb{L}^2(\mathbb{R})$, where $\mathbb{L}^2$ denotes the space of square-integrable functions. The term *mother* implies that the family of wavelets is derived from ψ, by translating

and scaling, i.e. dilation of, the function:

$$\psi_{a,b}(t) = \frac{1}{\sqrt{a}}\psi\left(\frac{t-b}{a}\right), a \in \mathbb{R}^+, b \in \mathbb{R} \tag{3.1}$$

where b is the translation parameter and a is the scaling parameter, which can be interpreted as the reciprocal of the frequency. Further, t can be considered as the time variable. The normalization is chosen such that $\|\psi_{a,b}\| = \|\psi\|$, which keeps the energy of the signal constant across the different scales. The continuous wavelet transform of the continuous square-integrable function $f : t \to \mathbb{R}$ with respect to this family is:

$$CWT_{a,b}(f) = \left\langle f, \psi^*_{a,b} \right\rangle = \int_{-\infty}^{+\infty} f(t)\,\psi^*_{a,b}(t)\,dt \tag{3.2}$$

where * denotes the complex conjugate. It is known that reconstruction of an $\mathbb{L}^2$ function requires satisfaction of the admissibility condition [Daubechies, 1992]:

$$\int_0^\infty \frac{1}{\omega}|\Psi|^2 d\omega < \infty \tag{3.3}$$

with $\Psi(\omega) = \int \psi(t)e^{i\omega t}dt$ being the Fourier transform of ψ, and ω denoting the angular frequency. The admissibility condition therefore implies

$$\Psi(0) = \int_{-\infty}^{\infty} \psi(t)dt = 0 \tag{3.4}$$

which is imposed by the requirement that the integral in Equation (3.3) should stay bounded when $\omega \to 0$. From $\Psi(0) = 0$, it can also be extracted that wavelets have a band-pass spectrum (it completely blocks the zero frequency), and thus can be used as band-pass filters. This important property will be used later in this chapter for describing the discrete wavelet transform and multi-resolution analysis.

The inverse CWT is given by [Daubechies, 1992]:

$$f(t) = \int_{-\infty}^{+\infty}\int_{0}^{+\infty} \mathrm{CWT}_{a,b}(f)\,\psi_{a,b}(t)\,da\,db. \tag{3.5}$$

For most practical applications where the functions are evaluated or measured at only a limited number of discrete points, there is no analytical solution for equations (3.2) and (3.5). Although numerical integration may, with loss of generality, partially alleviate this issue, the time-bandwidth product of the $\mathrm{CWT} : \mathbb{R} \to \mathbb{R}^2$ can be problematic, since its size is the square of that of the signal. The signal description should, ideally, have as few components as possible for the sake of computational efficiency.

3.2 The Discrete Wavelet Transform

The discrete wavelet transform (DWT) was developed to overcome the difficulties of the numerical implementation in using CWT for analytically-unknown functions. Discrete wavelets are not continuously scalable and translatable, and therefore can only be scaled and translated in discrete steps. Modification of equation (3.1) for the DWT reads:

$$\psi_{j,k}(t) = \frac{1}{\sqrt{a_0^j}}\psi\left(\frac{t - kb_0}{a_0^j}\right); \forall j, k \in \mathbb{Z}. \tag{3.6}$$

The scaling factor $a_0 > 1$ suggests a fixed dilation step. It also affects the overall translation of the mother wavelet function. With an appropriate mother wavelet function and the specific choice of $a_0 = 2$ and $b_0 = 1$ providing dyadic sampling of the time and the frequency axes, the orthonormal basis $\{\psi_{j,k} : j, k \in \mathbb{Z}\}$ can be generated such that

$$\langle \psi_{j,k}, \psi_{l,m} \rangle = \delta_{jl}\delta_{km} \tag{3.7}$$

in which δ_{ij} is the Kronecker delta and

$$\psi_{j,k}(t) = 2^{-j/2}\psi\left(2^{-j}t - k\right). \tag{3.8}$$

A function $f(t)$ can, hence, be expressed in terms of the wavelets basis as follows:

$$f(t) = \sum_{j,k=-\infty}^{\infty} f_{j,k}\psi_{j,k}(t) \tag{3.9}$$

where $f_{j,k}$ are the transformation coefficients. If the wavelet function has a compact support, the above series over the translation factor k can be computed readily. The series over the scale j however, is more challenging to deal with, since the wavelet functions do not cover the entire spectrum of f; each time the scale increases, the wavelet is stretched in the time domain with a factor of two and the bandwidth is halved. Each new scale therefore, covers half of the remaining spectrum. This means that an infinite number of wavelet functions are required for an accurate representation of f. To cope with this issue, the so-called *scaling function* was introduced by Mallat [1989], which is responsible for covering that region of the spectrum which is not spanned by the wavelet function at each scale. Equation (3.4) suggests that, since for $\omega = 0$, $\Psi(0) = 0$, the normalized scaling function φ should satisfy:

$$\Phi(0) = \int_{-\infty}^{\infty} \varphi(t)dt = 1 \tag{3.10}$$

where $\Phi(\omega) = \int \varphi(t)e^{i\omega t}dt$ is the Fourier transform of φ. From a signal representation point of view, if both the wavelet and the scaling functions are considered, no information is lost and the signal can be perfectly reconstructed.

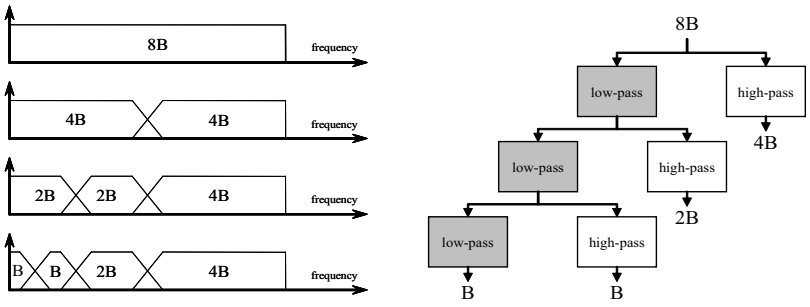

Figure 3.1: Iterated filter bank for multi-resolution analysis.

3.2.1 Multi-resolution Analysis

The idea of using the scaling function is essential in wavelets multi-resolution analysis (MRA). Based on the properties of the wavelet and the scaling functions, the DWT can be viewed as an iterated filter bank [Amaratunga and Williams, 1997]. The basic idea is to analyze a signal by passing it through a filter bank, which is a well-established procedure in sub-band coding[3] [Amaratunga and Williams, 1997]. The filter bank splits the signal spectrum into two parts; a low-pass part and a high-pass part. The high-pass part contains the smallest details of the signal, i.e. highest frequencies. The low pass part however, still contains some details which may be of interest. In this case, it can be split into low and high frequency spectra, and the procedure, as graphically illustrated in Figure 3.1, can be reiterated until the number of created bands is satisfactory.

The mathematical framework of the Daubechies compactly-supported wavelets is constructed in the context of the MRA. A multi-resolution analysis, in general, consists of a sequence of embedded subspaces

$$0 \subset \cdots \subset V_2 \subset V_1, \subset V_0, \subset V_{-1} \subset V_{-2} \subset \cdots \subset \mathbb{L}^2(\mathbb{R}) \tag{3.11}$$

with

$$\bigcap_{m \in \mathbb{Z}} V_m = 0. \tag{3.12}$$

If the orthogonal projection operator onto V_j is denoted by P_j, then $P_j f = f(t)$ for all $f(t) \in \mathbb{L}^2(\mathbb{R})$ if $j \to -\infty$.

The multi-resolution aspect is a consequence of an additional requirement known as *scale invariance*; all the spaces are scaled versions of the central space V_0. There is also a complementary requirement known as *shift invariance* stating that $f(t-k) \in V_j$ for all $k \in \mathbb{Z}$. These properties imply that, by scaling down, samples are considered at half the number of evaluation points. In the MRA

[3]Any form of transform coding that breaks a signal into a number of different frequency bands, and encodes each one independently, is called sub-band coding. Such a decomposition is mostly the first step in data compression for audio and video signals.

framework of interest, the problem to be solved is to find an orthonormal basis $\{\varphi_{0,k}; k \in \mathbb{Z}\}$ in V_0, from which the multi-resolution bases can be constructed with:

$$\varphi_{j,k}(t) = 2^{-j/2}\varphi\left(2^{-j}t - k\right); \forall j, k \in \mathbb{Z}. \tag{3.13}$$

The relationship between the two subspaces V_n and V_{n-1} onto which $f(t) \in \mathbb{L}^2(\mathbb{R})$ can be projected, is defined by the equation above. The difference between these two projections, as mentioned in Section 3.2, is presented with the orthogonal complement of V_j in V_{j-1}, denoted by W_j such that

$$V_{j-1} = V_j \oplus W_j \tag{3.14}$$

where $\oplus$ denotes the orthogonal, i.e. internal Hilbert, direct sum. The subspace W_n is spanned by the orthonormal basis $\{\psi_{j,k}; j, k \in \mathbb{Z}\}$ of $\mathbb{L}^2(\mathbb{R})$:

$$\psi_{j,k}(t) = 2^{-j/2}\psi\left(2^{-j}t - k\right); \forall j, k \in \mathbb{Z}. \tag{3.15}$$

The orthogonal projection operator onto W_j, denoted by Q_j, reads:

$$Q_j f = \sum_{k=-\infty}^{\infty} \langle f, \psi_{j,k} \rangle \psi_{j,k} = \sum_{k=-\infty}^{\infty} d_{j,k}\psi_{j,k} \tag{3.16}$$

where $d_{j,k}$ are known as the *detail coefficients*. Similarly, the orthogonal projection operator onto V_j can be expressed by

$$P_j f = \sum_{k=-\infty}^{\infty} \langle f, \varphi_{j,k} \rangle \varphi_{j,k} = \sum_{k=-\infty}^{\infty} c_{j,k}\varphi_{j,k} \tag{3.17}$$

where $c_{j,k}$ are the *approximation coefficients*. In accordance with Equation (3.14), the projection of f onto V_{j-1} can be written as

$$P_{j-1} f = P_j f + Q_j f. \tag{3.18}$$

This forms the basis of multi-resolution analysis associated with DWT. Since $W_j \perp V_j$ and $W_{j-1} \perp (V_j \oplus W_j)$, it can be concluded that $W_j \perp W_{j-1}$ and hence, each level of wavelet subspace is orthogonal to every other level. Thus, the wavelet functions $\psi_{j,k}$ are orthogonal for all $j, k \in \mathbb{Z}$. Multi-resolution analysis breaks down the original $\mathbb{L}^2(\mathbb{R})$ into a set of orthogonal subspaces at different scales. Designing appropriate basis functions ψ and φ with specific properties is the problem solved by Daubechies [1988] for the first time, and is now used widely in various applications.

3.2.2 Daubechies Compactly-supported Wavelets

The orthonormal bases of compactly-supported wavelets are designed based upon a set of desirable properties for MRA. The wavelet function ψ and its

companion, the scaling function φ, are governed by a set of N filter coefficients $\{a_k; k = 0, 1, \cdots, N-1\}$ through the two-scale relation:

$$\varphi(t) = \sum_{k=0}^{N-1} a_k \varphi(2t-k) \tag{3.19}$$

and its counterpart

$$\psi(t) = \sum_{k=0}^{N-1} (-1)^k a_{1-k} \varphi(2t-k) \tag{3.20}$$

which ensures that ψ is orthogonal to φ. These equations are set up by expressing the space V_0 in terms of the basis of V_{-1}, c.f. Equation (3.11). The constant N is known as the *wavelet order* and must be an even integer [Daubechies, 1992]. The support of φ is $[0, N-1]$, whereas the support of the corresponding wavelet ψ is $[1-\frac{N}{2}, \frac{N}{2}]$. The filter coefficients a_k are derived by imposing certain conditions established by Daubechies:

$$\sum_{k=0}^{N-1} a_k = 2 \tag{3.21}$$

$$\sum_{k=0}^{N-1} a_k a_{k-m} = \delta_{0m}; \forall m \in \mathbb{Z} \tag{3.22}$$

$$\sum_{k=0}^{N-1} (-1)^j a_{1-k} a_{k-2m} = 0; \forall m \in \mathbb{Z} \tag{3.23}$$

$$\sum_{k=0}^{N-1} (-1)^k k^m a_k = 0; \forall m \in 0, 1, \cdots, \frac{N}{2} - 1. \tag{3.24}$$

These coefficients are fixed for a specific wavelet or scaling function basis and need to be calculated only once. Equations (3.21) to (3.24) are essentially extracted from the following properties of the scaling and the wavelet functions.

$$\int_{-\infty}^{\infty} \varphi(t) dt = 1 \tag{3.25}$$

$$\int_{-\infty}^{\infty} \psi(t) dt = 0 \tag{3.26}$$

$$\int_{-\infty}^{\infty} \varphi(t-k)\varphi(t-j) dt = \delta_{kj} \tag{3.27}$$

$$\int_{-\infty}^{\infty} \varphi(t)\psi(t-m) dt = 0 \tag{3.28}$$

$$\int_{-\infty}^{\infty} t^n \psi(t) dt = 0; n = 0, 1, \cdots, \frac{N}{2} - 1, \tag{3.29}$$

where $j, k, m \in \mathbb{Z}$. The first two equations above are extracted from the admissibility condition as presented earlier in Section 3.1. Equation (3.27) represents the orthogonality of the scaling function under translation, and Equation (3.28) expresses the orthogonality of φ and ψ. Finally, Equation (3.29) states that the moments of the wavelet function are zero up to a certain order. This equation imposes that the set $\left\{1, t, \cdots, t^{N/2-1}\right\}$ is a linear combination of the integer translates of the scaling function, i.e. $\varphi(t-k)$. The exact expression for such a linear combination is given in Appendix B. The orthogonal properties of the scaling function and the wavelet function can be stated in the MRA framework as follows [Chen et al., 1996]:

$$\int_{-\infty}^{+\infty} \varphi_{j,k}\varphi_{j,l}dt = \delta_{lk} \tag{3.30}$$

$$\int_{-\infty}^{+\infty} \psi_{j,k}\psi_{l,m}dt = \delta_{jl}\delta_{km} \tag{3.31}$$

$$\int_{-\infty}^{+\infty} \varphi_{j,k}\psi_{j,m}dt = 0 \tag{3.32}$$

for $j, k, m \in \mathbb{Z}$. It is known that there are no explicit expressions for calculating the values of the scaling function and the corresponding wavelet function at an arbitrary point [Daubechies, 1992]. However, the function values of φ and ψ at dyadic points can be recursively computed from the two-scale relations (3.19) and (3.20). The algorithms used to obtain these values at integer points are given in Appendix B.

3.3 Wavelets For Solution of PDEs

The fact that Daubechies wavelets Daubechies [1992] possess several appealing properties such as orthogonality, compact support, exact representation of polynomials up to a certain degree, and ability of representing functions at different resolutions, has resulted in an extensive use of wavelets in solving PDEs [Amaratunga and Williams, 1997, Amaratunga et al., 1994, Beylkin, 1992, Chen and Hwang, 1996, Chen et al., 1996, Qian and Weiss, 1993]. The formulation is essentially derived through the wavelet collocation method (WCM) [Harten, 1994] or the wavelet-Galerkin method (WGM) [Qian and Weiss, 1993].

Daubechies wavelets are known as desirable bases for the Galerkin solution of PDEs [Amaratunga and Williams, 1997, Chen et al., 1996, Qian and Weiss, 1993]. They are orthogonal with compact support, and the integral of their product can be computed exactly. The efficiency of the WGM has been demonstrated repeatedly in various disciplines such as for Navier-Stokes equations [Qian and Weiss, 1993], Helmholtz equations [Qian and Weiss, 1993], Burgers equation [Chen and Hwang, 1996], and the population balance problem [Chen et al., 1996]. The spectral convergence of the WGM has been demonstrated by Qian and Weiss [1993] for various types of PDEs. The focus of this dissertation is also on the WGM, the details of which are explained in the present chapter.

3.3.1 Spectral Analysis Using Wavelets

The idea behind using wavelets to solve PDEs is similar to the Fourier-based spectral analysis: transformation of the elastodynamic equations expressing the wave motion from the time domain to another domain in which an accurate approximation of the displacement field can be sought. This is done in accordance with an extended version of the single-scale WGM presented by Mitra and Gopalakrishnan [2005], which does not utilize the MRA, but decouples the equations in the transformed domain. An elaborate, computationally-improved, and generalized formulation of the method called the decoupled wavelet-Galerkin approach (DWG) is outlined in this dissertation.

3.4 The Single-scale Wavelet-Galerkin Method

The wavelet-Galerkin method has been extensively applied to solving PDEs on regions with strong gradients due to its orthogonality characteristics, exact representation of polynomials up to a certain order, and compact support of Daubechies wavelets [Amaratunga and Williams, 1997, Chen and Hwang, 1996, Qian and Weiss, 1993]. A concise description of the method is provided in this section.

Consider a domain Ω and assume the arbitrary scalar function $f : (\Omega, t) \rightarrow \mathbb{R}$ to be discretized at L equally-spaced points in time separated by the time interval Δt. In order to avoid dealing with wavelet parameters at non-integer points, the dimensionless time τ can be utilized [Mitra and Gopalakrishnan, 2005] such that,

$$t_\tau = \tau \Delta t \ , \forall \tau \in [0, L-1]. \tag{3.33}$$

The single-scale approximation of the temporal behavior of f can be achieved at the resolution level zero. In this way, one only deals with the approximation coefficients, since the translates of φ span the whole function space (Figure 3.2) and therefore, can be used as a basis to approximate f [Amaratunga and Williams, 1997]:

$$f \approx \tilde{f} = \sum_k \hat{f}_k \varphi_{0,k} = \sum_k \hat{f}_k \varphi_k \ , \ k \in \mathbb{Z}. \tag{3.34}$$

In the above equation, $\varphi_k = \varphi(\tau - k)$ and $\hat{f}_k : \Omega \rightarrow \mathbb{R}$ are the weights of the translated functions, i.e. the approximation coefficients. For simplicity in notations, the translation of the scaling function at the resolution level zero, i.e. $\varphi_{0,k}$, is shown by φ_k. It is known that, the scaling function of the compactly-supported wavelets is nonzero only at $N-2$ points, i.e. $\varphi(\tau - k) \neq 0$ for $\tau - k = 1, 2, \cdots, N-2$ [Amaratunga and Williams, 1997]. The matrix representation of Equation (3.34) will therefore, have a bandwidth of $N-2$. Note that the smoothness of the scaling function increases as the order of the wavelets grows. As mentioned earlier, the scaling function of compactly-supported wavelets can be evaluated at integer points using the algorithms presented in Appendix B.

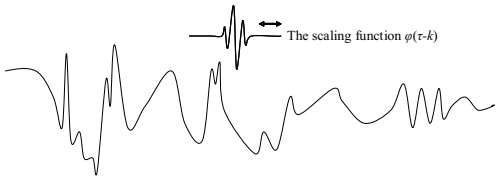

Figure 3.2: Translation of a single scaling function to approximate a transient function.

For a system of linear PDEs, each of the form $\mathfrak{F}(f^1, \frac{\partial f^2}{\partial t}, \frac{\partial^2 f^3}{\partial t^2}, \cdots) = 0$ with $f^i : (\Omega, t) \to \mathbb{R}$, the functions f^i can be expressed in terms of the approximation coefficients according to Equation (3.34):

$$\tilde{f}^i = \sum_k \hat{f}^i_k \varphi_k \ , \ \forall i \in [0, 1, 2, \cdots] \ , \ k \in \mathbb{Z}. \tag{3.35}$$

An approximation to the solution can be subsequently obtained in a Galerkin sense. To determine the unknown approximation coefficients, the WGM projects the resulting expression onto the subspace spanned by the translates of the scaling function acting as the test functions, i.e.:

$$\int_{\mathfrak{T}} \mathfrak{F}(\tilde{f}^1, \frac{\partial \tilde{f}^2}{\partial t}, \frac{\partial^2 \tilde{f}^3}{\partial t^2}, ...)\varphi_j d\tau = 0 \ , \forall j \in [0, 1, ..., L-1], \tag{3.36}$$

where $\mathfrak{T}$ defines the integral bounds. Some functionals known as *connection coefficients* result from substitution of Equation (3.35) in Equation (3.36) [Amaratunga and Williams, 1997, Qian and Weiss, 1993]:

$$\Gamma^n_{k-j} = \left\langle \varphi^{(n)}_k, \varphi_j \right\rangle, \forall k \in \mathbb{Z}, \ j \in [0, 1, \cdots, L-1]. \tag{3.37}$$

In the above equation, the superscript (n) denotes the nth derivative with respect to time, and $\langle ., . \rangle$ is the the inner product, i.e. $\langle f, g \rangle = \int_{\mathfrak{T}} f(\tau) g^*(\tau) d\tau$ with * reflecting the complex conjugate of the corresponding function. Since the derivatives of the compactly-supported wavelets are highly oscillatory, numerical quadrature techniques for computing the connection coefficients are mostly unstable or inaccurate [Amaratunga and Williams, 1997, Qian and Weiss, 1993] and it is therefore necessary to evaluate them exactly.

The connection coefficients are, in general, functions of $\mathfrak{T}$. Depending on the choice of the integration domain $\mathfrak{T}$, some values of the approximated function may be required that lie outside of the window of interest. This issue is known as the *edge effects* of the wavelets, and will be discussed in detail in sections 3.6 and 3.7.

3.5 The Decoupled Wavelet-Galerkin Method

A generic formulation of the WGM for wave propagation problems is introduced in this section. The equations of motion can be expressed in a general form of

a system of linear PDEs in space and time as:

$$\mathfrak{L}\mathbf{u} + \mathbf{f} = \mathcal{J}\ddot{\mathbf{u}} \tag{3.38}$$

where, in the present study, $\mathfrak{L}$ is a linear continuous differential operator that reflects the elastic properties of the medium, $\mathcal{J}$ is a matrix containing the inertial properties of the medium, and $\mathbf{u} = (u^1, u^2, \cdots, u^m)^T$ denotes the vector of m dependent variables, i.e. displacements and rotations. The vector $\mathbf{f} = (f^1, f^2, \cdots, f^m)^T$ specifies the given external forces. In accordance with Equation (3.34), the single-scale approximation of Equation (3.38) can be expressed as a system of PDEs in space only:

$$\mathfrak{L}\sum_k \hat{\mathbf{u}}_k\varphi_k + \sum_k \hat{\mathbf{u}}_k\varphi_k = \mathcal{J}\sum_k \hat{\mathbf{u}}_k\ddot{\varphi}_k \ , \ k \in \mathbb{Z}. \tag{3.39}$$

Since the differential operator $\mathfrak{L}$ is linear, it will be later moved inside the summation. Application of the WGM to the equation (3.38) requires taking the inner product of both sides of Equation (3.39) by ϕ_j:

$$\sum_k \left(\mathfrak{L}\hat{\mathbf{u}}_k + \hat{\mathbf{f}}_k\right)\langle\varphi_k, \varphi_j\rangle = \frac{1}{\Delta t^2}\sum_k \mathcal{J}\hat{\mathbf{u}}_k\langle\ddot{\varphi}_k, \varphi_j\rangle, \forall j \in [0, 1, \cdots, L-1] \tag{3.40}$$

which, using connection coefficients of Equation (3.37), can be rewritten as follows:

$$\sum_k \left(\mathfrak{L}\hat{\mathbf{u}}_k + \hat{\mathbf{f}}_k\right)\Gamma^0_{k-j} = \frac{1}{\Delta t^2}\sum_k \mathcal{J}\hat{\mathbf{u}}_k\Gamma^2_{k-j}. \tag{3.41}$$

For the sake of efficiency in notation, the above system of m PDEs is rearranged; by forming the $m \times L$ matrices $\hat{\mathbf{U}}$ and $\hat{\mathbf{F}}$ such that $\hat{\mathbf{U}}[\mu, p] = u^\mu_p$ and $\hat{\mathbf{F}}[\mu, p] = f^\mu_p$, with $\mu \in [1, 2, \cdots, m]$ and $p \in [1, 2, \cdots, L]$ respectively being the row number and the column number, Equation (3.41) can be presented as follows:

$$\mathbf{\Gamma}_0\left(\mathfrak{L}\hat{\mathbf{U}} + \hat{\mathbf{F}}\right)^T = \frac{1}{\Delta t^2}\mathbf{\Gamma}_2\left(\mathcal{J}\hat{\mathbf{U}}\right)^T. \tag{3.42}$$

In the above equation, $\mathbf{\Gamma}_0$ and $\mathbf{\Gamma}_2$ are $L \times L$ band-limited matrices the components of which are the values of connection coefficients Γ^0_{k-j} and Γ^2_{k-j}, respectively. The independence of the discrete temporal operators, i.e. $\mathbf{\Gamma}_0$ and $\mathbf{\Gamma}_2$, from the spatial operator $\mathfrak{L}$ can be understood from Equation (3.42); the spatial operator does not influence the construction of the temporal operators. Furthermore, since the orthogonality condition (3.27) holds only if $\mathfrak{T} = [-\infty, +\infty]$, $\mathbf{\Gamma}_0$ is, in general, not an identity matrix as the integral domain $\mathfrak{T}$ for the computation of connection coefficients can be chosen arbitrarily.

Equation (3.42) is a coupled system of L homogenous PDEs. The bandwidth of the matrix $\mathbf{\Gamma}_2$, which shows how the dependent variables, i.e. displacements, at different times are connected, is determined by the order of the compactly-supported wavelets N. Higher-order wavelets correlate more time steps through a wider matrix band. These matrices are however, independent of the material or geometrical properties of the problem. The coupled equations can be

decoupled through the eigen-decomposition of $\mathbf{\Gamma}_0^{-1}\mathbf{\Gamma}_2$. The projection of the approximation coefficients matrix $\hat{\mathbf{U}}$ on the eigen-space of $\mathbf{\Gamma}_0^{-1}\mathbf{\Gamma}_2$ is denoted by an overbar and can be accordingly expressed as:

$$\bar{\mathbf{U}}^T = \mathbf{\Phi}^{-1}\hat{\mathbf{U}}^T \tag{3.43}$$

where $\mathbf{\Phi}$ is the eigen-vector basis of $\mathbf{\Gamma}_0^{-1}\mathbf{\Gamma}_2$. It is apparent that the decoupling process depends only on the number of sampling points in time. For the sake of computational efficiency, the eigen-vectors and eigen-values can be stored when the number of sampling points is large. Using Equation (3.43) and standard algebra, Equation (3.42) can be rewritten as:

$$\mathbf{\Phi}^{-1}\left(\mathfrak{L}\hat{\mathbf{U}} + \hat{\mathbf{F}}\right)^T = \frac{1}{\Delta t^2}\mathbf{\Phi}^{-1}\left(\mathbf{\Gamma}_0^{-1}\mathbf{\Gamma}_2\right)\mathbf{\Phi}\,\mathbf{\Phi}^{-1}\left(\mathcal{J}\hat{\mathbf{U}}\right)^T. \tag{3.44}$$

and further simplified to:

$$\mathfrak{L}\bar{\mathbf{U}} + \bar{\mathbf{F}} = \frac{1}{\Delta t^2}\mathcal{J}\bar{\mathbf{U}}\mathbf{\Lambda}, \tag{3.45}$$

where $\mathbf{\Lambda}$ is the eigen-value matrix of $\mathbf{\Gamma}_0^{-1}\mathbf{\Gamma}_2$, the jth component of which will be denoted by κ_j^2. From Equation (3.45), the transformed form of the equations of motion corresponding to each $j \in [0, 1, \cdots, L-1]$, can be expressed as a linear relation between the jth column of $\bar{\mathbf{U}}$ and the jth column of $\bar{\mathbf{F}}$, and finally presented as:

$$\mathfrak{L}\bar{\mathbf{u}}_j + \bar{\mathbf{f}}_j = \bar{\omega}_j^2\mathcal{J}\bar{\mathbf{u}}_j, \tag{3.46}$$

where

$$\bar{\omega_j} = \frac{\kappa_j}{\Delta t}\ ,\ j \in [0, 1, \cdots, L-1], \tag{3.47}$$

is the DWG frequency. The term jth *wavelet point* will be used hereafter to indicate the solution associated with κ_j.

Using the DWG, the transient problem is now broken down into a set of temporally uncoupled stationary PDEs which can be solved in parallel at the different wavelet points. A linear combination of the transformed responses at the wavelet points weighted in accordance with equations (3.43) and (3.35) brings the response back into the real time.

The independence of the solution steps may seem surprising at the first glance, however, in analogy with the Fourier domain analysis and modal superposition techniques, the solution in time is a weighted superposition of the system response to a set of virtual frequencies defined at the discrete wavelet points. Mathematically speaking, there exists a subspace onto which temporally-linear-second-order equations can be projected and appear in a decoupled fashion. The eigen-values of the projection scaled by the reciprocal of the time interval specify the virtual frequencies.

It has to be pointed out that since $\mathbf{\Gamma}_0^{-1}\mathbf{\Gamma}_2$ is not symmetric, its eigen-values are, in general, complex numbers. This however, is not a problematic issue and can be handled in a straight-forward manner, as will be discussed in the following section.

3.6 Periodic and Non-periodic Conditions

Accurate computation of the connection coefficients is of a great importance in the WGM. The highly oscillatory nature of the scaling function makes standard numerical quadrature of integrals impractical. Latto et al. [1991] developed a procedure to compute the connection coefficients in Equation (3.37) over an unbounded domain, i.e. $[-\infty, \infty]$. This procedure has been used extensively in the WGM [Amaratunga and Williams, 1997, Amaratunga et al., 1994, Mitra and Gopalakrishnan, 2006d, 2007, 2005, 2006a,b]. If the integration domain in Equation (3.37) is unbounded, by expanding equation (3.41), edge effects appear on both the left and right hand sides of the time window of interest, and need to be dealt with carefully. The edge effects in this case are associated with $N-2$ terms in the connection coefficients which correspond to $N-2$ out-of-range indices at each side of the time window.

Accounting for the out-of-range values is generally an approximate procedure, unless there are certain conditions at the boundaries such as periodicity, symmetry or antisymmetry. Assuming periodicity is the simplest way to tackle such problems; however, it may lead to inaccurate results for non-periodic conditions. Amaratunga and Williams introduced an extrapolation technique to mitigate the edge effects [Amaratunga et al., 1994]. Although this scheme may be efficient in some applications, its accuracy depends highly on the type of the problem and initial/boundary conditions.

3.7 Edge Effects Removal

An improved scheme for dealing with the edge effects of the wavelet-Galerkin method is suggested in this research, which operates based on the computation of the connection coefficients of compactly-supported wavelets in Equation (3.37) on a finite domain. To clarify the concept, the connection coefficients in Equation (3.37) can be first written in a non-compact form as:

$$\left\langle \varphi_k^{(n)}, \varphi_j \right\rangle_{\mathfrak{T}} = \int_0^{\xi} \varphi^{(n)}(\tau - k)\varphi(\tau - j)d\tau, \forall k \in \mathbb{Z},\ j \in [0, 1, \cdots, L-1], \quad (3.48)$$

where $\mathfrak{T} \in [0, \xi]$, and indicates the integration domain. To compute the values of the above integral, the change of variables $\eta = \tau - j$ is applied. This results in:

$$\left\langle \varphi_k^{(n)}, \varphi_j \right\rangle_{\mathfrak{T}} = \int_{-j}^{\xi-j} \varphi^{(n)}(\eta - [k-j])\varphi(\eta)d\eta. \quad (3.49)$$

Equation (3.48), in which the integral bounds are updated according to the new variable η, can be split into two parts by subdividing the integration domain as follows:

$$\left\langle \varphi_k^{(n)}, \varphi_j \right\rangle_{\mathfrak{T}} = -\int_0^{-j} \varphi^{(n)}(\eta - [k-j])\varphi(\eta)d\eta + \int_0^{\xi-j} \varphi^{(n)}(\eta - [k-j])\varphi(\eta)d\eta. \quad (3.50)$$

The first term in Equation (3.50) vanishes in accordance with Equation (B.12) in Appendix B, hence,

$$\int_0^{\xi-j} \varphi^{(n)}(\eta - [k-j])\varphi(\eta)d\eta = \Gamma^n_{k-j}, \tag{3.51}$$

where $\Gamma^n_{k-j} : \xi - j \to \mathbb{R}$, is obtained from the definition given in Equation (B.10). From Equation (3.49), the properties of the connection coefficients of Daubechies wavelets over finite intervals in equations (B.11) to (B.14), and Equation (3.51), it was understood that if $\xi = L$, where L is the number of temporal sampling points, all the connection coefficients at the right-hand side of the time window, i.e. $k > L-1$, become zero, see property (B.12). At the left-hand-side of the time window, the number of out-of-range values of the connection coefficients does not change compared to the case which is based on the infinite integration domain, i.e. $N-2$ out-of-range indices of the approximation coefficients are still needed to be known. However, since these values lie only at the left-hand-side of the window of interest, for zero initial conditions, the out-of-range components can be discarded. As a consequence, the matrix equation (3.42) becomes free of edge effects and the accuracy of the DWG improves, as will be demonstrated later in this section. For non-zero initial conditions, the method of wavelet extrapolation [Williams and Amaratunga, 1997] or the capacitance matrix method [Qian and Weiss, 1993] can be adopted. Since zero initial conditions are plausible for SHM applications of wave propagation, this assumption will be made throughout this dissertation.

To computed the connection coefficients on a bounded domain, the technique used by Chen and Hwang [1996] and Chen et al. [1996] for the solution of the Burger's equation and the population-balance problem is utilized. The procedure to calculate the connection coefficients is outlined in Appendix B. It seems that since Chen and Hwang used the WGM for spatial transformations, in which incorporation of natural and essential boundary conditions at both sides of the domain was crucial, the potential contribution of computing the connection coefficients over a bounded domain in an edge effect removal scheme was not realized or not viewed as significant in their work.

It is illustrated in Figure 3.3 how the connection coefficients are assembled as components of a matrix, if Equation (3.37) has an unbounded integration domain. In this case, r, which is the number of components corresponding to out-of-range values at each side of the physical domain, will be $N-2$ [Beylkin, 1992, Williams and Amaratunga, 1997] and the sub-matrix $\mathbf{Q}^c$ will be a Toeplitz, i.e. diagonal-constant, matrix. Alternatively, and as mentioned above, computation of the connection coefficients over the finite dimensionless time window $[0, L]$ ensures that all the components of the sub-matrix $\mathbf{Q}^R$ vanish. In addition, $\mathbf{Q}^c$ is no longer a Toeplitz matrix, however, the number of out-of-range values at the left-hand-side, i.e. r, does not change.

A quantitative comparison between the periodic connection coefficients, the extrapolated connection coefficients, and the present method, in terms of the condition number of $\mathbf{\Gamma}_0^{-1}\mathbf{\Gamma}_2$ is provided, as shown in Figure 3.4 and Figure

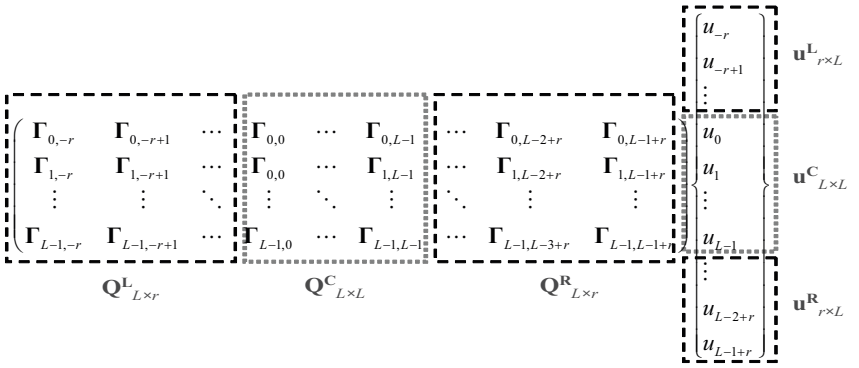

Figure 3.3: Representation of the out-of-range components.

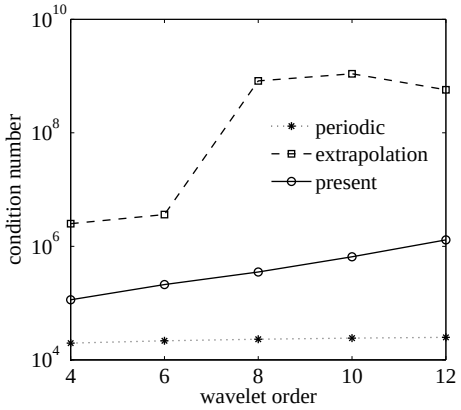

Figure 3.4: Dependence of the condition number of $\mathbf{\Gamma}_0^{-1}\mathbf{\Gamma}_2$ on the wavelet orders for $L = 200$.

3.5[4], and has been computed based on the $l2$-norm of $\mathbf{\Gamma}_0^{-1}\mathbf{\Gamma}_2$. The periodic boundary conditions and the extrapolated boundary conditions were considered in accordance with the coefficients computed over an unbounded domain, as a result of which $\mathbf{\Gamma}_0$ becomes an identity matrix due to the orthogonality of the scaling functions. From the dependence of the condition number of $\mathbf{\Gamma}_0^{-1}\mathbf{\Gamma}_2$ on the order of the compactly-supported wavelet demonstrated in Figure 3.4, the superior behavior of the present method over the extrapolation scheme can be observed. Although the periodic case has a smaller condition number that is virtually independent of the wavelet order, it is only applicable to very specific problems. The direct relationship between the wavelet order and the condition

[4]If the condition number is very large, the matrix is so-called ill-conditioned and may be almost singular. Computation of the inverse, or solution of a linear system of equations for an ill-conditioned system is prone to large numerical errors. A non-invertible matrix has the condition number equal to infinity.

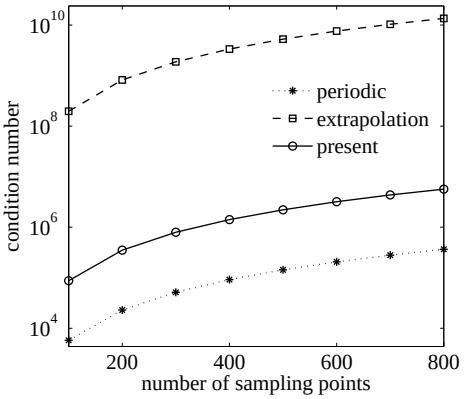

Figure 3.5: Dependence of the condition number of $\mathbf{\Gamma}_0^{-1}\mathbf{\Gamma}_2$ on the number of temporal nodes for $N = 8$.

number of interest suggests that, although the properties of the approximation basis improve with the wavelet order, from a computational point of view, the wavelet order should be kept small. Otherwise, preconditioning techniques may be required. The effect of the number of sampling points on the condition number of $\mathbf{\Gamma}_0^{-1}\mathbf{\Gamma}_2$ depicted in Figure 3.5 for $N = 8$ shows a similar trend to that shown in Figure 3.4, i.e. the extrapolation scheme is characterized by the highest condition number, followed by the present scheme and the periodic scheme.

3.8 Implementation and Applications - The 1D Wave Equation

The WGM and the required considerations for implementation of the method were discussed in the previous sections. In order to clarify the concept, the WGM will now be applied to solving the 1D wave equation in a linear solid:

$$\frac{\partial^2 u}{\partial x^2} + f = \frac{1}{c^2}\frac{\partial^2 u}{\partial t^2} \tag{3.52}$$

where $c = \sqrt{E/\rho}$ is the wave speed with E and ρ being the Young's modulus and the material density, respectively, and f is the applied force. Discretizing Equation (3.52) temporally at L points and using the DWG, it can be presented at the jth wavelet point as

$$\frac{d^2\bar{u}_j}{dx^2} + \bar{f}_j = \frac{\bar{\omega}_j^2}{c^2}\bar{u}_j. \tag{3.53}$$

The homogeneous solution of the above equation is:

$$\bar{u}_j(x) = C_1 e^{k_j x} + C_2 e^{-k_j x} \; ; k_j = \frac{\bar{\omega}_j}{c}. \tag{3.54}$$

The constants C_1 and C_2 are determined in accordance with the boundary conditions. At an arbitrary location, the axial load can be written as:

$$\bar{f}_j(x) = EA\frac{d\bar{u}_j}{dx} = EAk_j\bar{u}_j(x) \tag{3.55}$$

where A denotes the cross-section area of the bar. If an element with length l and two nodes at $x = 0$ and $x = l$ is assumed, the nodal forces $\bar{\mathbf{f}}_j = [\bar{f}_j(0), \bar{f}_j(l)]^T$ can be connected to the nodal displacement vector $\bar{\mathbf{u}}_j = [\bar{u}_j(0), \bar{u}_j(l)]^T$ via a dynamic stiffness matrix $\bar{\mathbf{K}}_j$:

$$\begin{aligned} \bar{\mathbf{f}}_j &= EAk_j \begin{pmatrix} 1 & -1 \\ e^{k_j l} & -e^{-k_j l} \end{pmatrix} \begin{pmatrix} C_1 \\ C_2 \end{pmatrix} \\ &= EAk_j \begin{pmatrix} 1 & -1 \\ e^{k_j l} & -e^{-k_j l} \end{pmatrix} \begin{pmatrix} 1 & 1 \\ e^{k_j l} & e^{-k_j l} \end{pmatrix}^{-1} \bar{\mathbf{u}}_j = \bar{\mathbf{K}}_\mathbf{j}\bar{\mathbf{u}}_j. \end{aligned} \tag{3.56}$$

The significant advantage of the wavelet-based approach over the standard FEM is that the dynamic stiffness matrix is constructed from the exact solution of the wave equation. As a consequence, as long as there is no discontinuity in the waveguide, a single element can capture the motion exactly, irrespective of the length of the waveguide. Note that the solution of the finite element formulation needs to be transformed back to the space of the wavelets approximation coefficients in accordance with Equation (3.43), and subsequently to real time according to (3.35).

For numerical verification of the present approach, consider an aluminum beam with $E = 70$ GPa and $\rho = 2700$ Kg/m^3. The beam properties are uniform along the length. To demonstrate the improvements of the present method to previous studies, the spurious oscillations appearing in the response were studied. The spurious oscillations appear as a consequence of a low-quality discretization, i.e. an insufficient temporal sampling rate. The solution obtained from the exact computation of the connection coefficients was compared to the solution from the wavelet extrapolation scheme [Mitra and Gopalakrishnan, 2005]. It is noted that the spatial formulation characterized by the dynamic stiffness matrix was similar in both approaches.

The velocity response of the structure subjected to a modulated triangular load pulse with duration of $50\mu s$, which does not have significant frequency components beyond 50 kHz, is illustrated in figures 3.6 and 3.7. The order of the compactly-supported wavelets N is 8 in both figures, whereas the number of temporal sampling points L is 100 in Figure 3.6 and 300 in Figure 3.7.

The reduction in the amplitude of the spurious oscillations in result of using the presented edge effect removal scheme compared to the extrapolation-based scheme [Mitra and Gopalakrishnan, 2005] is demonstrated in Figure 3.6. As shown in Figure 3.7, the difference between the two methods is less pronounced

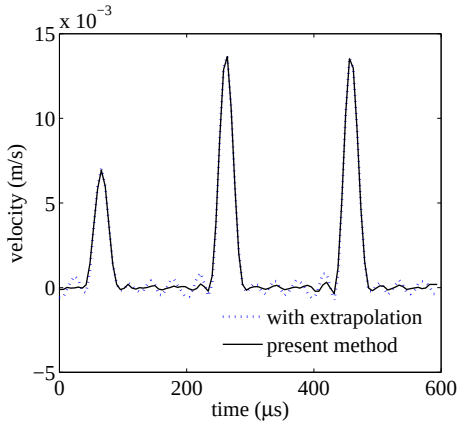

Figure 3.6: Comparison of the present method with the extrapolation-based method [Mitra and Gopalakrishnan, 2005] for $N = 8$ and $L = 100$.

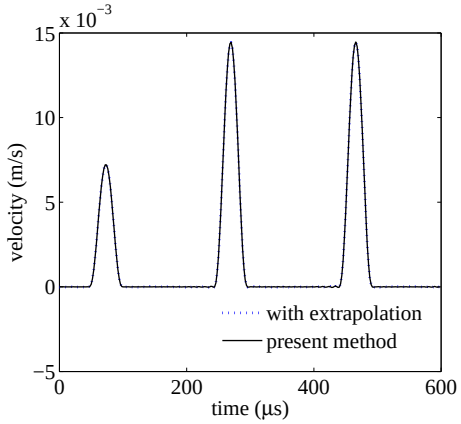

Figure 3.7: Comparison of the present method with the extrapolation-based method [Mitra and Gopalakrishnan, 2005] for $N = 8$ and $L = 300$.

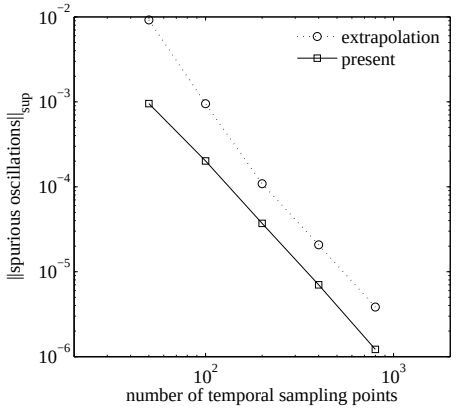

Figure 3.8: The dependence of the amplitude of spurious oscillations on the number of sampling points for $N = 6$.

at higher sampling rates for $L = 300$. It is worthwhile to note that in simulation of propagation of ultrasonic waves in structures and their interaction with structural discontinuities, the spurious oscillations should be sufficiently small in magnitude, i.e. the signal-to-noise ratio should be large enough, to allow distinguishing them from scatterings of waves due to the defects.

In order to quantitatively compare the edge effect removal scheme for different number of temporal sampling points, a sup-norm measure[5] of the spurious oscillations was adopted. The comparison, as shown in Figure 3.8, reveals that for a fixed wavelet order and discretization, a significant computational saving can be achieved using the presented improved scheme for computation of the connection coefficients. Although the sup-norm of the spurious oscillations spectrally decays by increasing the sampling rate in both schemes, the present method requires nearly 50% of the temporal sampling points used in the extrapolation-based results. This can be of a great importance in higher-dimension structures, which will be studied further in this dissertation.

3.9 Concluding Remarks and Extension to Higher Dimensions

The theory of the wavelet transform and the wavelet-Galerkin method were elaborately discussed in this chapter. The decoupling of the linear wave equations with respect to the temporal variable was demonstrated using the wavelet-Galerkin method applied to a generic form of linear second-order PDEs with

[5] On an n-dimensional Euclidean space $\mathbb{R}^n$, the sup-norm of the vector $\mathbf{x} = (x_1, x_2, \cdots, x_n)$ is given by:

$$\|\mathbf{x}\|_{sup} = \max\left(|x_1|, |x_2|, \cdots, |x_n|\right).$$

respect to time. Furthermore, an improved scheme for computation of the derivative operators in the wavelet-Galerkin method was presented, with which, for a certain accuracy level, a significant reduction in the number of sampling points compared to the conventional approach was achieved. This improved scheme will be applied to the temporal discretization of linear wave equations in the remaining of this dissertation. In the next chapter, the decoupled wavelet-Galerkin approach will be applied to a 1D formulation of the wavelet-based spectral finite element method that includes shear deformation, rotary inertia, and thickness contraction effects in composite beam-like structures.

Regarding the extension of the method to higher-dimensional problems, as discussed in Chapter 2, the conventional transformed domain methods employ successive transformations over the temporal and spatial coordinates until they are left with a set of ODEs that can be solved exactly [Doyle, 1989, Gopalakrishnan et al., 2008, Gopalakrishnan and Mitra, 2010]. Although some major difficulties in using the Fourier transform that result from the periodicity assumption and the global non-compactly-supported basis, can be eliminated by employing the DWG, as suggested by Amaratunga and Williams [1997] and Gopalakrishnan and Mitra [2010], and improved by the present work, there are still difficulties with dealing with 2D and 3D problems which have geometrical complexities and non-periodic boundary conditions [Mitra and Gopalakrishnan, 2006d, 2008]. This issue will be dealt with in depth in this dissertation and novel solutions will be presented in chapters 5 and 6 to deal with engineering structures.

Chapter 4

Wavelet-based Spectral Finite Element Method for Modeling One-dimensional Waveguides

As a result of the growing application of composite stringers, frames, and stiffened structures in the aerospace industry, the need to develop computationally-efficient models for analysis and simulation of ultrasonic wave propagation in these structures is pronounced for structural health monitoring (SHM) purposes. From a wave propagation point of view, these structures are typically 1D waveguides, i.e. guided waves propagate only in one direction, although the material motion may be in more than one dimension. Despite the applicability of 3D models to simulate such waveguides, their computational cost may not be justified for many SHM applications.

In order to develop efficient and fast simulation tools, simplifying assumptions on the description of the displacement fields are usually made. The accuracy of these assumptions, as mentioned in Chapter 2, declines at higher frequencies since the assumed displacement fields are not sufficiently rich anymore to capture higher order wave modes. The primary goal of an optimized simulation tool is to keep the computation time as low as possible, while a reasonable accuracy level is preserved. For reducing the model, inaccurate assumptions which are not valid in the frequency range of interest may result in a significant mismatch between the numerical results and experiments, thereby degrading the performance of the model-based identification schemes of SHM or non-destructive testing (NDT).

Despite the extensive studies on the propagation of guided ultrasonic waves in doubly-bounded waveguides[1] e.g. composite plates and shells as discussed in

[1] In doubly-bounded waveguides, waves can only propagate between the two free surfaces

Chapter 2, it is believed that the study of wave propagation in composite beams and rings acting as quadruply-bounded waveguides is not adequately addressed so far (the term quadruply-bounded waveguides denotes the wavelength is of the same order as the beam height and width). The semi-analytical finite element method (SAFEM), also known as the waveguide finite element method, may be regarded as the most notable procedure developed for analysis of quadruply-bounded waveguides [Hayashi et al., 2006, Bartoli et al., 2006]. The SAFEM assumes harmonic motion in the lengthwise direction and employs finite element discretization over the cross-section of the waveguide. Although the SAFEM can handle the analysis of the wave propagation in an infinitely long waveguide, simulation of wave motion in in bounded waveguides using SAFEM does not seem to be straight-forward.

For the simulation of wave propagation in straight composite beams (with and without delamination), a model based on the Fourier-based spectral finite element method (FSFEM) was presented by Gopalakrishnan et al. [2008], which takes shear deformation and thickness contraction effects into account. A similar model but with neglecting the thickness contraction effect was later implemented using the wavelet-based spectral finite element method (WSFEM) [Mitra and Gopalakrishnan, 2006c]. Among other works on delamination modeling in composite straight beams for SHM applications, the studies carried out by Mahapatra and Gopalakrishnan [2004], Nag et al. [2003], and Palacz et al. [2005b] are also of interest. It seems that the influence by the curvature, which can add new coupling terms to the final equations, has not been addressed in the literature.

In Chapter 3, a wavelet-based spectral formulation was shown for a simple bar example, in which both the material deformation and the waveguide were one-dimensional. In the present chapter, a 1D model is formulated for wave propagation analysis and simulation in composite beam-like structures, with displacement components defined in three dimensions. By studying the dispersion relations, the improvement by the proposed model, which considers the contraction effect in the width-wise direction in addition to the thickness-wise direction, is presented. To simulate the propagation of fundamental wave modes in a curved anisotropic waveguide, the wavelet-based spectral finite element method (WSFEM) is employed. The governing equations transformed through the wavelet-Galerkin method are solved exactly. The wave motion can hence be captured exactly in the absence of discontinuities, irrespective of the waveguide length. Furthermore, a model with structural discontinuities that can be viewed as piecewise continuous structure can be modeled with the minimum number of finite elements. This approach can bring a substantial reduction in the solution time, in comparison with the standard FEM. Furthermore, a delamination model is implemented whereby the effects of curvature, shear deformation, rotary inertia and thickness contraction in two planes are taken into account. The delamination model is developed by assuming that the cross-section is split into two parts, which are subsequently connected by means of

of the waveguide, e.g. plates.

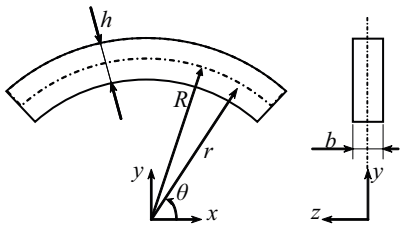

Figure 4.1: A schematic view of the curved beam element.

compatibility conditions. In order to verify the performance of the method and demonstrate the features, some numerical examples of delaminated composite beams and rings are provided in the end.

4.1 A General Anisotropic Curved Beam Model

The governing equations of a waveguide may be derived based on a set of assumptions on the distribution of the displacement field. In Chapter 2, a model was presented based on the expansion of the displacement field up to third-order terms about the mid-plane, and the accuracy of first-order models was discussed. The first-order model derived from the first-order shear deformation theory (FSDT) may capture the fundamental antisymmetric guided waves with a reasonable accuracy. Accurate estimation of the fundamental symmetric mode at high frequencies however, depends on if and how the contraction terms are accounted for in the model. The contraction can occur in different directions, i.e. thickness-wise and width-wise directions. It seems that the models presented so-far in the literature [Mitra and Gopalakrishnan, 2006c, Gopalakrishnan et al., 2008, Mahapatra and Gopalakrishnan, 2004, Nag et al., 2003, Palacz et al., 2005b, Pahlavan et al., 2010], have neglected the presence of the in-plane and the out-of-plane contraction effects at the same time. To improve on these models and alleviate the short-comings arising from the neglected contraction term(s), a model describing the wave motion in a curved anisotropic 1D waveguide in the presence of the axial-flexural-shear coupling is implemented in this section.

4.1.1 Equations of Motion

Consider a finite curved beam element with constant radius R, thickness h, and width b, as shown in Figure 4.1. By neglecting the mid-plane $r-\theta$ motion in the $z-$direction, the assumed displacement field in the cylindrical coordinate system can be expanded in a Taylor series about the mid-plane, i.e. $r = R$:

$$\mathbf{d} = \begin{pmatrix} u_\theta(s,r,t) \\ u_z(s,z,t) \\ u_r(s,r,t) \end{pmatrix} = \begin{pmatrix} u(s,t) + (r-R)\,\phi(s,t) \\ z\chi(s,t) \\ w(s,t) + (r-R)\,\psi(s,t) \end{pmatrix} \tag{4.1}$$

where $s = r\theta$ is the hoop coordinate, ϕ denotes the rotation of the cross-section in accordance with the FSDT, ψ and χ are respectively the contraction terms along the r and z coordinates, u is the circumferential displacement, and w denotes the radial displacement of the mid-plane. With the choice of proper correction factors, it is known that the FSDT is sufficiently accurate for describing the fundamental antisymmetric wave mode [Wang and Achenbach, 1994]. It will also be shown later in this section that the contraction terms may play a significant role in capturing the fundamental symmetric Lamb wave mode. The engineering strain-displacement relations in the cylindrical coordinate system are formulated as:

$$\boldsymbol{\epsilon} = \begin{pmatrix} \varepsilon_{\theta\theta} \\ \varepsilon_{zz} \\ \varepsilon_{rr} \\ \gamma_{rz} \\ \gamma_{r\theta} \\ \gamma_{z\theta} \end{pmatrix} = \begin{pmatrix} \frac{\partial u_\theta}{\partial s} + \frac{u_r}{r} \\ \frac{\partial u_z}{\partial z} \\ \frac{\partial u_r}{\partial r} \\ \frac{\partial u_z}{\partial r} + \frac{\partial u_r}{\partial z} \\ \frac{\partial u_r}{\partial s} + \frac{\partial u_\theta}{\partial r} + \frac{u_\theta}{r} \\ \frac{\partial u_z}{\partial s} + \frac{\partial u_\theta}{\partial z} \end{pmatrix}. \tag{4.2}$$

For convenience in notation, the dependent variables are assembled in the vector $\mathbf{u}$:

$$\mathbf{u} = (u, \psi, w, \phi, \chi)^T. \tag{4.3}$$

From the stain field shown and the displacement field in Equation (4.1), the only zero stain is γ_{rz}, and the rest of the strain components contribute in the motion. It should be added that in order to facilitate further computations regarding the last term in $\gamma_{r\theta}$, the radius of the curved beam is assumed to be fairly large compared to the laminate thickness.

In order to obtain the governing equations for a composite beam, Hamilton's principle is employed [Reddy, 2005]. For a linear elastic material occupying the spatial domain Ω, the strain energy is given by:

$$U = \frac{1}{2}\int_\Omega \boldsymbol{\epsilon}^T \mathbf{C} \boldsymbol{\epsilon} dv, \tag{4.4}$$

where dv denotes the volume element. The 6×6 matrix $\mathbf{C}$ contains the stiffness muduli of each lamina of a multilayered composite material:

$$\mathbf{C} = \begin{pmatrix} C_{11} & C_{21} & C_{31} & 0 & 0 & C_{61} \\ C_{21} & C_{22} & C_{32} & 0 & 0 & C_{62} \\ C_{31} & C_{32} & C_{33} & 0 & 0 & C_{63} \\ 0 & 0 & 0 & C_{44} & C_{54} & 0 \\ 0 & 0 & 0 & C_{54} & C_{55} & 0 \\ C_{61} & C_{62} & C_{63} & 0 & 0 & C_{66} \end{pmatrix}. \tag{4.5}$$

The kinetic energy of the body with the material density ρ is defined as:

$$T = \frac{1}{2}\int_\Omega \dot{\mathbf{d}}^T \rho\, \dot{\mathbf{d}} dv, \tag{4.6}$$

where the displacement vector was given in Equation (4.1). The Lagrangian can be subsequently introduced as:

$$\mathcal{L} = T - (U + V), \tag{4.7}$$

where V is the potential function of the applied external forces. Deriving the Lagrangian in terms the dependent variables u, ψ, w, ϕ, and χ introduced in equation(4.1), and taking the variation with respect to each, five coupled partial differential equations are obtained as follows:

$$\begin{aligned}\delta u: \; & KA_{55}\frac{\partial w}{\partial s} + KA_{55}\phi - K^2B_{55}\phi + KB_{55}\frac{\partial \psi}{\partial s} - K^2A_{55}u + A_{21}\frac{\partial \chi}{\partial s} \\ & + A_{31}\frac{\partial \psi}{\partial s} + KA_{11}\frac{\partial w}{\partial s} + KB_{11}\frac{\partial \psi}{\partial s} + B_{11}\frac{\partial^2 \phi}{\partial s^2} + A_{11}\frac{\partial^2 u}{\partial s^2} \\ & = I_0^z\frac{\partial^2 u}{\partial t^2} + I_1^r\frac{\partial^2 \phi}{\partial t^2}\end{aligned} \tag{4.8}$$

$$\begin{aligned}\delta\psi: \; & -\chi A_{32} - A_{31}\frac{\partial u}{\partial s} - KA_{31}w - K^2B_{11}w - KB_{11}\frac{\partial u}{\partial s} \\ & - KB_{21}\chi - KD_{11}\frac{\partial \phi}{\partial s} - B_{31}\frac{\partial \phi}{\partial s} - \psi A_{33} - K^2D_{11}\psi - 2\,KB_{31}\psi \\ & + D_{55}\frac{\partial^2 \psi}{\partial s^2} - KB_{55}\frac{\partial u}{\partial s} - KD_{55}\frac{\partial \phi}{\partial s} + B_{55}\frac{\partial^2 w}{\partial s^2} + B_{55}\frac{\partial \phi}{\partial s} \\ & = I_2^r\frac{\partial^2 \psi}{\partial t^2} + I_1^r\frac{\partial^2 w}{\partial t^2}\end{aligned} \tag{4.9}$$

$$\begin{aligned}\delta w: \; & -KA_{11}\frac{\partial u}{\partial s} - KA_{21}\chi - KA_{31}\psi - K^2B_{11}\psi - KB_{11}\frac{\partial \phi}{\partial s} \\ & - K^2A_{11}w + A_{55}\frac{\partial \phi}{\partial s} - KA_{55}\frac{\partial u}{\partial s} - KB_{55}\frac{\partial \phi}{\partial s} + B_{55}\frac{\partial^2 \psi}{\partial s^2} \\ & + A_{55}\frac{\partial^2 w}{\partial s^2} = I_0^z\frac{\partial^2 w}{\partial t^2} + I_1^r\frac{\partial^2 \psi}{\partial t^2}\end{aligned} \tag{4.10}$$

$$\begin{aligned}\delta\phi: \; & KA_{55}u - A_{55}\frac{\partial w}{\partial s} - K^2B_{55}u + KB_{55}\frac{\partial w}{\partial s} + KD_{55}\frac{\partial \psi}{\partial s} \\ & - B_{55}\frac{\partial \psi}{\partial s} - A_{55}\phi - K^2D_{55}\phi + 2\,KB_{55}\phi D_{11}\frac{\partial^2 \phi}{\partial s^2} + KB_{11}\frac{\partial w}{\partial s} \\ & + KD_{11}\frac{\partial \psi}{\partial s} + B_{11}\frac{\partial^2 u}{\partial s^2} + B_{21}\frac{\partial \chi}{\partial s} + B_{31}\frac{\partial \psi}{\partial s} = I_2^r\frac{\partial^2 \phi}{\partial t^2} + I_1^r\frac{\partial^2 u}{\partial t^2}\end{aligned} \tag{4.11}$$

$$\begin{aligned}\delta\chi: \; & -A_{32}\psi - A_{21}\frac{\partial u}{\partial s} - KA_{21}w - KB_{21}\psi - B_{21}\frac{\partial \phi}{\partial s} - A_{22}\chi \\ & + J_2^z\frac{\partial^2 \chi}{\partial s^2}A_{66} = I_2^z\frac{\partial^2 \chi}{\partial t^2}\end{aligned} \tag{4.12}$$

where the curvature K (the reciprocal of R) is used for the sake of simplicity in notation. Furthermore, the laminate stiffness and inertia coefficients are given

by:

$$\begin{pmatrix} A_{ij} & B_{ij} & D_{ij} \\ I_0^r & I_1^r & I_2^r \end{pmatrix} = \sum_{n=1}^{N_l} \int_{r_i-R}^{r_{i+1}-R} \begin{pmatrix} C_{ij}^n \\ \rho \end{pmatrix} \left[1, r, r^2\right] b \, dy, \tag{4.13}$$

with C_{ij}^n denoting the (i,j)th component of the material stiffness matrix. In addition,

$$I_2^z = \frac{1}{b} \sum_{n=1}^{N_l} \int_{-\frac{b}{2}}^{\frac{b}{2}} z^2 dz. \tag{4.14}$$

Equations (4.8) to (4.12) express the wave motion in a 1D curved waveguide with axial-flexural-shear coupling. The boundary conditions required to solve these equations can be obtained by taking the variation of the Lagrangian with respect to the first derivative of each dependent variable [Reddy, 1997], which leads to

$$F_\theta(s,t) = -A_{31}\psi - A_{21}\chi - A_{11}\frac{\partial u}{\partial s} - KB_{11}\psi - KA_{11}w - B_{11}\frac{\partial \phi}{\partial s} \tag{4.15}$$

$$M_{rr}(s,t) = -D_{55}\frac{\partial \psi}{\partial s} + KB_{55}u + KD_{55}\phi - B_{55}\frac{\partial w}{\partial s} - B_{55}\phi \tag{4.16}$$

$$F_{r\theta}(s,t) = -A_{55}\phi - A_{55}\frac{\partial w}{\partial s} + KB_{55}\phi + KA_{55}u - B_{55}\frac{\partial \psi}{\partial s} \tag{4.17}$$

$$M_z(s,t) = -D_{11}\frac{\partial \phi}{\partial s} - KB_{11}w - KD_{11}\psi - B_{11}\frac{\partial u}{\partial s} - B_{21}\chi - B_{31}\psi \tag{4.18}$$

$$M_{zz}(s,t) = -J_2^z \, A_{66}\frac{\partial \chi}{\partial s}. \tag{4.19}$$

Note that if the radius is very large, the terms multiplied by the curvature K vanish and the governing equations will reduce to those for a straight beam. If the contraction in z-direction is neglected as well, the governing equations will become identical to those obtained by Gopalakrishnan et al. [2008]. Further in this section, the importance of the contraction terms will be highlighted.

4.2 Spectrum and Dispersion Relations

In order to study the propagation characteristics and the dispersion properties of the described waveguide, a harmonic response is assumed in accordance with

$$\mathbf{u}(s,t) = \hat{\mathbf{u}} e^{i(ks-\omega t)} \tag{4.20}$$

where k is the wavenumber, ω is the angular frequency, and $\hat{\mathbf{u}}$ denotes the corresponding amplitudes of $\mathbf{u}$. Substitution of the harmonic solution with the prescribed frequency ω into equations (4.8) to (4.12) can be written in the following matrix-vector form,

$$\mathbf{W}(k)\hat{\mathbf{u}} = \mathbf{0}. \tag{4.21}$$

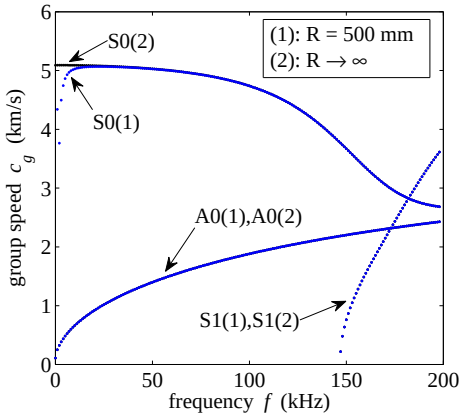

Figure 4.2: Group speed dispersion curves for the aluminium beams with $R = 500$ mm and $R \to \infty$.

In order to find the non-trivial solution, the determinant of $\mathbf{W}(k)$ should be equated to zero. For the problem under investigation, this leads to a standard polynomial eigenvalue problem (PEP) of order 2 with respect to the wavenumber, with five variables $(\hat{u}, \hat{\psi}, \hat{w}, \hat{\phi}, \hat{\chi})$. Solution techniques for PEPs have been discussed in detail by Gopalakrishnan et al. [2008].

The current model may be viewed as an application of the Timoshenko beam theory in the $r-\theta$ plane, and the Mindlin-Hermann rod theory [Doyle, 1989] in the $r-\theta$ and $\theta-z$ planes. In order to study the influence of different deformation modes assumed, the present model is reduced to some special cases. In the comparative study, the material is considered to be aluminum. Examples of composite beams however, are also provided later in this section. The thickness h and the width b of the waveguide are 1 mm and 20 mm, respectively.

For the first case, the beam curvature is considered to be negligible, i.e. $K \to 0$. This simplifies the equations to a straight waveguide. The group speed dispersion curves for this case are illustrated in Figure 4.2. Within the frequency range of [0,200] kHz, two symmetric, i.e. S0 and S1, and one antisymmetric, i.e. A0, wave modes propagate. It can be observed that the influence of the curvature is pronounced only at the low frequency regime. Beyond a certain frequency, which is about 25 kHz in this example, wave propagation is characterized *only* by the cross-section and material properties and not the curvature, i.e. wave propagation beyond 25 kHz is a localized phenomenon. At lower frequencies however, the coupling effect due to the curvature is significant and cannot be neglected, in other words, the global response becomes more dominant.

In the second case, the assumption of negligible contraction in the z-direction ($\chi = 0$) is imposed to the straight beam. This simplifies the model to that derived by Mahapatra and Gopalakrishnan [2003] for describing axial-flexural-

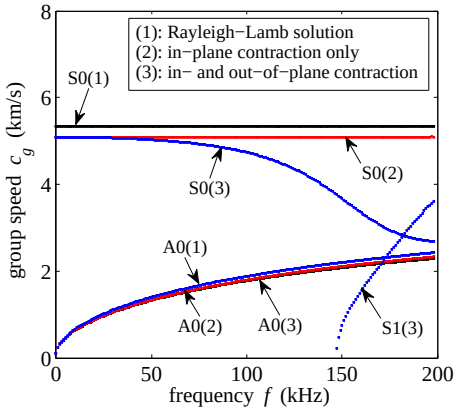

Figure 4.3: Influence of the contraction term on the group speed dispersion curves for an aluminum beam ($b = 20$ mm).

shear coupling in laminated composite beams. The group speed curves for this case are shown in Figure 4.3, and compared to the Rayleigh-Lamb solution.

The Rayleigh-Lamb solution for plate structures, as discussed in Chapter 2, is based on the plane-strain assumption in the $r - \theta$ plane, whereas the model presented by Mahapatra and Gopalakrishnan [2003] assumes plane-stress conditions. For a quadruply-bounded waveguide, these models may result in inaccuracies in the dispersion relations as shown in Figure 4.3: the Rayleigh-Lamb solution overestimates the propagation speed of the symmetric waves, since it does not consider the finite width of the waveguide. Although the model assuming plane-stress conditions is in agreement with the present model up to a certain frequency (50 kHz in this example i.e. $f.h = 1000$ kHz mm), it diverges sharply after this frequency and does not capture any cut-off frequency for the next antisymmetric mode A1(3). It should be noted that the present model is also limited to a certain frequency range, below the cut-off frequency of S1. The validity range of this first-order model may also be estimated from Figure 2.2 in which a first-order model was compared to a third-order model. The limit frequency according of this model, which is in accordance with the Mindlin-Hermann theory for S0 waves [Doyle, 1989], is much higher than the model that neglects the contraction in the $\theta - z$ plane, see Figure 4.4. The accuracy of the present model will be validated in Section 4.3 by comparing to a 3D time-domain spectral element method (SEM).

The influence of the beam width on the group speed dispersion curves is illustrated next in Figure 4.4. For a beam with a reduced width $b = 5$ mm, it can be observed that including and excluding the thickness contraction in the z-direction result in nearly the same response up to 200 kHz which is equivalent to $f.b = 1000$ kHz mm. The difference between the two models however, was significant in Figure 4.3 for $b = 20$ mm. The main conclusion drawn from

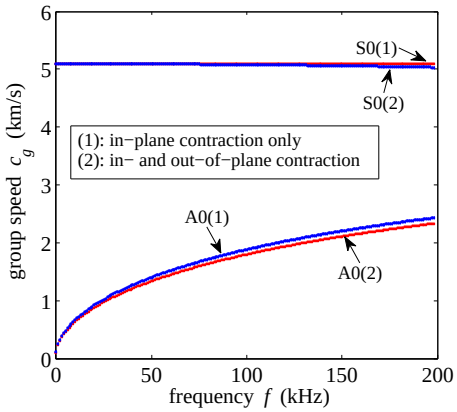

Figure 4.4: Influence of the contraction term on the group speed dispersion curves for an aluminum beam ($b = 5$ mm).

this study is that the importance of including the thickness contraction in the thickness-wise and the width-wise directions in the beam model is highly dependent on the geometry of the waveguide. The product of the frequency and the width and/or thickness needs to be carefully considered before using an approximate solution.

Although not presented here, other special cases can still be extracted from the present model. For instance, excluding the thickness contraction in r-direction as well ($\psi = 0$), represents the classical FSDT; or the elementary beam theory can be successively examined by addition of the conditions $I_1^r = I_2^r = 0$ and $C_{33}^n, C_{55}^n \to \infty$ to the previous conditions. From the results demonstrated by Gopalakrishnan et al. [2008], the inaccuracy of such elementary theories at high frequencies was concluded, thus they can not be applicable in SHM.

As a concluding remark, in dynamics, in contrast to static analysis of structures, the product of the thickness and frequency determines what assumptions can be made for the distribution of the displacement fields. The maximum frequency which can be captured accurately in a waveguide with rectangular cross-section is determined by the largest dimension of the cross-section of the waveguide. When the width of a waveguide is an order of magnitude larger than the thickness, the contraction effect may be neglected in the thickness-wise direction, and vice versa. It should also be noted that at frequencies which are sufficiently high to trigger higher order Lamb wave modes, i.e. beyond the first cut-off frequency, the assumed displacement fields should be enriched with higher-order functions, or 2D/3D models should be used, in order to obtain a more accurate solution.

4.3 Wavelet-based Spectral Finite Element Implementation of the Problem

The spectral finite element formulation is based on the decoupled wavelet-Galerkin method (DWG) explained in detail in Chapter 3, through which equations (4.8) to (4.12) can be represented in a temporally-decoupled fashion. The displacement field at the jth wavelet point $\bar{\mathbf{u}}_j$ can be expressed as follows

$$\bar{\mathbf{u}}_j = \bar{\mathfrak{u}}_j e^{ik_j s} \tag{4.22}$$

where $\bar{\mathfrak{u}}_j$ denotes the amplitude envelope of the wave, and k_j is the wavenumber at the jth wavelet point. The governing equations at the jth wavelet point can hence, be shown in matrix notation as

$$\left(\mathbf{A_2}k^2 + \mathbf{A_1}k + \mathbf{A_0}\right)\bar{\mathfrak{u}}_j e^{ik_j s} = 0 \tag{4.23}$$

where the coefficient matrices $\mathbf{A_1}, \mathbf{A_2}$, and $\mathbf{A_3}$ can be readily derived from equations (4.8) to (4.12). Equation (4.23) is in fact a PEP, analogous to the dispersion analysis, with $5 \times 2 = 10$ eigenvalues, where 5 is the number of dependent variables, see Equation (4.3), and 2 is the PEP order. In order to obtain a non-trivial solution, the wavenumbers k setting the determinant to zero are sought. The system response to any input can be constructed as a linear combination of the resulting 10 eigenfunctions as

$$\bar{\mathfrak{u}}_j = \sum_{n=1}^{10} c_{j,n}\mathfrak{A}_{j,n}e^{ik_{j,n}s} \tag{4.24}$$

where the weights $c_{j,n}$ need to be determined in accordance with the boundary conditions. The nth component of the eigenvector denoted by $\mathfrak{A}_{j,n}$, and the nth wavenumber $k_{j,n}$, correspond to the nth eigenfunctions at the jth wavelet point. Equation (4.24) can be represented in matrix notation as

$$\bar{\mathfrak{u}}_j = \mathbf{Q}_j\mathbf{c}_j \,;\, \mathbf{Q}_j[m,n] = \mathfrak{A}^m_{j,n}e^{ik_{j,n}s} \tag{4.25}$$

with the weight coefficients $c_{j,n}$ being put in vector $\mathbf{c}_j$. Also $\mathbf{Q}_j[m,n]$ denotes the component at the mth row and the nth column of the matrix $\mathbf{Q}_j$. If the obtained eigenfunctions form a basis to express the displacement fields, the resulting formulation will present an exact solution, provided that no discontinuity exists in the physical domain $\Omega_e \subseteq \mathbb{R}$. If formulated as a finite element method to construct a dynamic stiffness matrix, the implementation would not be an error minimization scheme as the error, i.e. the residual of the homogenous governing equation, is naturally zero; but is only a way to conveniently model the generally-inhomogeneous domain Ω with N_{el} non-overlapping homogeneous subdomains Ω_e, i.e.

$$\Omega = \bigcup_{e=1}^{N_{el}} \Omega_e \tag{4.26}$$

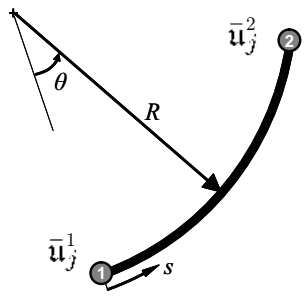

Figure 4.5: The curved two-noded beam element.

and readily incorporate the boundary conditions.

A two noded curved beam element is considered here as shown in Figure 4.5. The element nodal displacements $\bar{\mathbf{q}}_j$ can be written in terms of the weight coefficients and a projection matrix denoted by $\mathbf{T}_j$:

$$\bar{\mathbf{q}}_j = \mathbf{T}_j \mathbf{c}_j \, ; \mathbf{T}_j[m,n] = \mathfrak{A}_{j,n}^m e^{ik_{j,n}\bar{s}(n)} \tag{4.27}$$

where

$$\bar{s}\,(n) = \begin{cases} 0 & \text{for } 1 \leq n \leq 5 \\ l^e & \text{for } 6 \leq n \leq 10. \end{cases} \tag{4.28}$$

The spectral interpolation functions relating the displacement fields to the nodal displacements at the jth wavelet point can be consequently constructed as follows:

$$\bar{\mathfrak{u}}_j = \mathbf{Q}_j \mathbf{T}_j^{-1} \bar{\mathbf{q}}_j = \mathbf{N}_j \bar{\mathbf{q}}_j, \tag{4.29}$$

where $\mathbf{N}_j$ is the matrix of basis, i.e. shape, functions at the jth wavelet point. The procedure is hereafter completely analogous to FEM. The finite element basis which already includes the dynamic properties of the structure can be utilized to compute the dynamic stiffness matrix $\mathbf{K}_j^{dyn}$ as

$$\mathbf{K}_j^{dyn} = \bigcup_{e=1}^{N_{el}} \left(\mathbf{K}_j^e + \bar{\omega}_j \mathbf{C}_j^e + \bar{\omega}_j^2 \mathbf{M}_j^e \right) \tag{4.30}$$

where $\bar{\omega}_j$ is the jth wavelet frequency, and $\mathbf{K}_j^e$, $\mathbf{C}_j^e$, and $\mathbf{M}_j^e$ are respectively the stiffness, the damping, and the mass matrices at the element level for the jth wavelet point as given by

$$\mathbf{K}_j^e = \int_{\Omega_e} \mathfrak{B}_j^T \mathbf{C} \mathfrak{B}_j d\Omega \tag{4.31}$$

$$\mathbf{C}_j^e = \int_{\Omega_e} \mathbf{N}_j^T \eta_j \mathbf{N}_j d\Omega \tag{4.32}$$

$$\mathbf{M}_j^e = \int_{\Omega_e} \mathbf{N}_j^T \rho \mathbf{N}_j d\Omega \tag{4.33}$$

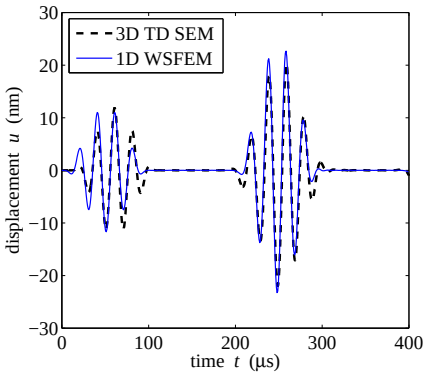

Figure 4.6: Comparison of the present 1D model with 3D time-domain SEM at 50 kHz. The second envelop arriving at about $200\mu s$ is the reflection of S0 waves from the beam end.

where the strain-nodal displacement matrix $\mathfrak{B}_j = \mathbf{L}\mathbf{N}_j$ with $\mathbf{L}$ being the displacement-strain continuous operator matrix, and η_j is the frequency-dependent damping coefficient. As mentioned earlier, since the finite element formulation satisfies the equations of motion exactly, as long as there is no discontinuity and inhomogeneity in the system, a single element is sufficient to capture the displacement at the jth wavelet point exactly.

The present model is compared to a 3D time-domain (TD) spectral element method (SEM) for a free-free straight aluminum beam with $l = 500$ mm, $h = 1$ mm, and $b = 20$ mm, whose group speed curves were given in Figure 4.3. The simulation time is 400 μs discretized at 13333 sample points in the TD solution and 400 points in the WSFEM. The SEM model has 4545 degrees of freedom (DOFs) based on the mesh pattern $20 \times 1 \times 2$ in the length-, thickness-, and width-wise directions, and the corresponding basis order of 5, 2, and 2, whereas the WSFEM uses 1 element with 10 DOFs, as explained above. The external load is a 5-cycle narrow-banded Hanning-windowed pulse with central frequency f_0, applied at one end of the beam. The displacement response at the same point, excitation point, is illustrated in figures 4.6 and 4.7 for $f_0 = 50$ kHz and $f_0 = 100$ kHz, respectively.

A very good agreement between the two methods at 50 kHz can be observed in Figure 4.6. At 100 kHz however, despite the good match between the arrival times at about 200 μs, a mismatch due to different dispersion characteristics can be seen that, depending on the application, may or may not be significant. This is in fact, the price that one may afford for such a computationally-inexpensive method, which saves drastically in the computational power and time. In damage identification schemes which are based on the time of flight (TOF) of the ultrasonic wave packets and transmission/reflection coefficients, the 1D WSFEM can provide the sufficient accuracy. Similar to the Fourier-based spectral FEM [Gopalakrishnan et al., 2008], adoption of correction factors can enhance

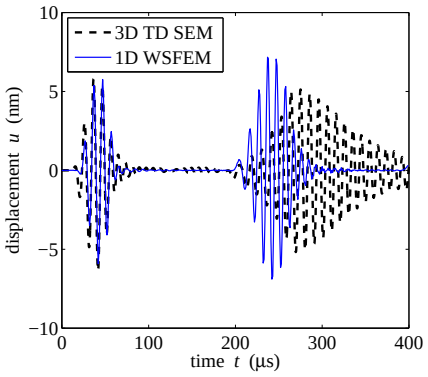

Figure 4.7: Comparison of the present 1D model with 3D time-domain SEM at 100 kHz. The second envelop arriving at about $200\mu s$ is the reflection of S0 waves from the beam end.

the accuracy of the 1D formulation for practical applications. For estimation of the accuracy of the method in the absence of a reference solution, comparison of the frequency-thickness product of the structure with that of the cut-off frequency of higher-order modes is generally required.

4.4 Extended Applications of the Implemented Model

The implemented finite element framework in this chapter is a computationally-efficient model for the waveguides which limit the waves to propagate in a single direction. From this model, a number of special cases were extracted in previous sections. In this section, some extended applications derived from the presented model are outlined.

4.4.1 Composite Rings

Although the application of composite rings and frames is growing intensively in aerospace industry, it seems that to date, not enough attention is paid to the numerical models of wave propagation in such structural members. With the implemented curved element, modeling ring-type composite structures is straight-forward. The ring-type structure which can be circular or oval, can be made by assembling the appropriately constructed elements, and a subsequent imposition of periodic boundary condition equalizing the displacements of the end points.

4.4.2 Frame Structures

Frames structures composed of straight and/or curved members can be modeled using the implemented WSFEM. Similar to the standard FEM, transformation of the coordinate system is required to model the rotated members in the global coordinate system.

4.4.3 Delamination Modeling in Composite Beams

Delamination in composites is the most challenging type of damage from an inspection point of view, as discussed in Chapter 1. In a typical SHM application, the travel time of a diagnostic wave packet through a delamination of order if a few centimeter is of the order of a few microseconds, and the displacement of the waveguide is orders of magnitude smaller than the laminate thickness. The complexity of interaction of the diagnostic waves with the damaged area exhibiting nonlinearities may be hence approximated by simplified models, without substantial loss of information, especially about the location of the defect. In other words, under such conditions, avoiding computationally-expensive and sophisticated nonlinear damage mechanics models and instead, using reduced-order models to approximate the behavior of the delaminated waveguide at ultrasonic frequencies can be justified.

To date, it seems that the use of these methods in health monitoring of delaminated ring-type composite structures has not been addressed in the literature. Some computationally-efficient models for delaminated straight beams have been suggested by Mahapatra and Gopalakrishnan [2004], Mitra and Gopalakrishnan [2006c], Nag et al. [2003]. In the present research, the approach used in the abovementioned references is modified and extended to the implemented curved beam model; the delaminated region is considered as two split sections (2 and 3) shown in Figure 4.8, each being a free-free-free-free quadruply-bounded waveguide. Each of these sub-structures represents a radial-tangential coupling due to curvature, and asymmetry due to the generally-unbalanced layup at each subsection.

In the conventional approach for straight beams [Mahapatra and Gopalakrishnan, 2004, Mitra and Gopalakrishnan, 2006c, Nag et al., 2003], compatibility conditions are established to couple the delaminated segment and the neighboring elements and subsequently, a 2-noded delaminated element is obtained. These conditions are primarily used in order to match the displacements and equilibrate the forces at the intersections. In this dissertation, a dynamic equivalent of that approach is employed, which facilitates extension of the delamination model to the present enriched curved waveguide model. The term equivalent implies that instead of the additional constraint equations, the compatibility conditions for the displacements, rotations, forces and moments are applied through the standard assembling process of the finite element formulation. The approach uses two elements of thickness h at the delaminated region, where h is the total intact laminate thickness. Each of the two elements however, contains a number of layers with zero stiffness and mass. This way, a

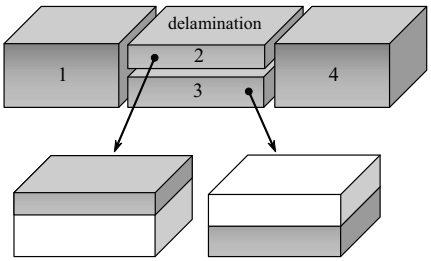

Figure 4.8: The delamination model in a composite beam.

coupling is introduced in the delaminated section, as a result of the asymmetry of each sub-section laminate. The schematic view of the model for a straight member is illustrated in Figure 4.8. Note that this system can be attached to undamaged curved beam elements in a straight-forward manner, following the standard procedure in the FEM [Reddy, 2005].

4.5 Numerical Examples

For the sake of numerical verification, a straight composite beam ($R \to \infty$) mm with thickness $h = 1$ mm, width $b = 20$ mm, and length=500 mm is considered. The material chosen is AS/3501-6 graphite-epoxy with the properties given in Section 2.2.3. The ply-stacking sequence is $[0]_8$ where the 0° fibers are aligned in the longitudinal direction. The structure has free-free boundary conditions. The external load which is a 5-cycle narrow-banded Hanning-windowed pulse with central frequency of 100 kHz, is applied at the left end in the longitudinal direction. The assumed delamination is 10 mm long and is located at the center of the beam (right end at $x = 250$ mm) between the third and the fourth material layers. The order of the compactly-supported wavelets for the temporal approximation is $N = 6$, and the 200 μs time window is discretized at $L = 250$ sample points. Four elements are sufficient in modeling the beam; two elements for the two intact segments at the left- and right-hand-sides of the delamination, and two elements for modeling the delaminated segment as explained in Section 4.4.3.

The displacement response of the structure at the excitation point is shown in Figure 4.9. The baseline response, which is the response of the undamaged structure, is plotted in the same figure. Also a contour plot illuminating the displacement response of the beam as a function of time and location can be observed in Figure 4.10. The difference between the baseline response and the response of the delaminated beam can be seen in Figure 4.9. The additional wave packet in the response of the delaminated beam starting at nearly 60μs (the dashed line) in this figure, is due to the reflection of the incoming waves by the delamination. This can also be seen in Figure 4.10, where a secondary branch separates from the main branch due to the interaction of the waves with

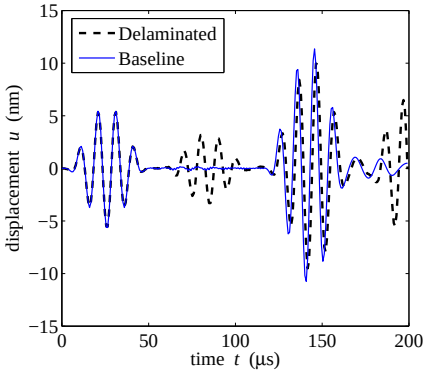

Figure 4.9: The displacement response of the delaminated ring at the excitation point.

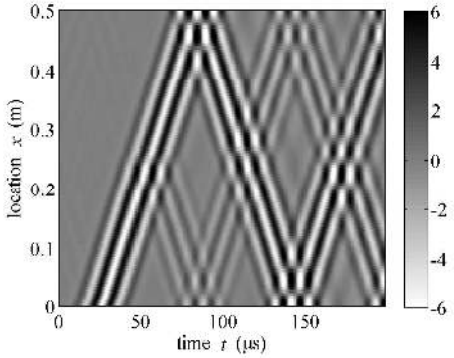

Figure 4.10: The displacement response of the delaminated composite beam.

delamination at about $t = 60$ μs and $x = 250$ mm. The reflections by the beam ends at $x = 0$ and $x = 0.5$ m can also be observed.

In the next example, a composite ring with radius $R = 500$ mm is considered. The material, stacking sequence, height, and width of the beam are the same as in the previous example. As shown in Figure 4.11, the structure is not clamped, i.e. no displacement boundary condition. The external load signal is also the same as in the previous example, and is applied at point A in the circumferential direction. A 10 mm long delamination between the third and the fourth layers of the laminate, is located at zone D, 270° from point A. The time window chosen is 560 μs which is discretized at $L = 560$ sample points.

The displacement response of the ring at point A is shown in Figure 4.12. When the diagnostic waves are generated by applying the external excitation, the delamination reflects a part of the incoming waves. These reflections arrive

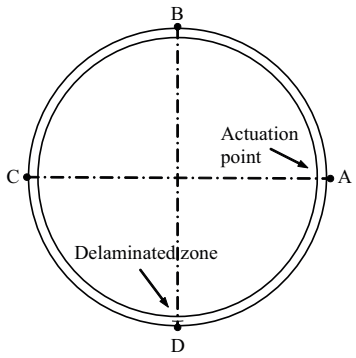

Figure 4.11: The model of the delaminated ring. The delamination is located at point D.

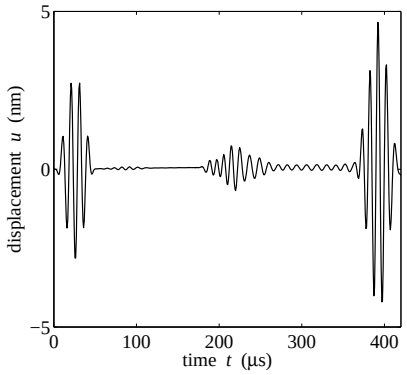

Figure 4.12: The displacement response of the delaminated ring at point A.

at the measurement point A, at about 200 μs. One can determine the location of the delamination by extracting the group speed of the S0 waves at 100 kHz, and the time of flight of the reflected packet. This will be discussed in Chapter 7, and more advanced approaches will be presented for autonomous identification of delamination in composite structures.

A contour of the displacement response of the composite ring in the circumferential direction is plotted in Figure 4.13. Although it may not be very clear at the first glance, about the time 120 μs and the angular location 270°, a secondary branch orthogonal to the top main branch appears, which shows the waves bouncing off the delamination. It can also be observed that the amplitude of the wave packet decreases slightly as it passes through the delamination, since it loses a part of its energy through the reflected waves.

The deformations of the beam at six different times scaled up by 6×10^7, are illustrated in Figure 4.14. Once the diagnostic waves are sent to the structure,

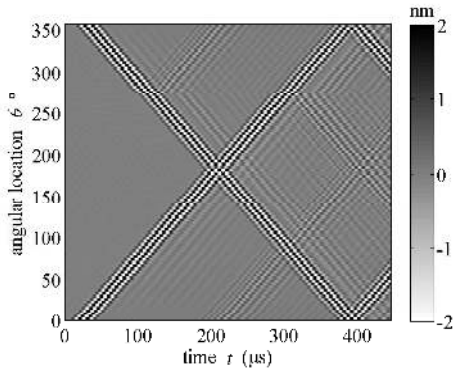

Figure 4.13: The displacement response of the delaminated composite ring.

they travel through both the upper and the lower segments of the ring. The propagation at this frequency is a highly localized phenomenon. Thus, before reaching the delamination, the displacement field is symmetric with respect to the trajectory dividing the ring into the upper half and the lower half. At 149.6 μs, the reflection from the delamination appears. At 224 μs, the reflected packet is passing through point A, which can be seen in Figure 4.14 and also at the coordinate (224,365) in Figure 4.13. After interacting with the other wave packets, it is more difficult to extract information from the response.

It is worthwhile to drop the point that in this particular example, if the delamination was located at 180° from point A, no reflection would be seen as the transmitted and reflected signals on each side would add up to the original incoming waves.

4.6 Advantages and Limitations of The Proposed 1D Model

A computationally-efficient model was presented in this chapter which can capture propagation of the fundamental modes of guided waves in composite beams. The accuracy of the model depends on the geometry of the structure and the frequency content of the diagnostic waves. Using the present model, the dispersion curves of the waveguide are extracted from which the accuracy of the model can be estimated. This model will be used in Chapter 8 in a model-based SHM system, for delamination identification in composite beams and rings. For the cases where the present model can not be adopted e.g. very thick beams, 2D and 3D models as explained in the next chapters may be used.

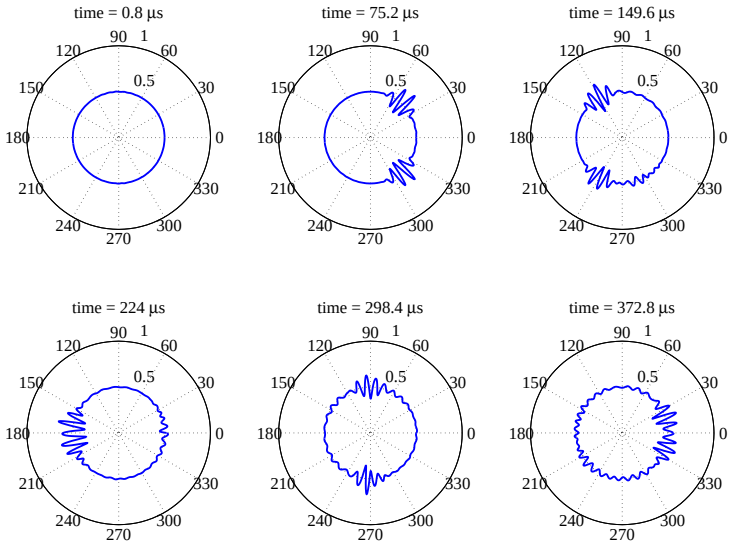

Figure 4.14: Propagation of S0 waves in the delaminated composite ring (displacement scaling $= 6 \times 10^7$).

Chapter 5

Wavelet-Based Spectral Finite Element for 2D Waveguides

The wavelet-based spectral finite element method (WSFEM) was formulated for 1D waveguides in Chapter 4. This Chapter is devoted to extending the WSFEM to 2D waveguides, in particular to plate structures undergoing in-plane displacements[1].

The formulation of the 1D WSFEM, as outlined in Chapter 4, is based on the wavelet-Galerkin approach (see Chapter 3) for temporal discretization of the governing partial differential equations (PDEs) in 1D waveguides. The interpolation functions in the WSFEM for the spatial discretization were chosen to be the eigen-functions of the free-space solution of the homogeneous wave equations. Accordingly and below the cut-off frequency of the higher-order modes, the constructed finite elements were, irrespective of the length of the 1D continuous (sub)structure, able to accurately capture the wave motion with a single element. The number of degrees of freedom (DOFs) in the discretized problem is order(s) of magnitude lower in the WSFEM than in the conventional polynomial-based FEM equipped with Newmark schemes for time integration. Although the wavelet-based spectral formulation obtained in Mitra and Gopalakrishnan [2005], which has been further improved in chapters 3 and 4 of the present dissertation, is inherently advantageous for simulation of wave propagation in 1D waveguides, engineering applications often require more complex and higher-dimensional models. In order to develop a spectrally-formulated finite element framework to solve 2D wave equations, Mitra and Gopalakrishnan [2006d, 2007] use the wavelet-Galerkin method temporal and spatial discretization of the solution. They apply the Daubechies wavelets as an alternative to

[1]The article "A 2D wavelet-based spectral finite element method for elastic wave propagation", Pahlavan et al. [2012a] in Philosophical Magazine, has been extracted from the content of this chapter.

the fast Fourier transform (FFT) in the FFT-based spectral FEM, see Chapter 2: transforming both the time parameter and one of the spatial coordinates, and subsequently solving the ordinary differential equation in terms of the remaining spatial coordinate with FEM [Mitra and Gopalakrishnan, 2006d, 2007]. Despite the advantages of this approach referred to as the *conventional* WSFEM in this dissertation, in terms of (i) allowing for a decoupling of the governing equations in the transformed domain, which naturally enables parallel computation, and (ii) providing a time discretization scheme that is independent of the spatial discretization, undesirable artificial edge effects in space and time are observed. The elimination of these edge effects requires the application of elaborate extrapolation schemes at the temporal and spatial boundaries of the problem under consideration, as discussed in Chapter 3, see also [Qian and Weiss, 1993, Mitra and Gopalakrishnan, 2006d, 2007, Williams and Amaratunga, 1997]. With respect to a spatial coordinate, such a scheme only works adequately if the geometrical boundary and the corresponding boundary conditions are relatively straightforward.

In the present chapter, a novel wavelet-based spectral finite element method (WSFEM) is proposed that keeps the appealing features of the conventional wavelet-based spectral method, but overcomes its restrictions. The approach, which is elaborated for a two-dimensional orthotropic structure, is based on a temporal transformation of the governing equations to the wavelet domain using a wavelet-Galerkin approach. The resulting equations are decoupled by means of an eigenvalue analysis, and subsequently spatially discretized in the wavelet domain with FEM. A 9-noded element with exponential shape functions is derived for the FEM discretization, where the complex arguments of the shape functions are determined from the characteristics of compression and shear waves propagating along the principal axes of orthotropy[2]. The final solution is obtained by back-transforming the FEM nodal displacements computed in the wavelet domain to the time domain. Since there is no geometrical edge effect when all spatial coordinates are discretized with FEM in the physical spatial domain, the WSFEM formulation is suitable for studying wave propagation phenomena in structures with arbitrary shape and boundary conditions. Furthermore, the temporal edge effects emerging from the DWT of the time parameter can be eliminated for zero initial conditions in a straightforward fashion, as demonstrated in Chapter 3. The governing equations in the transformed domain are uncoupled for each wavelet point, which makes the WSFEM approach suitable for parallel computation.

The accuracy and applicability of the 2D WSFEM approach were demonstrated in the numerical results section, by examining the dispersion relations of a benchmark problem on Lamb, waves in an isotropic, plane-strain layer with traction-free surfaces, and comparing the numerical result to the well-known Rayleigh-Lamb solution [Achenbach, 1993, Doyle, 1989]. In addition, the in-plane propagation of compression and shear waves in a plate subjected

[2]A different implementation of the method based on 8-noded elements can be found in Pahlavan et al. [2011].

to an impact load is simulated, and the result is compared to FEM solutions computed with linear and quadratic elements and a direct numerical time-integration scheme. The effect of anisotropy and irregular material interfaces and boundaries were demonstrated by comparing the WSFEM solutions for an isotropic plate to that of an orthotropic plate, and to that of a plate made of two dissimilar materials, with and without a cut-out at one of the plate corners.

5.1 Description of the 2D Model

The wavelet-Galerkin approach outlined in Chapter 3, is applied to the case of the in-plane dynamic response of an orthotropic layer. Assuming a 2D domain Ω in the $x-y$ plane, with finite thickness in the z-direction, and adopting the plane-stress assumption, the equations of motion in the $x-$ and y-directions of the layer, which are assumed to coincide with the principal axis of orthotropy, can be deduced from the general three-dimensional case presented in [Reddy, 2007] as:

$$Q_{11}\frac{\partial^2 u}{\partial x^2} + (Q_{12}+Q_{66})\frac{\partial^2 v}{\partial x \partial y} + Q_{66}\frac{\partial^2 u}{\partial y^2} = \rho\frac{\partial^2 u}{\partial t^2} \tag{5.1}$$

$$Q_{22}\frac{\partial^2 v}{\partial y^2} + (Q_{21}+Q_{66})\frac{\partial^2 u}{\partial x \partial y} + Q_{66}\frac{\partial^2 v}{\partial x^2} = \rho\frac{\partial^2 v}{\partial t^2} \tag{5.2}$$

where ρ is the material density, $t \in \mathbb{R}^+$ denotes the real time, and $u : \Omega \times t \to \mathbb{R}$ and $v : \Omega \times t \to \mathbb{R}$ are respectively the displacements in x- and y-directions. Also Q_{ij} for $i, j \in \{1, 2, 6\}$ are the in-plane stiffness components where, in accordance with Voigt's notation, the stress and strain tensor components indexed by $11, 22, 12$, correspond to the rows, and columns, $1, 2, 6$ of the stiffness matrix, respectively. Under plane-stress conditions, the non-zero stiffness components have the form:

$$Q_{11} = \frac{E_1}{1-\nu_{12}\nu_{21}},\ Q_{12} = Q_{21} = \nu_{21}Q_{11},\ Q_{22} = \frac{E_2}{1-\nu_{12}\nu_{21}}, Q_{66} = G_{12}. \tag{5.3}$$

From Equation $(5.3)_2$, it follows that symmetry of the stiffness matrix requires that $\nu_{12}E_1 = \nu_{21}E_2$, which essentially leaves the two-dimensional orthotropic model with four independent stiffness parameters, i.e., the axial stiffnesses E_1, E_2, the Poisson's ratio ν_{12}, and the shear modulus G_{12}. Furthermore, since the thickness in the z-direction does not influence the wave propagation in the $x-y$ plane of the layer, this parameter does not appear in equations 5.1 to 5.3.

5.2 The Wavelet-Galerkin Discretization of the 2D Wave Equation

The time discretization of the problem is performed by relating the real time t to dimensionless time τ via:

$$t = \tau \Delta t \ ; \tau \in [0, L-1] \tag{5.4}$$

to correspond with dividing the time window of interest into $L-1$ time intervals Δt. Applying the decoupled wavelet-Galerkin approximation (DWG) presented in sections 3.4 and 3.5 to the equations of motion (5.1) and (5.2), and invoking Equation (5.4), result in:

$$Q_{11}\frac{\partial^2 \bar{u}_j}{\partial x^2} + (Q_{12}+Q_{66})\frac{\partial^2 \bar{v}_j}{\partial x \partial y} + Q_{66}\frac{\partial^2 \bar{u}_j}{\partial y^2} - \rho \bar{\omega}_j^2 \bar{u}_j = 0 \tag{5.5}$$

$$Q_{22}\frac{\partial^2 \bar{v}_j}{\partial y^2} + (Q_{21}+Q_{66})\frac{\partial^2 \bar{u}_j}{\partial x \partial y} + Q_{66}\frac{\partial^2 \bar{v}_j}{\partial x^2} - \rho \bar{\omega}_j^2 \bar{v}_j = 0 \tag{5.6}$$

$$\forall j = 0, 1, ...L-1.$$

In the above equations, $\bar{u}_j : \Omega \to \mathbb{R}$ and $\bar{v}_j : \Omega \to \mathbb{R}$ are the transformed displacements in the wavelet domain, following from the application of the DWG, and $\bar{\omega}_j$ denotes the wavelet frequency defined by Equation (3.46).

As discussed in chapters 3 and 4, decoupling the temporally transformed differential equations enables one to solve them independently at each wavelet point j, thereby allowing for a parallel implementation of the time discretization procedure. The spatial discretization of equations 5.5 and 5.6 is performed using a finite element approach. This makes the present approach different from other wavelet-based solution procedures for 2D problems [Mitra and Gopalakrishnan, 2006d, 2008], where, in addition to a wavelet transformation used for the discretization of the time coordinate, a second wavelet transformation was applied for discretizing one spatial coordinate, and a 1D FEM was subsequently employed to discretize the resulting ordinary differential equations in terms of the other spatial coordinate. As mentioned in the introduction of this chapter, the advantage of discretizing equations 5.5 and 5.6 fully with FEM is that it circumvents the need to meet specific requirements on the type of boundary conditions and the geometry which can be modeled.

5.3 Spatial Discretization of the Transformed 2D Wave Equations

In the present dissertation, specialized basis functions for approximation of the response at each wavelet point are suggested by selection of appropriate functions that closely match the characteristics of the physical problem under consideration. For the study of wave propagation problems in the wavelet domain, it is a natural choice to perform the spatial discretization of Equation (5.5)

by choosing the basis of the displacement fields in accordance with the series expansions:

$$\bar{u}_j(x,y) = \sum_p \sum_q C_{pq}^j \exp\left[i\left(k_x^{j,p}x + k_y^{j,q}y\right)\right] \tag{5.7}$$

$$\bar{v}_j(x,y) = \sum_p \sum_q D_{pq}^j \exp\left[i\left(k_x^{j,p}x + k_y^{j,q}y\right)\right] \tag{5.8}$$

$$\forall j = 0, 1, \cdots, L-1,$$

where C_{pq}^j and D_{pq}^j are the expansion coefficients, and p and q are integers. The constants $k_x^{j,p}$ and $k_y^{j,q}$ can be determined in accordance with the characteristics of specific waves propagating through the structure. In the present study, as will be shown below, these constants which are related to wave-numbers, are derived from the characteristics of the compression (P) and shear (S) waves propagating along the principal axes of orthotropy, i.e., the x- and y-directions.

First, the wave-numbers corresponding to the P and S waves propagating in the x-direction is obtained. The wavelength of such plane waves in the y-direction is infinitely large, which relates to a wave-number equal to zero. This condition is in agreement with:

$$k_y^{j,0} = 0. \tag{5.9}$$

The corresponding wave-numbers in x-direction can be computed by substituting Equation (5.9) into Equation (5.7), followed by inserting the result into Equation (5.5) and calculating the non-trivial solutions. The expression in terms of the displacement $\bar{u}_j$, which is associated with the P waves in x-direction, then provides:

$$k_x^{j,1} = ik_{x,P}^j = i\sqrt{\frac{\rho\bar{\omega}_j^2}{Q_{11}}},\ ; k_x^{j,2} = -ik_{x,P}^j, \tag{5.10}$$

while for the expression in terms of the displacement $\bar{v}_j$, which is associated with the S waves in x-direction, it is found that:

$$k_x^{j,3} = ik_{x,S}^j = i\sqrt{\frac{\rho\bar{\omega}_j^2}{Q_{66}}}\ ; k_x^{j,4} = -ik_{x,S}^j. \tag{5.11}$$

In expressions (5.10) and (5.11), the parameters $k_{x,P}^j$ and $k_{x,S}^j$ have the dimension length^{-1}, and may be interpreted as wave-numbers of the P waves and S waves in x-direction, respectively. These wave-numbers are generally complex-valued, due to the fact that the frequencies $\bar{\omega}_j$ coming from the orthogonal decomposition of the governing equations in the wavelet domain are complex-valued.

The propagation of compression and shear waves in the y-direction corresponds to a wave-number in the x-direction equal to zero, which is in agreement with the condition:

$$k_x^{j,0} = 0. \tag{5.12}$$

Combining Equation (5.12) with Equation (5.7) followed by inserting the result into Equation (5.5), leads to a non-trivial solution for the expression in terms of the displacement $\bar{v}_j$, which is associated with the P waves in y-direction with the wave-number:

$$k_y^{j,1} = ik_{y,P}^j = i\sqrt{\frac{\rho\bar{\omega}_j^2}{Q_{22}}}; k_y^{j,2} = -ik_{y,P}^j, \tag{5.13}$$

In addition, from the expression in terms of the displacement $\bar{u}_j$, which is associated with the S waves in y-direction, it can be derived that:

$$k_y^{j,3} = ik_{y,S}^j = i\sqrt{\frac{\rho\bar{\omega}_j^2}{Q_{66}}}; k_y^{j,4} = -ik_{y,S}^j. \tag{5.14}$$

Note from Equation (5.11) and Equation (5.14) that the wave-numbers $k_{x,S}^j$ and $k_{y,S}^j$, respectively characterizing the propagation of the S waves in x- and y-directions, are equal. Conversely, from equations (5.10) and (5.13), it may be observed that the wave-numbers $k_{x,P}^j$ and $k_{y,P}^j$, characterizing the propagation of the P waves in x- and y-directions, respectively, are different. This difference can be ascribed to the orthotropic material characteristics of the layer. Combining the above result with the general form Equation (5.7), the displacements $\bar{u}_j$ and $\bar{v}_j$ may be expressed as:

$$\bar{u}_j(x,y) = \sum_{p=0,1,2} \sum_{q=0,3,4} C_{pq}^j \exp\left[i\left(k_x^{j,p}x + k_y^{j,q}y\right)\right), \tag{5.15}$$

$$\bar{v}_j(x,y) = \sum_{p=0,3,4} \sum_{q=0,1,2} D_{pq}^j \exp\left[i\left(k_x^{j,p}x + k_y^{j,q}y\right)\right), \tag{5.16}$$

In the resulting expressions, i.e. Equation (5.15) and Equation (5.16), the wave-numbers of the compression and shear waves are substituted, in accordance with equations (5.10) to (5.14). Furthermore, for notational convenience, the expansion coefficients C_{pq}^j and D_{pq}^j in Equation (5.15) and Equation (5.16) are designated here as C_k^j and D_k^j, respectively, with $k \in \{1, 2, \cdots, 9\}$, where 9 is number of constants in each equation. When storing these $9 \times 2 = 18$ coefficients in a vector

$$\mathbf{c}_j = \left[\ C_1^j, C_2^j, \ldots, C_9^j, D_1^j, D_2^j, \ldots, D_9^j\ \right]^T, \tag{5.17}$$

equations (5.15) and (5.16) can be expressed in matrix-vector format:

$$\bar{\mathbf{u}}_j = \mathbf{P}_j\mathbf{c}_j,\ \forall j = 0, 1, \cdots, L-1, \tag{5.18}$$

where the vector $\bar{\mathbf{u}}_j$ contains the two displacement functions $\bar{u}_j(x,y)$ and $\bar{v}_j(x,y)$, and the 2×18 matrix $\mathbf{P}_j$ contains the exponential functions, their products, and two times unity, in correspondence with equations (5.15) and (5.16).

It is apparent that equations (5.15) and (5.16) do not provide an exact solution to equations (5.5) and (5.6), but include a linear combination of some

interpolation functions derived from the physics of wave propagation in the waveguide under investigation. Once the coefficients of the approximation, i.e. $\mathbf{c}_j$, are obtained, the displacement field can be readily reconstructed. To determine these coefficients in such a way that the error in the wavelet transformed PDEs (5.5) and (5.6) is minimized in the $l2$ norm, the Galerkin weighted residual method is employed based on which, a finite element formulation is provided.

In order to solve for the coefficients $\mathbf{c}_j$ within a FEM-setting, a 9-noded, C^0-continuous, rectangular finite element is constructed that has two-degrees of freedom per node. The nodes are located, respectively, at the 4 corners of the element, in the middle of each of the 4 element edges, and at the element center. A standard FEM-approach is subsequently followed, where the nodal coordinates x_r, y_r of each element node $r \in \{1, 2, \cdots, 9\}$ are substituted into Equation (5.18), providing the displacements at each node. The nodal displacements of the element may be stored in a vector $\bar{\mathbf{q}}_j^e$, given by:

$$\bar{\mathbf{q}}_j^e = \begin{bmatrix} \mathbf{P}_j|_{x=x_1,y=y_1} \\ \mathbf{P}_j|_{x=x_2,y=y_2} \\ \vdots \\ \mathbf{P}_j|_{x=x_9,y=y_9} \end{bmatrix} \mathbf{c}_j = \mathbf{T}_j \mathbf{c}_j \tag{5.19}$$

As a next step, the 18×18 matrix $\mathbf{T}_j$ is inverted to solve for the 18 unknown coefficients, i.e., $\mathbf{c}_j = \mathbf{T}_j^{-1} \bar{\mathbf{q}}_j^e$. Substituting this solution back into Equation (5.18) results in:

$$\bar{\mathbf{u}}_j = \mathbf{P}_j \mathbf{T}_j^{-1} \bar{\mathbf{q}}_j^e = \mathbf{N}_j \bar{\mathbf{q}}_j^e \tag{5.20}$$

where the 2×18 matrix $\mathbf{N}_j = \mathbf{P}_j \mathbf{T}_j^{-1}$ characterises the (spectral) shape functions of the element, which need to be computed for each wavelet point j separately. Some characteristics of the shape functions are illustrated in Figure 5.1, using a discretized interval of $L = 150$ wavelet points, where the real and imaginary parts of the shape functions $\mathbf{N}_j$ for a corner node, with local coordinates x=0, y=0, of the 9-noded rectangular element are sketched over the element surface $0.03 \times 0.03\text{m}^2$. The wavelet points selected are the initial, i.e. $j = 0$, see Figure 5.1-a, and the final , i.e. $j = 149$, see Figure 5.1-b, wavelet points of the interval $\tau \in [0, L-1]$ considered.

Figure 5.1 confirms that (i) the interpolation condition, i.e. unity value for the real part $\Re(\mathbf{N}_j)$ corresponding to the chosen node and zero value at all other nodes, and (ii) the local support condition, i.e. the real and imaginary parts of the shape function vanish across the element boundary, are satisfied. Since the shape functions are C^0-continuous, the interelement displacement compatibility condition is also met. The presence of the imaginary part of a shape function is inherent to a FEM formulation in the wavelet domain, which is characterized by complex-valued parameters, such as the wavelet frequency $\bar{\omega}_j$, and the wavenumbers presented in equations (5.9) to (5.14). From Figure 5.1, it can be seen that a shape function related to the lowest wavelet point $j = 0$ represents relatively long waves of relatively low frequency, and a shape function related to

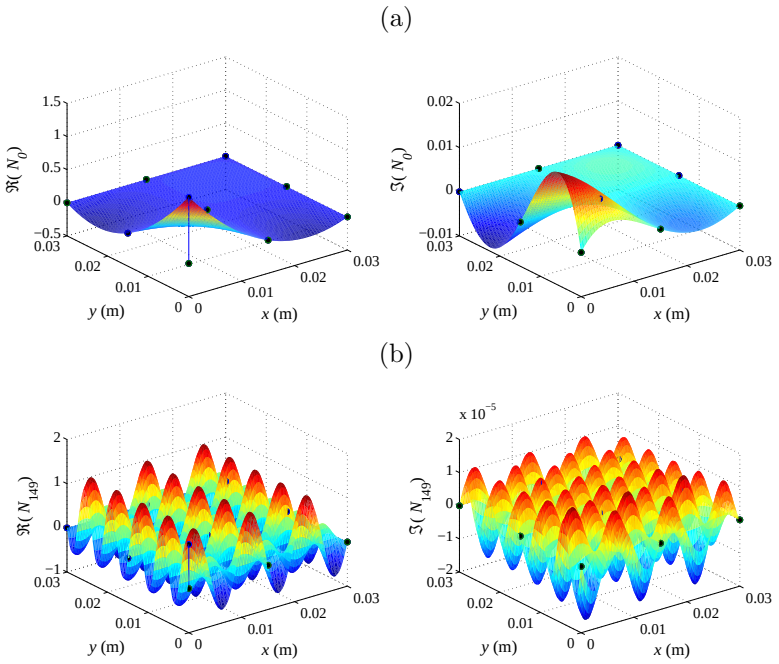

Figure 5.1: Real part $\Re(\mathbf{N}_j)$ and imaginary part $\Im(\mathbf{N}_j)$ of a FEM shape function $\mathbf{N}_j$ for two different wavelet points, plotted over the surface ($= 0.03 \times 0.03$ m^2) of a single 9-noded rectangular element. (a) Shape function $\mathbf{N}_0[1]$ of the element node 1 located at $x = 0$, $y = 0$, corresponding to the initial wavelet point $j = 0$. (b) Shape function $\mathbf{N}_{149}[1]$ of the element node 1 located at $x = 0$, $y = 0$, corresponding to the final wavelet point $j = 149 (= L - 1)$.

the highest wavelet point, $j = 149$, represents relatively short waves of relatively high frequency. The convention is such that the wavelengths corresponding to the shape functions $\mathbf{N}_j$ decreases with increasing value of the wavelet point j.

The matrix $\mathbf{N}_j$ with the element shape functions can be used in the usual way to construct the element stiffness matrix $\mathbf{K}_j^e$, and the element mass matrix $\mathbf{M}_j^e$ as:

$$\mathbf{K}_j^e = \int_{\Omega_e} (\mathbf{L}\mathbf{N}_j)^T \mathbf{D} (\mathbf{L}\mathbf{N}_j) dV \ , \ \mathbf{M}_j^e = \int_{\Omega_e} \mathbf{N}_j^T \mathbf{R} \mathbf{N}_j dV \tag{5.21}$$

in which Ω_e denotes the element volume, the 3×3 matrix $\mathbf{D}$ contains the stiffness moduli of the orthotropic material, as presented in Equation (5.22), the 3×2 matrix $\mathbf{L}$ includes the differential operators required for the computation of the strains, and the 2×2 matrix $\mathbf{R}$ contains the material density ρ, i.e.:

$$\mathbf{D} = \begin{bmatrix} Q_{11} & Q_{12} & 0 \\ Q_{21} & Q_{22} & 0 \\ 0 & 0 & Q_{66} \end{bmatrix}, \tag{5.22}$$

$$\mathbf{L} = \begin{bmatrix} \frac{\partial}{\partial x} & 0 \\ 0 & \frac{\partial}{\partial y} \\ \frac{\partial}{\partial y} & \frac{\partial}{\partial x} \end{bmatrix}, \tag{5.23}$$

and

$$\mathbf{R} = \begin{bmatrix} \rho & 0 \\ 0 & \rho \end{bmatrix}. \tag{5.24}$$

In Equation (5.21), the integration over the element volume required for computing $\mathbf{K}_j^e$ and $\mathbf{M}_j^e$ can be performed analytically, due to the exponential nature of the shape functions $\mathbf{N}_j$.

Following a weak formulation of the governing equations of the structural problem modeled, the system of equations that needs to be solved within a FEM-setting is derived in the usual way, leading to:

$$\bar{\mathbf{K}}_j \bar{\mathbf{q}}_j = \bar{\mathbf{f}}_j \tag{5.25}$$

where the dynamic stiffness matrix of the structure is given by:

$$\bar{\mathbf{K}}_j = \mathbf{K}_j + \bar{\omega}_j^2 \mathbf{M}_j \tag{5.26}$$

The mass matrix $\mathbf{M}_j$ and the stiffness matrix $\mathbf{K}_j$ are the assembly of the element mass and stiffness matrices presented in Equation (5.21), and the wavelet frequency $\bar{\omega}_j$ is as defined in Equation (3.46). Further, the nodal displacement vector $\bar{\mathbf{q}}_j$ is constructed from the element displacements presented in Equation (5.19), and the nodal force vector $\bar{\mathbf{f}}_j$ accounts for the traction boundary conditions applied along the surface S_e of the finite element via:

$$\bar{\mathbf{f}}_j = \int_{S_e} \mathbf{N}_j^T \bar{\mathbf{t}}_j dS \tag{5.27}$$

where, for simplicity, the body forces are omitted. In Equation (5.27), the tractions in the wavelet domain i.e. $\bar{\mathbf{t}}_j$, follow from the corresponding approximation coefficients $\hat{\mathbf{t}}_j$:

$$\begin{bmatrix} \bar{\mathbf{t}}_{j=0} \\ \bar{\mathbf{t}}_{j=1} \\ \vdots \\ \bar{\mathbf{t}}_{j=L-1} \end{bmatrix} = \mathbf{\Phi}^{-1} \begin{bmatrix} \hat{\mathbf{t}}_{j=0} \\ \hat{\mathbf{t}}_{j=1} \\ \vdots \\ \hat{\mathbf{t}}_{j=L-1} \end{bmatrix} \tag{5.28}$$

where $\mathbf{\Phi}^{-1}$ transforms a function from the domain of the approximation coefficients to the wavelet domain, see Section 3.4. The approximation coefficients $\hat{\mathbf{t}}_j$ appearing in Equation (5.28) are obtained component-wise from the actual, time-dependent traction $\mathbf{t}$, using the inverse relation of Equation (3.35), i.e. through performing the discrete wavelet transform. After invoking Equation (5.25) to solve for the nodal displacements $\bar{\mathbf{q}}_j$ in the wavelet domain, the approximation coefficients of the nodal displacements can be obtained via:

$$\begin{bmatrix} \hat{\mathbf{q}}_{j=0} \\ \hat{\mathbf{q}}_{j=1} \\ \vdots \\ \hat{\mathbf{q}}_{j=L-1} \end{bmatrix} = \mathbf{\Phi} \begin{bmatrix} \bar{\mathbf{q}}_{j=0} \\ \bar{\mathbf{q}}_{j=1} \\ \vdots \\ \bar{\mathbf{q}}_{j=L-1} \end{bmatrix} \tag{5.29}$$

after which the components of the time-dependent nodal displacement vector $\mathbf{q}$ are calculated using the inverse DWT, see Equation (3.35).

It should be mentioned that dissipation effects, which have been omitted in the present analysis for simplicity reasons, can be straightforwardly included in the formulation by extending Equation (5.26) with a term $\bar{\omega}_j \mathbf{C}_j$. Here, the matrix $\mathbf{C}_j$ contains the characteristics of the linear damping model used. This matrix is constructed in the same way as the mass matrix $\mathbf{M}_j$, see Equation (5.21).

The implemented WSFEM is presented schematically in Figure 5.2, in which the decoupled FEM solution procedure in the wavelet domain is shown.

5.4 Numerical Results

In order to evaluate the performance of the 9-noded element presented in the previous section, first, a benchmark problem with a well-known solution was studied. The benchmark problem relates to the propagation of Lamb waves, see Chapter 2, in an infinitely long in x-direction, homogeneous, isotropic layer of thickness H in y-direction, under plane-strain conditions in the z-direction. The layer was subjected to traction-free boundary conditions at its top, i.e. $y = H/2$, and bottom, i.e. $y = -H/2$, surfaces. The equations of motion (5.1) and (5.2), which hold for an anisotropic layer under plane-stress conditions, could be straightforwardly adapted to the case of an isotropic layer under plane-strain conditions by expressing the stiffness coefficients in Equation (5.1) and

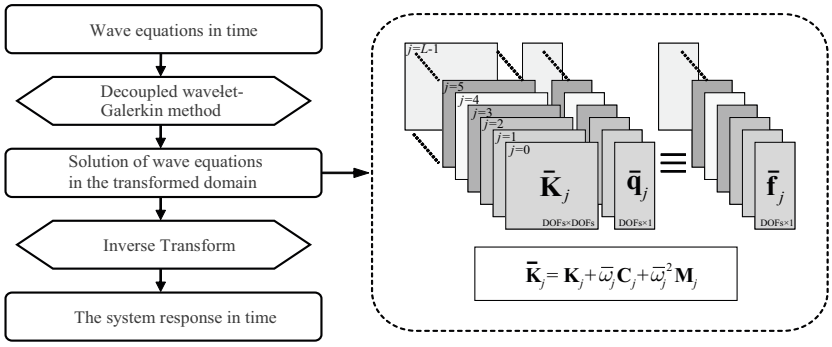

Figure 5.2: Schematic representation of the wavelet-based spectral finite element method. The decoupled wavelet-Galerkin scheme breaks down the equations of motion into a number of systems of linear equations, which can be solved in parallel.

Equation (5.2) as:

$$Q_{12} = Q_{21} = \lambda,\ Q_{66} = \mu,\ Q_{11} = Q_{22} = \lambda + 2\mu, \tag{5.30}$$

where the Lamé constants λ and μ were formulated in terms the Young's modulus E and the Poisson's ratio ν, i.e. $\lambda = \nu E/[(1+\nu)(1-2\nu)]$, and $\mu = E/[2(1+\nu)]$. The benchmark problem was solved by choosing the stiffness parameters and density in correspondence with the values for aluminium, i.e., $E = 70$GPa and $\nu = 0.3$, and $\rho = 2700\text{kg/m}^3$. The dispersion curves were obtained in the standard way, by substituting the harmonic plane wave solution for the displacements u and v, given by:

$$u(x,y,t) = \bar{u}\exp[i(\omega t - k_x x - k_y y)], \tag{5.31}$$

$$v(x,y,t) = \bar{v}\exp[i(\omega t - k_x x - k_y y)], \tag{5.32}$$

into the equations of motion (5.1), and numerically computing the non-trivial solution, known as the Rayleigh-Lamb solution, from the roots of the obtained transcendental equation Achenbach [1993], Graff [1975]. In Equation (5.32) and Equation (5.33), $\bar{u}$ and $\bar{v}$ are the wave amplitudes, k_x and k_y are the wavenumbers in x- and y-directions, and ω is the angular frequency. The Rayleigh-Lamb solution was compared to the dispersion curves computed numerically using the formulation presented in Section 5.3. In the numerical simulation, a layer of 2m long and 0.05m thick was modeled, and discretized by 640 9-noded rectangular elements, i.e., 4 elements across the thickness of the layer and 160 elements across the length. The layer was free-free, and subjected to a harmonic load with unit amplitude at its upper left corner. The frequency of the load was increased stepwise from 2 to 100kHz, using increments of 2kHz. The nodal displacements were computed in the frequency domain for each step, by solving a system of equations similar to Equation (5.25), with the wavelet parameter $\bar{\omega}_j$

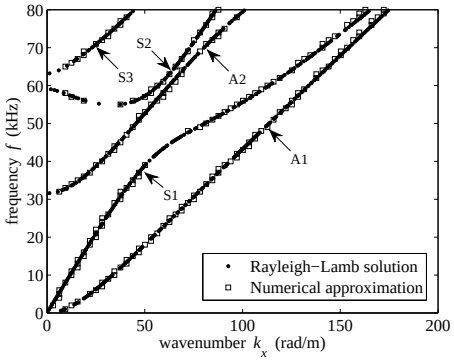

Figure 5.3: The dispersion curves for the lowest 5 modes, i.e. 3 symmetric and 2 antisymmetric modes, of a layer of thickness $H = 0.05$m.

in Equation (5.26) replaced by $i\omega$. The nodal displacements along the upper boundary of the layer, i.e., at $y = H/2$, were subsequently subjected to a Fourier transform, which provides the wave-numbers k_x characterizing the response at the frequency f considered.

The dispersion curves for the 5 lowest Lamb wave modes are presented in Figure 5.3, by plotting the frequency $f(= \omega/2\pi)$ versus the wave-number k_x in x-direction. The semi-analytical solution and the numerical solution are in very good agreement. The numerical dispersion curves presented in Figure 5.3 were directly computed in the frequency domain, i.e., a computation of the layer response in time was not required. This study hence, only reveals that the spatial discretization of the numerical formulation was adequate and precise.

In order to illustrate time discretization aspects of the WSFEM formulation, a second example was considered where a $300 \times 300 \times 1\text{mm}^3$ plane-stress, homogeneous, isotropic aluminium plate with $E = 70$GPa and $\nu = 0.3$, and $\rho = 2700\text{kg/m}^3$ was subjected to an in-plane impact load, as shown in Figure 5.4. The load had a unit amplitude and a frequency content of 0-40 kHz, and was applied in the vertical , i.e. y-, direction at the middle of the lower plate edge. The plate was supported in x- and y-directions at the two corners of the upper edge.

The displacement v in the y-direction evaluated at the center of the plate, i.e. point C, is depicted Figure 5.5 as a function of time, corresponding to (i) an accurate, reference solution computed with FEM, (ii) a FEM computation (FEM-Q) that used 9-noded quadrilateral elements with quadratic shape functions, (iii) a FEM computation (FEM-L) that used 4-noded quadrilateral elements with linear shape functions, and (iv) a computation performed using the WSFEM approach presented in this chapter. The time integration of the FEM reference solution (i) and the other two FEM solutions (ii) and (iii) was performed with a second-order accurate, central difference scheme, in correspondence with Newmark time-integration parameters equal to $\beta = 0$, $\gamma = 0.5$, see

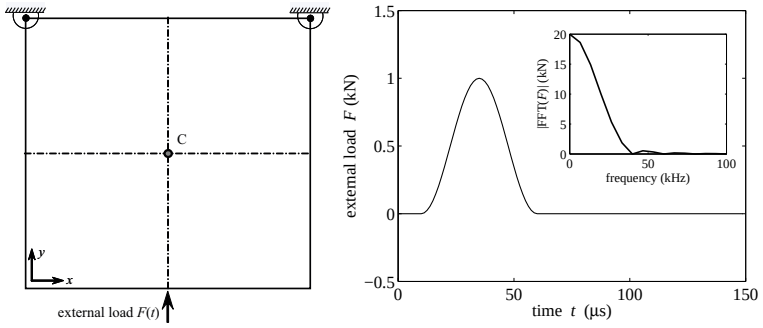

Figure 5.4: The geometry and loading: (left) the square plate ($300\times300\times1\text{mm}^3$) subjected to an external loading $F(t)$ at the lower plate edge; (right) loading characteristics as a function of time and frequency (inset).

Hughes [1987] .

The order of the Daubechies wavelets used in the WSFEM approach was $N = 6$. The number of nodes used for computations (ii), (iii) and (iv) were the same, namely 289, corresponding to meshes of $8 \times 8 = 64$ 9-noded elements and $16 \times 16 = 256$ 4-noded elements. The time increment for the FEM computations (ii) and (iii) equaled 0.1 μs, which warranted that the central difference scheme remained stable. In the WSFEM, the choice of the time increment was not critical from the stability perspective. From the accuracy point of view, preliminary WSFEM simulations showed that, for the current boundary value problem, a time increment of $\Delta t = 3.0\mu$s provides a result that does not really change in accuracy when the time interval is smaller. The time interval $\Delta t = 3.0\mu$s caused the sampling density L in the wavelet domain apparently to be sufficiently high to accurately capture the response characteristics generated by the loading specified in Figure 5.4. Note that for a given time window of interest, the connection between L and Δt is explicitly set by Equation (5.4).

In order to generate a FEM reference solution constructed with 9-noded quadrilateral elements with a relatively high spatial accuracy, the total number of nodes was taken to be considerably larger than for the other three solutions, namely 58081 nodes corresponding to $120 \times 120 = 14400$ elements, while the discrete time step was taken to be significantly smaller, i.e. $\Delta t = 0.005\mu$s. The time window used for the simulations was $t_{end} = 150\mu$s. It can be observed from Figure 5.5 that the calculated responses look qualitatively similar, and that the WSFEM solution provided the best approximation to the reference solution. The accuracy of the FEM-Q solution was slightly less than that of the WSFEM solution, while the FEM-L was the least accurate, especially during the last 30μs of the response. As the mesh become finer, all methods converge to the reference solution as demonstrated in Figure 5.6 for 6561 nodes. In this case also, the WSFEM provides a better accuracy than FEM-L and FEM-Q.

In order to quantitatively compare the convergence behavior of the WSFEM,

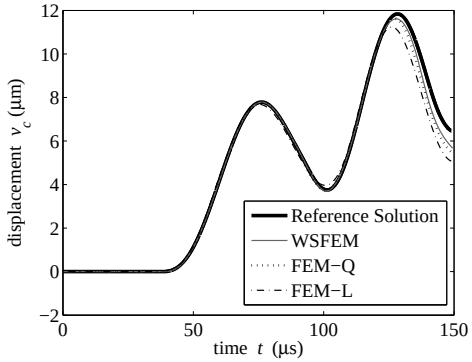

Figure 5.5: Vertical displacement v at the center of the plate, i.e. point C in Figure 5.4. The WSFEM and FEM-Q and FEM-L solutions constructed with meshes of 289 nodes are compared to a FEM reference solution.

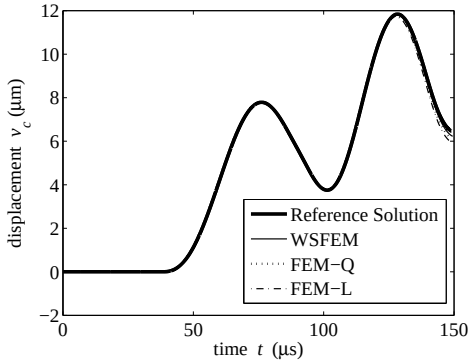

Figure 5.6: Vertical displacement v at the center of the plate, i.e. point C in Figure 5.4. The WSFEM and FEM-Q and FEM-L solutions constructed with meshes of 6561 nodes are compared to a FEM reference solution.

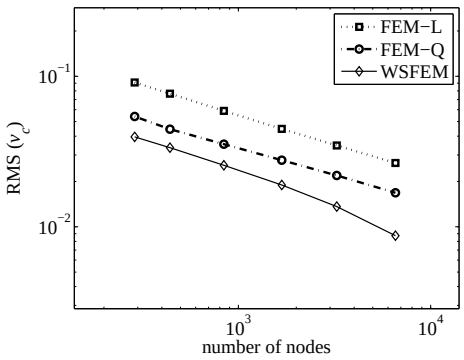

Figure 5.7: The RMS error in nodal displacement under mesh refinement.

FEM-L and FEM-Q solutions under mesh refinement, the root mean square (RMS) error of the vertical displacement v_C at point C was computed as:

$$RMS = \left(\frac{\int_0^{t_{end}} \left[v_C(t) - v_{C,ref}(t) \right]^2 dt}{\int_0^{t_{end}} \left[v_{C,ref}(t) \right]^2 dt} \right)^{\frac{1}{2}} \tag{5.33}$$

with $v_{C,ref}$ the vertical displacement related to the FEM reference solution and $t_{end} = 150\mu$s. The integral in Equation (5.33) was computed using direct numerical integration, similar to the previous example. The RMS error is depicted in Figure 5.7, illustrating that the mesh convergence rate is similar for the three solutions, but that the WSFEM solution had the smallest error for an arbitrarily mesh fineness, followed by the FEM-Q solution and the FEM-L solution. A certain value of RMS error can be achieved by a few times less degrees of freedom in the WSFEM compared to the FEM-L. This result is consistent with the result plotted in Figure 5.5.

In addition to the RMS error, the convergence of the residual error in the strong form of the governing equations may be examined. The residual error is calculated by taking the $l2$, i.e. Euclidian, norm of the residuals of the equations of motion (5.1) and (5.2) evaluated at the plate center (i.e., point C, see Figure 5.4-a). The convergence rate of this residual error turns out to be similar for the WSFEM and FEM-Q computations, in a sense that it decreases with a factor 5 to 6 when the number of elements is increased by a factor of 25. Conversely, for the FEM-L simulation, the decrease in the residual error is negligible for this increase in mesh refinement.

Finally, the time evolution of the displacement v in y-direction was considered over the whole plate using the WSFEM solution for the isotropic plate with $10 \times 10 = 100$ elements, see Figure 5.8-a. The effect of anisotropy becomes clear when the structural response of an orthotropic plate is compared to that of an orthotropic plate depicted in Figure 5.8-b. For the orthotropic plate, the stiffness in the x-direction was taken 25% higher than for the isotropic, alu-

minum plate, i.e., $E_1 = 87.5$GPa, while in y-direction the stiffness was 25% lower, $E_2 = 52.5$GPa. The value of the Poisson's ratio $\nu_{12} = 0.25$, which, due to symmetry of the stiffness tensor, corresponds to $\nu_{21} = E_1\nu_{12}/E_2 = 0.42$, (see Equation (5.3)), and the shear modulus $G_{12} = 35$GPa. The densities in both cases were similar, i.e. 2700 kg/m^3. As shown in Figure 5.9-a, the analysis was further extended by considering the response of a composite plate consisting of the above-mentioned isotropic material at the lower part of the plate, and the orthotropic material at the upper part of the plate. As indicated by the black line, an interface with perfect bonding and a rectangular tooth geometry, tooth length=tooth width=0.1m, connected the two materials in the middle of the plate. The effect of an irregular plate boundary on the response characteristics was examined in Figure 5.9-b, by providing the composite plate of Figure 5.9-a with a $50 \times 50 \times 1$mm^3 cut-out at its lower right corner.

The contour plots in Figure 5.8 and Figure 5.9 illustrate that at $t = 36\mu$s, only part of the load signal had yet been applied, resulting into a compression (P) wave propagating along the trajectory $x = 0.15$m, a shear (S) wave propagating along the trajectory $y = 0$, and a combination of these two waves propagating along other trajectories. At $t = 59\mu$s, the front of the P wave had passed the plate center, where a comparison between Figure 5.8-a and 7b shows that the wave front for the orthotropic case was more straight than for the isotropic case, due to the different stiffness parameters in x- and y-directions. From the location of the P wave front along $x = 0.15$m, it may be concluded that the P wave velocity in the y-direction in the orthotropic plate is lower than in the isotropic plate, which can be ascribed to the lower stiffness of the orthotropic material in the y-direction. It is further indicated in Figure 5.8-a and Figure 5.8-b that at $t = 84\mu$s, the fronts of P and S waves had reached the plate boundaries, which led to interference between incident waves and waves reflected at the boundaries. At $t = 108\mu$s, the tails of incident P and S waves had also reached the plate boundaries, which further intensified the interference pattern of the incident and the reflected waves.

From the response of the composite plate in Figure 5.9-a, it can be observed that at $t = 84\mu$s, waves propagating from the lower, isotropic part of the plate had reflected, and refracted, at the interface with the orthotropic part, as a result of which the displacement pattern in the isotropic part of the plate had become different from that of the isotropic plate in Figure 5.8-a. Due to additional wave reflections, this difference grew with time, as illustrated by the displacement patterns for $t = 108\mu$s in Figure 5.8-a and Figure 5.9-a. The effect of the cut-out on the dynamic response was apparent from breakage of the vertical symmetry of the displacement pattern after the P and S waves had reached the left and right plate boundaries, see Figure 5.9-b for $t = 84\mu$s and $t = 108\mu$s.

The above examples show that the WSFEM method is suitable for simulating elastic wave propagation problems in an accurate and efficient manner. The main strength of the present method is that it combines the wavelet-Galerkin method and FEM in an optimal way, i.e., the wavelet-Galerkin method is used only for the temporal discretization of the problem, making the method suitable for parallel computation, and FEM is employed for the spatial discretization

of the problem, as a result of which, geometries and boundary conditions of arbitrary complexity can be modeled.

5.5 Concluding Remarks

A WSFEM formulation has been proposed for the analysis of 2D elastic wave propagation problems. The method uses a wavelet-Galerkin approach for transforming the governing equations from the time domain to the wavelet domain, after which the spatial dependency of the displacement response is solved for in the wavelet domain by means of FEM endowed with exponential shape functions. The final response is obtained by transforming the computed nodal displacements from the wavelet domain back to the time domain.

A WSFEM approach was proposed and formulated in this chapter to simulate elastic wave propagation in 2D waveguides. The method uses the wavelet-Galerkin approach for transforming the governing equations from the time domain to the wavelet domain, after which the spatial dependency of the governing equations was solved using a spectral FEM equipped with exponential shape functions. The response was subsequently transformed back to the time domain by employing the inverse transform.

The performance of the WSFEM approach was compared to that of a standard FEM approach, showing that the accuracy of WSFEM was similar to that of FEM equipped with quadratic shape functions and a second-order accurate, Newmark explicit, i.e. Newmark-β, time-integration scheme. In terms of computational efficiency, the WSFEM approach offers a significant advantage to using FEM equipped with a direct time-integration scheme, in a sense that the time-discretized equations can be solved for each wavelet point separately. This makes the WSFEM approach inherently suitable for parallel computation. Another appealing feature of the WSFEM is the stability of the time discretization scheme, which allows us to use relatively large time intervals in the computation of the response. Extension of the WSFEM to 3D structures will be discussed in the next chapter.

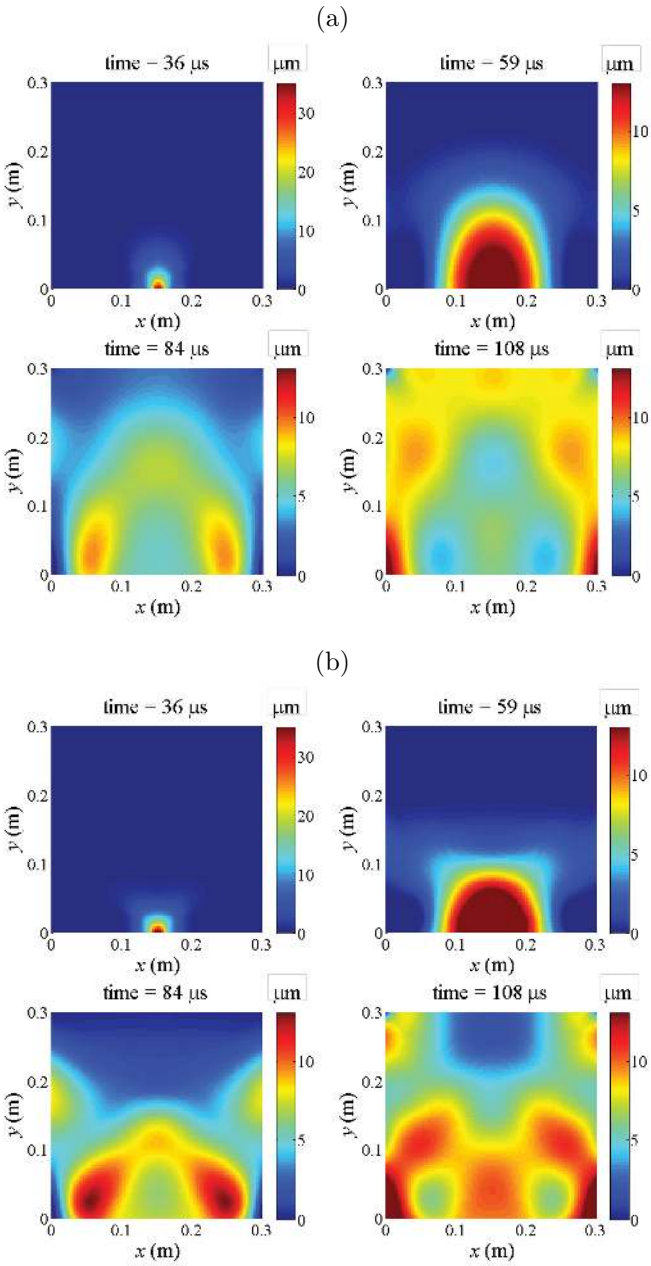

Figure 5.8: Contour plot of the displacement v in the y-direction; (a) isotropic plate, (b) orthotropic plate.

(a)

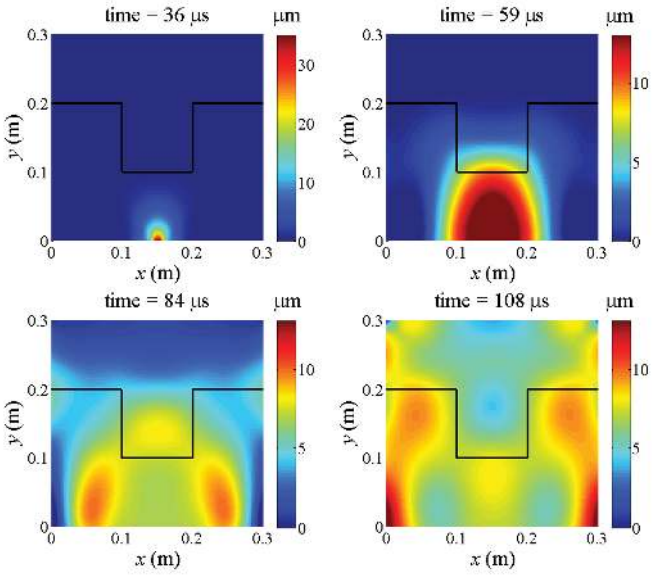

(b)

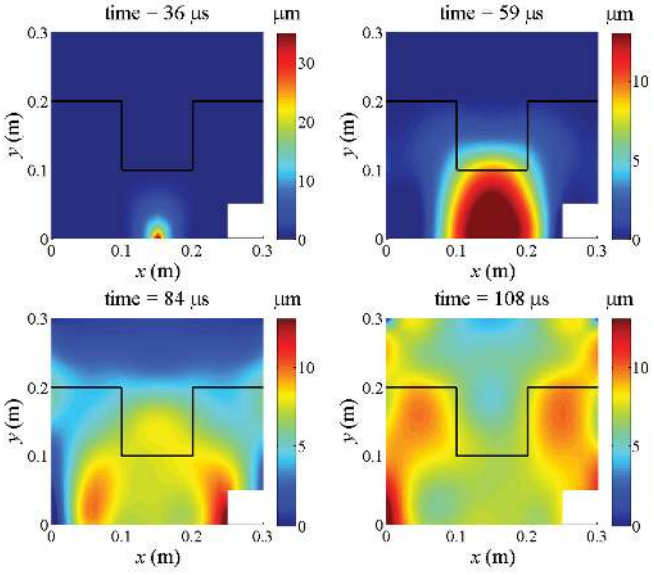

Figure 5.9: Contour plot of the displacement v in the y-direction; (a) heterogeneous plate, (b) heterogeneous plate with cut-out.

Chapter 6

Generalization of the WSFEM: Spectral Formulation of Finite Element Methods

A novel and generic formulation of the wavelet-based spectral finite element approach, which is applicable to linear transient dynamics and elastic wave propagation problems, is presented in this chapter[1].

The fact that Daubechies wavelets [Daubechies, 1992], as presented in Chapter 3, possess several appealing properties such as orthogonality, compact support, exact representation of polynomials up to a certain degree, and an ability to represent functions at different resolutions, has resulted in the extensive use of wavelets in signal processing [Abbate et al., 1997, Daubechies, 1992, Giurgiutiu, 2008, Mallat, 1989], electromagnetics [Fujii and Hoefer, 2003, Karumpholz and Katehi, 1996], and computational fluid and solid mechanics [Amaratunga and Williams, 1997, Amaratunga et al., 1994, Beylkin, 1992, Chen and Hwang, 1996, Chen et al., 1996, Han et al., 2006, Ko et al., 1995, Ma et al., 2003, Patton and Marks, 1996, Qian and Weiss, 1993]. Among these applications, the use of Daubechies compactly-supported wavelets for spectral analysis of elastic wave propagation was suggested and has mainly been pursued by Mitra and Gopalakrishnan [Mitra and Gopalakrishnan, 2006d, 2007, 2005, 2006a,b]. This approach is referred to as *conventional wavelet-based spectral finite element method* in this dissertation. Gopalakrishnan and Mitra [2010] use the Daubechies wavelets in a Galerkin sense as an alternative to the fast Fourier transform (FFT) to alleviate the issues arising from the imposed periodicity in the formulation of

[1]The article "Spectral Formulation of Finite Element Methods Using Daubechies Compactly-Supported Wavelets for Elastic Wave Propagation Problems", Pahlavan et al. [2012b] in Wave Motion, has been extracted from the content of this chapter.

the Fourier transform. Their investigations have shown improvements in the required computational power, in comparison with the FFT-based analysis, by taking advantage of avoiding a periodicity assumption and the compact support of Daubechies wavelets. As mentioned in chapters 4 and 5, despite the significant progress achieved by Mitra and Gopalakrishnan, there are still difficulties to overcome, when dealing with 2D and 3D problems with geometrical complexities and non-periodic boundary conditions. The wavelet-based spectral analysis, in analogy with the FFT-based spectral analysis, employs global orthogonal bases for transformation of the governing equations from the time domain to the frequency domain, and from the physical spatial domains to the wavenumber domains, to convert a system of multi-dimensional partial differential equations (PDEs) to a set of ordinary differential equations (ODEs) [Doyle, 1989, Farris and Doyle, 1989, Gopalakrishnan et al., 1992, 2008]. Dealing with engineering structures with directional properties and local variations in the structural characteristics, however, can not be handled straight-forwardly in a non-physical domain, i.e. the wavenumber domain. Regarding the inflexibility of the conventional wavelet-based spectral method in dealing with non-basic geometries, the author suggested an alternative solution in Chapter 5, i.e. applying the wavelet-Galerkin method temporally and using a tailored finite element method for the spatial discretization, the shape functions of which were based on the wavenumbers corresponding to the introduced frequencies in the transformed wavelet domain. Improvements over the time domain standard finite element method (FEM) with linear and quadratic basis functions was demonstrated using the proposed wavelet-based finite element method (WSFEM), which was more pronounced in the temporal discretization. As a next step, the formulation needs to be extended to capture the response of more complex structures used in the engineering world. Although the approach proposed in Chapter 5 offers an improved framework to deal with 2D structures, the non-standard finite element formulation with frequency-dependent approximation bases, which requires incorporation of more wave modes in more complex media, introduces complexities in the formulation that may hinder its extension to 3D waveguides and structures.

A novel framework for elastic wave propagation simulation is proposed and formulated in the present chapter, which can combine a wavelet-based spectral analysis for the temporal discretization, with any standard finite element spatial discretization scheme, on the basis of their complementary merits. Employing the wavelet-Galerkin method described in Chapter 3 of this dissertation, the variational principle of virtual work is expressed in a temporally-transformed domain. After a subsequent decoupling projection, the wavelet frequencies corresponding to the temporal discretization are introduced. The resulting equations are coupled only spatially. The variational problem hence, can be reduced to a set of temporally independent problems, which can be solved using any spatial discretization method, e.g. FEM. Note that the 2D WSFEM presented in Chapter 5, is a special case of the formulation presented in this chapter. Since the 3D WSFEM allows for the solution corresponding to each virtual frequency separately, the computations can be performed in parallel, in analogy

with the 1D and 2D formulations in chapters 4 and 5. Although applicable to all finite element schemes, the focus of the presented numerical examples is on the so-called spectral element method (SEM) outlined in Chapter 2. In SEM, higher-order polynomials are used as basis functions and the element nodes are located on Gauss-Lobatto-Legendre (GLL) points thereby having hp-refinement and spectral convergence properties [Komatitsch et al., 2000, Peng et al., 2009]. Accurately capturing the geometry through the isoparametric formulation is possible in the present formulation due to the higher order basis functions in SEM. As a result of the wavelet-Galerkin method used, the wavelet-based spectral finite element method (WSFEM) has spectral convergence also with respect to the temporal discretization.

Using 3D numerical examples, the features of the presented WSFEM method are demonstrated and the possible ways of improving the solution speed are discussed in this chapter. Having verified the accuracy of the WSFEM formulation and its implementation, a composite laminate fully discretized with 3D SEM elements is modeled. The distribution of the displacement, the strain, and the stress fields are obtained, which provide detailed information about the symmetric and antisymmetric Lamb waves propagating through such a complex waveguide.

6.1 Temporal Discretization: Spectrally-implemented Principle of Virtual Work

The decoupled wavelet-Galerkin method (DWG) introduced in Chapter 3, is applied to the variational principle of virtual work in this section. Principle of virtual work permits derivation of the equations of motion from a definite integral involving the virtual internal work, i.e., strain energy, of a body and the virtual work performed by external forces [Reddy, 2005, 2007]. The corresponding virtual displacements are hypothetical and arbitrary, and the actual loads act on their fixed values.

The virtual strain energy of an elastically deformed body is given by:

$$\delta U = \int_{\Omega} \boldsymbol{\sigma} : \delta\boldsymbol{\epsilon}\, dv, \tag{6.1}$$

where $\boldsymbol{\sigma}$ and $\boldsymbol{\epsilon}$ are respectively, the second-order stress and strain tensors, (:) indicates the tensor product, and dv denotes the volume element in the material body $\Omega \subseteq \mathbb{R}^3$. The relation between the stress and the strain tensors in a linear elastic material obeys the Hooke's law:

$$\boldsymbol{\sigma} = \mathbf{C} : \boldsymbol{\epsilon}. \tag{6.2}$$

In the equation above, $\mathbf{C}$ is the forth-order stiffness tensor. Denoting the displacement vector by $\mathbf{u} : \Omega \times t \rightarrow \mathbb{R}^3$, where t is the real time, the second-order strain tensor can be expressed by:

$$\boldsymbol{\epsilon} = \frac{1}{2}\left[\nabla\mathbf{u} + (\nabla\mathbf{u})^T\right]. \tag{6.3}$$

The virtual displacement vector $\delta\mathbf{u}$ is composed of the variations of the dependent variables, i.e. degrees of freedom, which can be varied separately and independently [Doyle, 1989]. Using the reduced Voigt notation, the Hooke's law in Equation (6.2) can be rewritten as:

$$\begin{pmatrix} \sigma_x \\ \sigma_y \\ \sigma_z \\ \sigma_{yz} \\ \sigma_{xz} \\ \sigma_{xy} \end{pmatrix} = \begin{pmatrix} C_{11} & C_{12} & C_{13} & C_{14} & C_{15} & C_{16} \\ C_{21} & C_{22} & C_{23} & C_{24} & C_{25} & C_{26} \\ C_{31} & C_{32} & C_{33} & C_{34} & C_{35} & C_{36} \\ C_{41} & C_{42} & C_{43} & C_{44} & C_{45} & C_{46} \\ C_{51} & C_{52} & C_{53} & C_{54} & C_{55} & C_{56} \\ C_{61} & C_{62} & C_{63} & C_{64} & C_{65} & C_{66} \end{pmatrix} \begin{pmatrix} \epsilon_x \\ \epsilon_y \\ \epsilon_z \\ 2\epsilon_{yz} \\ 2\epsilon_{xz} \\ 2\epsilon_{xy} \end{pmatrix}. \tag{6.4}$$

Note that in this notation, the stiffness matrix in the reduced notation remains symmetric i.e.:

$$C_{ij} = C_{ji} \ \forall i, j = 1 \text{ to } 6. \tag{6.5}$$

The total virtual work of a deformable solid body is divided into the contribution of the virtual work of external forces and internal forces. The virtual work of external forces can be broken further into the virtual work of the surface loads, i.e. δW^s, and the virtual work of the body forces, i.e. δW^b. Hence:

$$\delta W = (\delta W^s + \delta W^b) - \delta U, \tag{6.6}$$

Using the D'Alembert's principle, the inertia forces can also be treated as body forces [Doyle, 1989]. Hence:

$$\delta W^b = \delta W^v + \delta W^d = \int_\Omega \mathbf{f}^b \cdot \delta\mathbf{u} dv - \int_\Omega \rho\ddot{\mathbf{u}} \cdot \delta\mathbf{u} dv. \tag{6.7}$$

where δW^d is the virtual work of the inertia forces, and δW^v denotes the virtual work done by the rest of the body forces denoted by $\mathbf{f}^b$. The principle of virtual work states that the body is in equilibrium, if the total vitual work is zero for every independent kinematically-admissible virtual displacement δu [Doyle, 1989]:

$$\int_{t_1}^{t_2} \delta \left[W^s + W^v + W^d - U \right] dt = 0. \tag{6.8}$$

To tackle dynamic problems, often, the Hamilton's principle is derived from the principle of virtual work, which reformulates the virtual work of the inertia forces in terms of the virtual kinetic energy of the body [Reddy, 2005, Doyle, 1989]. Subsequently, taking the variation with respect to each dependent variable leads to the strong form of m governing equations, and the corresponding boundary conditions, where m denotes the number of dependent variables, see Reddy [2005] for the details. For extraction of the governing equations and the boundary conditions, the integrand equivalent to the one in Equation (6.8), can be set to zero, since the components of the virtual displacement vector can

be varied separately and independently, and the integral bounds are arbitrary [Doyle, 1989].

In this study, alternatively, since only the weak form of the governing equations is desired, which will be later solved using the finite element method, derivation of the strong form of the equations is omitted. Following the standard FEM, the boundary conditions are approximated and applied through the finite element formulation, similar to Chapter 5 of this dissertation. In addition, the use of the wavelet-Galerkin method circumvented the derivation of Hamilton's principle, as it can straight-forwardly handle the derivatives with respect to time. The integrand in the principle of virtual work, i.e. Equation (6.8), is set to zero, for the same reason as in the Hamilton's principle explained above.

To employ the wavelet-Galerkin method (see Chapter 3), assume the actual displacement field, the external forces, and the body forces to be discretized at L equally-spaced points in time separated by the time interval Δt. To avoid dealing with wavelet parameters at non-integer points, as discussed in Section 3.4, the dimensionless time τ can be utilized such that,

$$t_\tau = \tau \Delta t \,; \forall \tau \in [0, L-1]. \tag{6.9}$$

The corresponding virtual energies and works in Equation (6.8) can be expressed by applying the wavelet transform in accordance with Equation (3.35). Indicating the approximation coefficients of a function by the *hat*-sign, and the translates of the wavelet scaling function by φ_k, $k \in \mathbb{Z}$, it can be written that:

$$\sum_k \delta \hat{W}^s_k \varphi_k + \sum_k \delta \hat{W}^v_k \varphi_k - \sum_k \delta \hat{U}_k \varphi_k - \Delta t^{-2} \sum_k \rho \delta \hat{B}_k \ddot{\varphi}_k = 0, \tag{6.10}$$

where, based on the fact that the variation $\delta \mathbf{u}$ can be varied separately and arbitrarily at each time instant [Doyle, 1989], the normalized virtual energy $\delta \hat{B}_k$ is introduced as:

$$\delta \hat{B}_k = \int_\Omega \hat{\mathbf{u}}_k . \delta \mathbf{u} dv = \int_\Omega \hat{\mathbf{u}}_k . \delta \hat{\mathbf{u}}_k dv. \tag{6.11}$$

Also note that the term Δt^{-2} in Equation (6.10) appears as a result of the change of variable from t to the dimensionless time τ. In accordance with the wavelet-Galerkin method presented in Chapter 3, one can take the inner product on both sides of Equation (6.10) with φ_j for $j = 0, 1, \cdots, L-1$ as:

$$\sum_k \left[\delta \hat{W}^s_k \langle \varphi_k, \varphi_j \rangle + \delta \hat{W}^v_k \langle \varphi_k, \varphi_j \rangle - \delta \hat{U}_k \langle \varphi_k, \varphi_j \rangle - \Delta t^{-2} \rho \delta \hat{B}_k \langle \ddot{\varphi}_k, \varphi_j \rangle \right] = 0. \tag{6.12}$$

Accordingly, the following form of the principle of virtual work for $j = 0, 1, \cdots, L-1$ can be obtained:

$$\sum_k \delta \hat{W}^s_k \Gamma^0_{k-j} + \sum_k \delta \hat{W}^v_k \Gamma^0_{k-j} - \sum_k \delta \hat{U}_k \Gamma^0_{k-j} - \Delta t^{-2} \sum_k \rho \delta \hat{B}_k \Gamma^2_{k-j} = 0. \tag{6.13}$$

where Γ^i_{k-j}, for $i = 1, 2$, denotes the zeroth- and the second-order connection coefficients of Daubechies wavelets derived in Section 3.4. Rearrangement of

the above L equations in a matrix-vector configuration can be represented as follows:

$$\delta\hat{\mathbf{W}}^s + \delta\hat{\mathbf{W}}^v - \delta\hat{\mathbf{U}} - \Delta t^{-2}\rho{\mathbf{\Lambda}_0}^{-1}\mathbf{\Lambda}_2\delta\hat{\mathbf{B}} = 0, \tag{6.14}$$

where $\mathbf{\Lambda}_0$ and $\mathbf{\Lambda}_2$, as introduced in Section 3.4, are each a band-limited matrix the components of which are the values of the zeroth- and second-order connection coefficients. Equation (6.14) is a coupled system of L homogenous partial differential equations, similar to the formulation in chapters 3, 4, and 5. Equation (6.14) expresses the relationship between the adjacent displacements in time. The bandwidth of the matrix ${\mathbf{\Lambda}_0}^{-1}\mathbf{\Lambda}_2$ is determined by the order of the compactly-supported wavelets N. Higher order wavelets correlate more time steps through a wider matrix band. These matrices however, are independent of the material or geometrical properties of the problem and vary only with the number of sampling points.

The coupled set of equations (6.14) can be subsequently decoupled through the eigendecomposition of ${\mathbf{\Lambda}_0}^{-1}\mathbf{\Lambda}_2$. Similar to chapters 3, 4, and 5, the projection of the approximation coefficients vector of a scalar function f denoted by $\hat{\mathbf{f}}$, on the eigenspace of ${\mathbf{\Lambda}_0}^{-1}\mathbf{\Lambda}_2$ denoted by an over-bar and called the transformed domain, can be accordingly obtained by:

$$\bar{\mathbf{f}} = \mathbf{\Phi}^{-1}\hat{\mathbf{f}}, \tag{6.15}$$

where $\mathbf{\Phi}$ is the eigenvector basis of ${\mathbf{\Lambda}_0}^{-1}\mathbf{\Lambda}_2$. Each of the L temporally-decoupled PDEs corresponding to equations (6.14) can be solved independently. These equations for the wavelet points $j = 0, 1, \cdots, L-1$ are:

$$\delta\bar{W}_j^s + \delta\bar{W}_j^v - \delta\bar{U}_j - \Delta t^{-2}\rho\lambda_j^2\delta\bar{B}_j = 0, \tag{6.16}$$

with λ_j^2 the jth eigenvalue of ${\mathbf{\Lambda}_0}^{-1}\mathbf{\Lambda}_2$. Equation (6.16) is the principle of virtual work expressed via the DWG. Equation (6.16) can also be written as:

$$\delta\left[\bar{W}_j^s + \bar{W}_j^v - \bar{U}_j - \rho\bar{\omega}_j^2\bar{B}_j\right] = 0, \tag{6.17}$$

where the wavelet frequency is $\bar{\omega}_j = \Delta t^{-1}\lambda_j$, i.e. the eigenvalues of ${\mathbf{\Lambda}_0}^{-1}\mathbf{\Lambda}_2$ scaled by the reciprocal of the time interval. Note that since ${\mathbf{\Lambda}_0}^{-1}\mathbf{\Lambda}_2$ is not a symmetric matrix, its eigenvalues are in general, complex numbers.

The transient problem is now broken down into a set of temporally-uncoupled system of PDEs which can be solved in parallel for different wavelet points. These equations can be therefore solved at each wavelet point, using an approximate solution method such as the finite element method, the finite difference method, the boundary element method, etc. A linear combination of the transformed responses at the wavelet points weighted in accordance with Equation (6.15), brings the response back into the real time.

On the independence of the solution steps, physically speaking, the solution in time is a weighted superposition of the system response to a set of virtual frequencies defined at the discrete wavelet points in analogy with the Fourier domain analysis. Alternatively speaking, there exists a subspace onto which,

temporally-linear-second-order equations can be projected and appear in a decoupled fashion.

As mentioned in Chapter 3, the DWT generally requires extra attention to be paid to the edges of the time window of interest, due to the edge effects of the wavelets. This can be dealt with using different approaches as discussed in sections 3.6 and 3.7. In this chapter, the method suggested by the author in Section 3.7 and applied in chapters 4 and 5, is employed, which is based on a finite integration domain for computation of the connection coefficients. Note again that as a result of the integration on a finite interval equal to the length of the non-dimensional time window of interest, despite the orthogonality of the scaling functions of Daubechies wavelets, the connection coefficient matrix $\mathbf{\Lambda}_0$ becomes non-diagonal. This technique makes the approach free of edge effects for problems with zero initial conditions. Although not studied in this dissertation, the capacitance matrix method [Qian and Weiss, 1993], or an extrapolation-based scheme [Williams and Amaratunga, 1997] may be adopted for non-zero initial conditions.

6.2 Spatial Discretization: Wavelet-based Spectral Finite Element Formulation

A Galerkin approach for spatial discretization of the weak form of the governing equation, i.e. Equation (6.17), can be adopted by choosing the same basis (trial) functions and weighting (test) functions, to approximate the displacement field. The chosen basis functions can be used for both the real and imaginary parts of the dependant variables at different wavelet points thereby, in contrast to the 2D formulation in Chapter 5, obtaining a fixed stiffness and mass matrices throughout the analysis.

First, the approximation coefficients of the displacement field $\mathbf{u}$, in accordance with Equation (3.35), are obtained by:

$$\mathbf{u} = \sum_k \hat{\mathbf{u}}_k \varphi_k. \tag{6.18}$$

Analogous to Equation (6.15), the displacement field in the domain of the approximation coefficients and the displacement field in the wavelet domain are correlated as:

$$\begin{bmatrix} \bar{\mathbf{u}}_{j=0} \\ \bar{\mathbf{u}}_{j=1} \\ \vdots \\ \bar{\mathbf{u}}_{j=L-1} \end{bmatrix}_{L\times 3} = \mathbf{\Phi}^{-1} \begin{bmatrix} \hat{\mathbf{u}}_{j=0} \\ \hat{\mathbf{u}}_{j=1} \\ \vdots \\ \hat{\mathbf{u}}_{j=L-1} \end{bmatrix}_{L\times 3}. \tag{6.19}$$

The selection of basis functions can follow any of the available standard forms. At wavelet point j, the vector of the transformed dependent variables $\bar{\mathbf{u}}_j$, can be expressed in terms of the nodal displacements vector $\bar{\mathbf{q}}_j^e$ through the matrix of shape functions $\mathbf{N}^e$. In Cartesian coordinate system:

$$\bar{\mathbf{u}}_j(x, y, z) = \mathbf{N}^e(x, y, z)\bar{\mathbf{q}}_j^e. \tag{6.20}$$

As mentioned above, $\mathbf{N}^e$ is not a function of j, i.e. wavelet point. By invoking Equation (6.20), the energy functionals in Equation (6.17) can be expressed in the element level by the following relations:

$$\bar{U}_j = \frac{1}{2}\int_{\Omega_e} \bar{\boldsymbol{\epsilon}}_j^T \mathbf{D}\bar{\boldsymbol{\epsilon}}_j dv = \frac{1}{2}\int_{\Omega_e} \bar{\mathbf{q}}_j^{e^T} \mathbf{B}^{e^T}\mathbf{D}\mathbf{B}^e\bar{\mathbf{q}}_j^e dv \tag{6.21}$$

$$\bar{B}_j = \frac{1}{2}\int_{\Omega_e} \bar{\mathbf{u}}_j^T \bar{\mathbf{u}}_j dv = \frac{1}{2}\int_{\Omega_e} \bar{\mathbf{q}}_j^{e^T} \mathbf{N}^{e^T}\mathbf{N}^e\bar{\mathbf{q}}_j^e dv \tag{6.22}$$

$$\bar{W}_j^s = \int_{\Omega_e} \bar{\mathbf{u}}_j^T \bar{\mathbf{f}}_j^s dv = \int_{\Omega_e} \bar{\mathbf{q}}_j^{e^T} \mathbf{N}^{e^T}\bar{\mathbf{f}}_j^s dv \tag{6.23}$$

where $\bar{\mathbf{f}}_j^s$ is the vector of surface tractions, $\mathbf{D}$ denotes the constitutive matrix, and $\mathbf{B}^e$ definend by:

$$\mathbf{B}^e = \mathbf{L}\mathbf{N}^e, \tag{6.24}$$

is the strain-nodal displacements matrix with $\mathbf{L}$ being the linear differential operator relating the strain field to the displacement field:

$$\mathbf{L} = \begin{pmatrix} \frac{\partial}{\partial x} & 0 & 0 & 0 & \frac{\partial}{\partial z} & \frac{\partial}{\partial y} \\ 0 & \frac{\partial}{\partial y} & 0 & \frac{\partial}{\partial z} & 0 & \frac{\partial}{\partial x} \\ 0 & 0 & \frac{\partial}{\partial z} & \frac{\partial}{\partial y} & \frac{\partial}{\partial x} & 0 \end{pmatrix}^T. \tag{6.25}$$

Note that the body forces are neglected for the sake of simplicity. Using relations (6.21) to (6.23), the finite element solution of Equation (6.17) in the jth decoupled wavelet point can be obtained by taking the variation with respect to the nodal displacement vector $\bar{\mathbf{q}}_j^e$. This operation at the global level for a linearly damped system will lead to:

$$\left(\mathbf{K} + \bar{\omega}_j\mathbf{C} + \bar{\omega}_j^2\mathbf{M}\right)\bar{\mathbf{q}}_j = \bar{\mathbf{f}}_j, \tag{6.26}$$

where $\bar{\mathbf{q}}_j$ denotes the global nodal displacement vector at the jth point of transformed domain. The matrices $\mathbf{K}$, $\mathbf{C}$ and $\mathbf{M}$ are respectively, the stiffness, the damping and the mass matrices. The transformed global vector of the external forces is shown on the right-hand-side of the equation by $\bar{\mathbf{f}}_j$. The matrices of Equation (6.26) are computed in accordance with the standard finite element method, by assembling the corresponding matrices at the element level:

$$\mathbf{K} = \bigcup_{e=1}^{N_{el}} \mathbf{K}^e,\ \mathbf{M} = \bigcup_{e=1}^{N_{el}} \mathbf{M}^e,\ \bar{\mathbf{f}}_j = \bigcup_{e=1}^{N_{el}} \bar{\mathbf{f}}_j^e,\ \mathbf{C} = \bar{\alpha}_j\mathbf{K} + \bar{\beta}_j\mathbf{M}, \tag{6.27}$$

where N_{el} is the total number of elements, and $\bar{\alpha}_j$ and $\bar{\beta}_j$ denote the frequency-dependent damping coefficient. For computation of the matrices in Equation (6.27), the SEM is utilized by employing higher-order Lagrange polynomials in conjunction with Gauss-Lobatto-Legendre (GLL) points and the GLL nodal quadrature, see Chapter 2. Following an isoparametric formulation and introducing the mapping $\mathbf{J}_e$ from the element domain Ω_e to the reference domain

with coordinates (ξ, η, γ) on $[-1, 1]^3$, the mass, stiffness, and the nodal forces in the element level can be computed as:

$$\mathbf{M}^e = \int_{\Omega_e} \mathbf{N}^{eT} \rho^e \mathbf{N}^e dv$$

$$= \rho^e \sum_{i=1}^{N_1+1} \omega_i \sum_{n=1}^{N_2+1} \omega_n \sum_{k=1}^{N_3+1} \omega_k \mathbf{N}^e(\xi_i, \eta_n, \gamma_k)^T \mathbf{N}^e(\xi_i, \eta_n, \gamma_k) \det(\mathbf{J}^e_{ink}), \quad (6.28)$$

$$\mathbf{K}^e = \int_{\Omega_e} \mathbf{B}^{eT} \mathbf{D}^e \mathbf{B}^e dv$$

$$= \sum_{i=1}^{N_1+1} \omega_i \sum_{n=1}^{N_2+1} \omega_n \sum_{k=1}^{N_3+1} \omega_k \mathbf{B}^e(\xi_i, \eta_n, \gamma_k)^T \mathbf{D}^e \mathbf{B}^e(\xi_i, \eta_n, \gamma_k) \det(\mathbf{J}^e_{ink}), \quad (6.29)$$

$$\bar{\mathbf{f}}^e_j = \int_{\Omega_e} \mathbf{N}^{eT} \bar{\mathbf{f}}^s_j dv$$

$$= \sum_{i=1}^{N_1+1} \omega_i \sum_{n=1}^{N_2+1} \omega_n \sum_{k=1}^{N_3+1} \omega_k \mathbf{N}^e(\xi_i, \eta_n, \gamma_k)^T \bar{\mathbf{f}}^s_j(\xi_i, \eta_n, \gamma_k) \det(\mathbf{J}^e_{ink}). \quad (6.30)$$

In the equations above, ω_i are the quadrature weights, N_1, N_2, and N_3 are respectively, the degree of polynomials in the directions of ξ, η, and γ. The results obtained in the wavelet domain have to be transformed back to the space of the approximation coefficients, and subsequently to real time, similar to the procedure outlined in Chapter 5.

A graphical implementation of the approach is shown in Figure 6.1. Each decoupled system of linear equations (SLEs) includes a different dynamic stiffness matrix as a linear combination of the mass, the damping and the stiffness matrices in accordance with Equation (6.26). To summarize the entire solution procedure, the following steps have to be taken to solve a problem.

Step 1: Computation of the approximation coefficients of the wavelet transform at the resolution level zero, in accordance with Equation (3.37).

Step 2: Computation of the connection coefficients for construction of matrices $\mathbf{\Lambda}_0$ and $\mathbf{\Lambda}_2$ in Equation (6.14).

Step 3: Finding the wavelet frequencies $\bar{\omega}_j$ in Equation (3.47), to be used in Equation (6.26).

Step 4: Transformation of the input functions, e.g. applied forces, using Equation (6.15).

Step 5: Construction of the finite element matrices $\mathbf{K}$, $\mathbf{M}$, and $\mathbf{C}$ in Equation (6.27).

Step 6: Formation of the dynamic stiffness matrix of Equation (6.26) at each wavelet point j.

Step 7: Solving the linear system of algebraic equations (6.26) for each wavelet point.

Step 8: Back-transformation to real time.

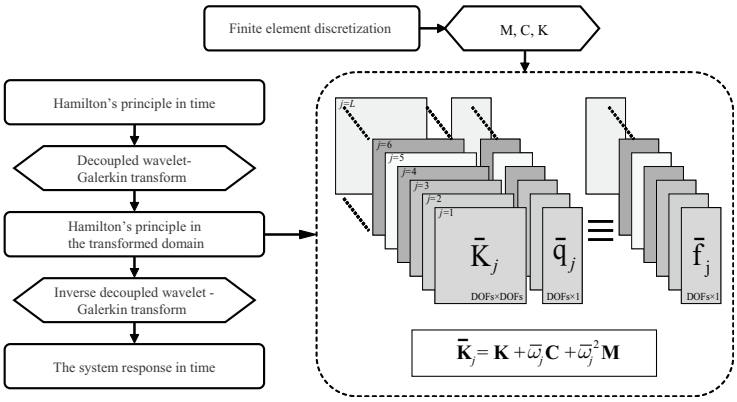

Figure 6.1: The wavelet-based spectral formulation of finite element methods. The spatial discretization can be performed using a finite element scheme, e.g. SEM. The resulting stiffness, mass, and damping matrices are fed into the wavelet-Galerkin based solver, which in essence, is responsible for the temporal discretization of the problem. For dealing with complex geometries, the finite element model can also be constructed in commercial software.

6.3 Some Remarks about the Wavelet-based Spectral Finite Element Method

In order to better understand the introduced wavelet-based spectral finite element method (WSFEM), some of its computational aspects are outlined in this section.

1. The WSFEM can be implemented in parallel, since there is no connection between the computations at different time steps[2]. The maximum speed-up factor which can be achieved using parallel computing can be estimated from Amdahl's law [Amdahl, 1967]. If there is no limitation on the number of available CPUs and the memory bandwidth for parallel computations, the limit speed-up factor will be equal to the reciprocal of the portion of the algorithm that cannot be parallelized[3]. In practical applications, the solution time may also depend on the size of the problem to be solved, the CPU(s) cache, the available memory size, and the memory type, see Appendix D.

2. Improved accuracy in the temporal discretization can be achieved by both

[2]In both explicit and implicit time-domain schemes, the time marching procedure makes the solution at each time step dependent on the solution at the previous step(s), and sometime current step, making the parallelization impractical.

[3]For example, assuming that the parallelizable portion of the problem is 90% the entire solution of the transient problem, the solution cannot be sped up more than 10 times, irrespective of the number of processing units.

increasing the number of sampling points, and increasing the wavelet order.

3. The temporal discretization is independent of the spatial discretization. In a typical elastic wave propagation problem, no more than few hundreds of temporal sampling points are usually required to capture the frequencies of interest within the time window of interest, i.e. shorter time windows for high frequency problems, and vice versa.

4. The transformation operators can be computed once and stored for large number of temporal sampling points, since the transformation operators are independent of the physical properties. As a rough estimation, the forward and the inverse projections for a few hundreds of sampling points take a normal processor a fraction of a second to compute.

5. Frequency-dependent damping models are, contrary to both implicit and explicit Newmark time integration schemes, straight-forward to apply in the WSFEM.

6. Unlike the frequency domain spectral methods, the WSFEM is free from additionally-imposed conditions such as periodicity. The results in the transformed domain can hence be accurately reconstructed in the time domain, as confirmed by the results in the next sections and also chapters 4 and 5.

7. Similar to the time domain methods, all finite element schemes currently-used for linear elasticity problems, e.g. SEM, NURBS-based FEM [Hughes et al., 2008], or finite element models from commercial software, can be adopted into the WSFEM formulation. This makes the approach flexible in dealing with various engineering applications.

8. The WSFEM, as a result of its spectral formulation, does not present significant numerical dispersion, see the numerical verification in Appendix C.

9. Similar to time-domain SEM, capturing surface waves does not require additional treatment in the formulation and the free surface boundary conditions are naturally imposed in the finite element formulation of the problem.

10. Non-zero initial conditions are not straight-forward to deal with. As discussed in Chapter 3 however, wave propagation problems in structural health monitoring (SHM) nearly always meet the zero initial conditions. In case initial conditions are not zero and important to consider, the methods mentioned in Section 3.4 may be applied.

11. The method is not suitable for nonlinear problems.

As a general remark, in the absence of parallel computation facilities, depending on the problem under investigation, the WSFEM may or may not be faster than the explicit Newmark scheme. This also strongly depends on the efficiency of the solution techniques employed for solving linear systems of equations schematically shown in Figure 6.1. Optimized techniques can speed up the WSFEM solution time. If, for example, SEM is utilized for spatial approximation, only the diagonal components of the dynamic stiffness matrix change at each wavelet point, hence, an appropriate factorization may substantially reduce the computational time of the WSFEM.

6.4 Validation: Lamb waves in an infinite aluminium plate

The developed WSFEM was validated through a number of numerical and analytical solutions of 1D, 2D and 3D problems. As an example, predictions of the present method for the benchmark problem in Ha and Chang [2010] are compared to the exact results. The problem of interest is the time domain simulation of the propagation of fundamental Lamb wave modes in an aluminum plate with thickness of 1 mm. The excitation force is a narrow-banded burst with central frequency of 50 kHz, applied as point load tangent to top free surface of the plate. Following Ha and Chang [2010], the plate dimensions are chosen sufficiently large so that the reflections from the edges do not appear in the time window of interest, i.e. 200 μs. In the WSFEM, the number of time samples was chosen as $L = 300$, the SEM order $N_x = N_y = 5$ and $N_z = 3$, where z is the direction perpendicular to the free surfaces of the plate. The result, which is the displacement component in the same direction as the point load, on the top surface, and 152.4 mm away from the source, can be observed in Figure 6.2 showing a good agreement with the analytical solution. The first wave packet in the time window shown is the fundamental symmetric mode S0, and the second envelope traveling at a lower speed is the fundamental antisymmetric mode. Note that the small discrepancy in the two plots, which was also observed by Ha and Chang [2010], may be attributed to the finite size of the model in the numerical simulation.

6.5 Case Study I: A 3D Aluminum Beam-like Structure

The accuracy and convergence properties of the WSFEM are discussed in this section. An aluminum bar with length, width, and thickness of 200, 20, and 1mm, respectively, is considered with the modulus of elasticity, Poisson's ratio and density of 70GPa, 0.3, and 2700kg/m^3, respectively. A schematic representation of the structure, loading, boundary conditions, and the global coordinate system is given in Figure 6.3.

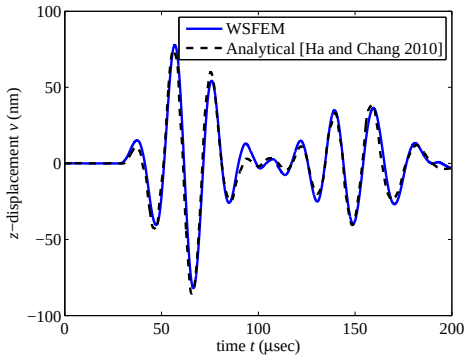

Figure 6.2: Comparison of the 3D WSFEM results with analytical results of Lamb waves generated by a point load on a free surface of a plate structure published by Ha and Chang [2010].

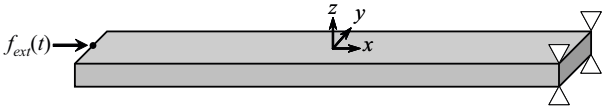

Figure 6.3: The sample 3D structure: the structure is clamped at four points in all degrees of freedom, and the external point load $f_{ext}(t)$ is applied in x-direction, as shown in the figure.

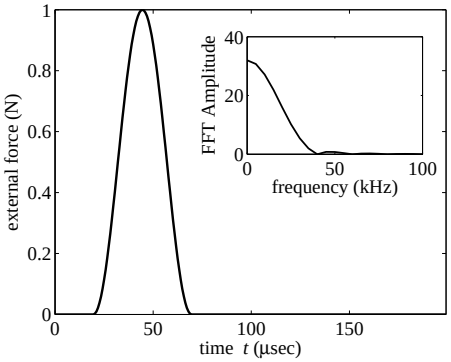

Figure 6.4: The loading function and its frequency spectrum: the duration of the pulse in the time domain is 50μs, and in the frequency domain nearly 50kHz.

At the excitation point located at the coordinate $(-100, 0, 0)$mm, the structure is subjected to a wide-banded load pulse, which is shown in Figure 6.4 along with its frequency transform. The signal has no major frequency beyond 50 KHz, and the simulation time is 200μs.

Since the problem is formulated in a transformed domain, it is of interest to observe what the inputs and outputs, i.e. forces and displacements, look like in the transformed domain. The transformed force, c.f. Equation (6.15), is plotted in Figure 6.5 for the wavelet order $N = 6$ and 128 temporal sampling points, i.e. $L = 128$. As mentioned earlier, the transformed force has both real and imaginary components. The larger amplitude of the transformed force at smaller wavelet points expresses the greater contribution of these wavelet points in the system response. It is also known that each wavelet point corresponds to a complex wavelet frequency. This correspondence, which is demonstrated in Figure 6.6, can facilitate physical interpretation of the solution procedure, as will be seen later in this section. As a general remark, the wavelet points numbering can be performed differently than that of shown in Figure 6.6; the wavelet frequencies can be viewed as the eigenvalues of some connection coefficient matrices which can be ordered in different ways, e.g. in an increasing or decreasing order. Hence, for interpretation of the results in the transformed domain, consideration of the wavelet point-wavelet frequency relation, e.g. Figure 6.6, is always necessary. Moreover, it can help the reader to make analogy with the Fourier frequency domain.

The accuracy of the WSFEM is evaluated by comparing the displacement response of the beam-like structure at the excitation point, to the SEM equipped with Newmark explicit time integration. In both methods, the structure is spatially discretized to $20 \times 2 \times 1$ spectral elements with basis functions of order 5 in x- and y-directions, and order 2 along z. The critical time step size of the ETI is about 0.06μs, equivalent to having 3332 time steps in the 200μs window of interest. To create a reference solution, the time step size in ETI is chosen

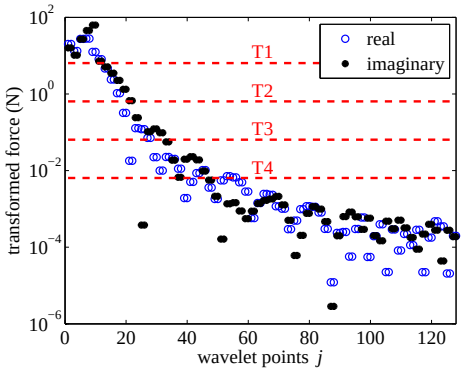

Figure 6.5: The transformed load in the wavelet domain, with real and imaginary components.

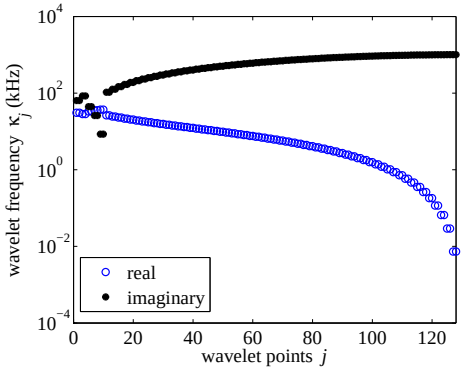

Figure 6.6: The wavelet frequencies versus wavelet points.

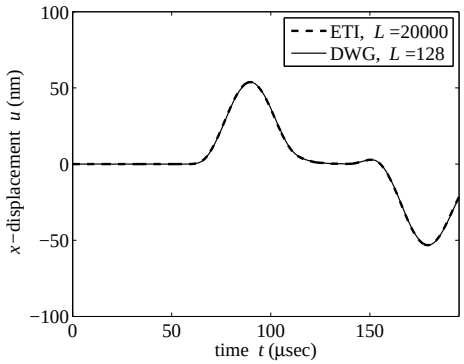

Figure 6.7: The displacement response of the waveguide in the length-wise direction.

as nearly 15% of its critical size. The displacement response of the structure in the x-direction at (100,0,0)mm denoted by u, is shown in Figure 6.7.

Excellent agreement between the two methods, the DWG-based scheme and ETI, can be observed in Figure 6.7. In the DWG with order 6, only 128 time samples are used. Depending on the desired sampling frequency, smaller values of L are still possible. In order to quantify the difference in the two responses shown, the root mean square (RMS) deviation is computed as:

$$\text{RMS} = \left(\frac{\int_0^{t_{end}} \left[u(t) - u_{ref}(t) \right]^2 dt}{\int_0^{t_{end}} \left[u_{ref}(t) \right]^2 dt} \right)^{\frac{1}{2}} . \tag{6.31}$$

In the example shown (Figure 6.7), the RMS deviation of the WSFEM from the reference solution is 0.0012, i.e. almost identical to the reference solution, as the similarity is equal to 1-RMS, i.e. the responses are 99.88% similar. Note that the integrals in Equation (6.31) were computed numerically using the trapezoidal rule.

The convergence of the DWG-based SEM was evaluated, and for each discretization scheme, the deviation of the response from the reference solution was computed in the RMS sense. A similar analysis on the same spatial grid was also performed for ETI, and the results are shown in Figure 6.8.

Superior convergence of the DWG-based SEM can be observed in Figure 6.8. The solution parameters are similar to the previous example. Unlike the DWG, the ETI suffers from conditional stability, thus, the ETI-based solution diverges if the time step size is larger than 1μs. The difference in the required number of sampling points between the DWG and the ETI becomes drastic for fine meshes as shown in Figure 6.9. This can make the present formulation of the WSFEM advantageous for larger numbers of degrees of freedom. Note that the FE mesh in Figure 6.9 is uniformly refined, i.e. the aspect ratio of the elements is kept constant in the mesh refinement process.

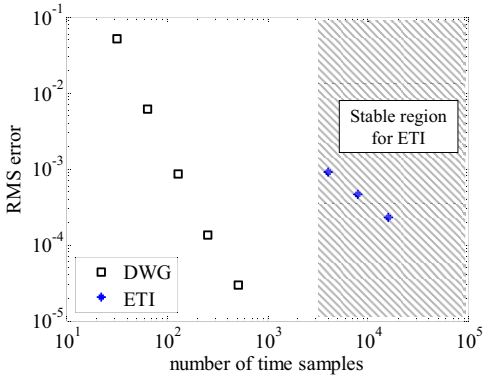

Figure 6.8: Comparison of the convergence rates of the DWG-based SEM and the ETI-based SEM. The ETI has conditional stability. The stable region of ETI is hatched in the figure.

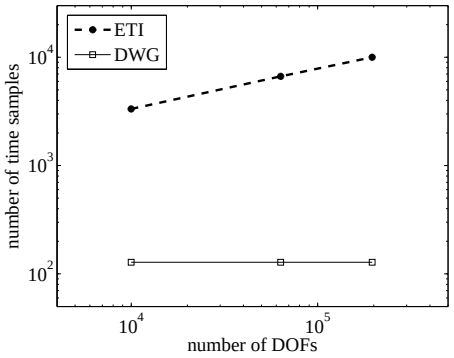

Figure 6.9: Comparison of the number of sampling points in the DWG-based SEM and the ETI-based SEM. The temporal discretization in the DWG, contrary to the ETI, is independent of the spatial discretization.

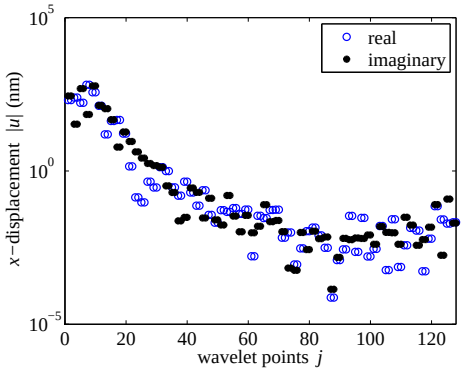

Figure 6.10: The real and imaginary components of the transformed displacement response in the length-wise direction. The displacement amplitudes are in agreement with the transformed applied force amplitudes in Figure 6.5.

The transformed-domain displacement response of the structure in the x-direction at (100,0,0)mm for L=128 is demonstrated in Figure 6.10. As expected, the response in the transformed domain is complex. The imaginary component of the response however, vanishes when it is transformed back to time (Figure 6.7), i.e. the inverse DWG weights the transformed-domain responses in such a way that the imaginary components cancel out, and create a real-valued response in time.

To better illustrate the transformed-domain response, three wavelet points 0, 64, and 127 are considered (L=128). The displacement of the upper surface of the structure in the y-directions denoted by v, is plotted in Figure 6.11. The magnitudes of the real and imaginary components are shown separately. It can be clearly seen that at the first wavelet point, i.e. $j = 0$, the structure present a low frequency response (Figure 6.11-a). A higher frequency response is captured at $j = 64$, as shown in Figure 6.11-b. By looking at the amplitudes however, this response does not seem to contribute as much as the response at $j = 0$ in the time-domain solution. At the last wavelet point, i.e. $j = 127$, the response is completely dominated by smaller wavelengths corresponding to the highest frequency which is captured by the considered discretization (Figure 6.11-c). It will be shown later in this section that elimination of the responses at the wavelet points 64 and 127 in the response reconstruction in time does not visibly influence the results.

The reconstructed time-domain response can be obtained by certain reshuffling of the solutions in the transformed domain, i.e. a weighted superposition in accordance with the DWG. The reconstructed response at 46.8μs and 156μs are demonstrated in Figure 6.12. Similar to the previous example, the contour plots show the magnitude of the displacement of the top surface of the structure in the x- and y-directions. Due to the relatively high frequency content of the excitation pulse, elastic waves propagate throughout the structure.

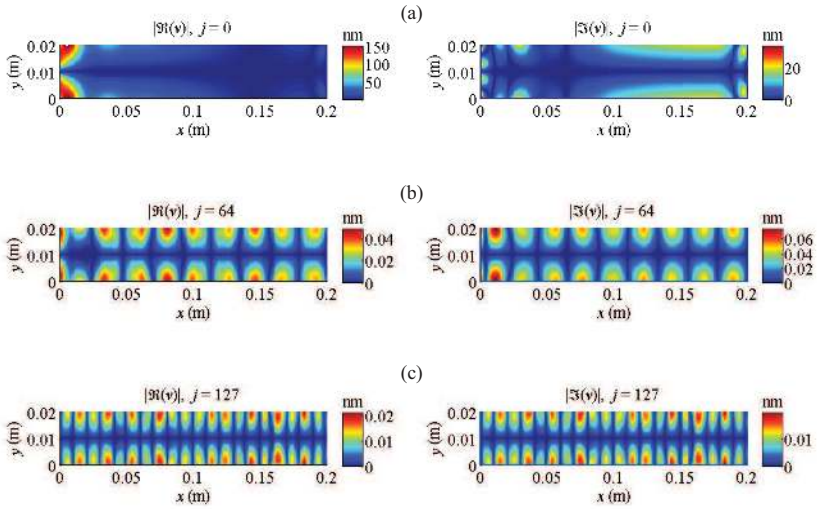

Figure 6.11: The transformed displacement response at the upper surface at three wavelet points; (a) $j = 0$, (b) $j = 64$, and (c) $j = 127$.

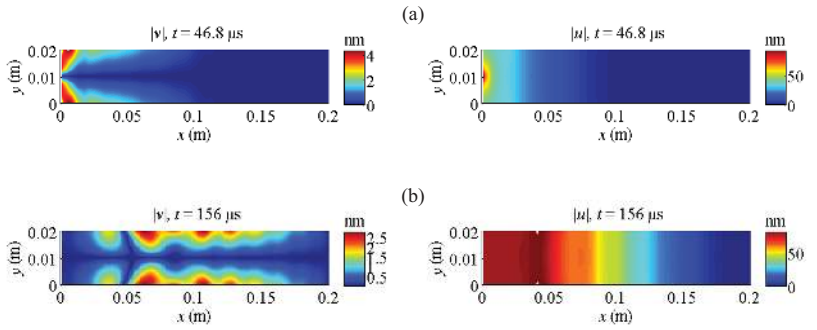

Figure 6.12: The time-domain displacement response at the upper surface; (a) $t = 46.8\mu$s, and (b) $t = 156\mu$s.

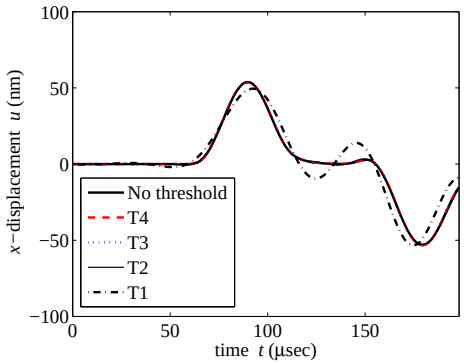

Figure 6.13: Effect of thresholding. The thresholding is based on neglecting the response at the wavelet points in which the transformed applied force has no major component, c.f. Figure 6.5.

The question to be answered yet is that how many of the responses in the transformed domain are required for reconstruction of the response in time, since the contribution of the responses does not appear to be equal. Using a thresholding scheme, the influence of the responses with small amplitudes in the response reconstruction is studied. As shown in Figure 6.5, four different threshold levels (T1 to T4) are considered for the transformed input load. Contribution of the responses at the wavelet points (wavelet frequencies) the transformed load component of which is below the threshold limit is thus neglected. This means that only a subset of the equations shown in Figure 6.1 need to be solved, while the rest of the responses are formally set to zero. This investigation is demonstrated in Figure 6.13.

According to Figure 6.13, the thresholding can save a substantial computational power by reducing the number of equations to be solved. Using threshold levels T4 and T3, which result in solving nearly 40% and 30% of the entire 128 SLEs respectively, the reconstructed solution reproduces the solution of the full system perfectly. Threshold level T2 however, which solves approximately 20% of the SLEs, undergoes minor deviations from the full solution. This is certainly a substantial saving as such a transient problem is solved at only 24 points. By further reducing the solution points in number, the threshold T1 filters out some important information about the system and hence, results in an imperfect reconstruction of the response in time. It has to be noted that the choice of an appropriate threshold is a subjective task and needs to be done in accordance with the structural properties, loading conditions, maximum frequency to be captured, and the desired accuracy.

6.6 Possible Techniques for Speeding up the Procedure

In addition to the use of thresholding, with which a substantial savings in the computational power can be achieved, certain techniques may be adopted to reduce the computational time of the WSFEM. In the presented approach based on SEM for spatial discretization, since the mass matrix is diagonal, by means of a fixed reordering of the dynamic stiffness matrix at all solution steps, c.f. Equation (6.26), using column count, or minimum degree methods [Strang, 2007], the solution can be made faster to some extent. It is however, believed that considerable computational time can be still saved in the WSFEM, if the dynamic stiffness matrix at each step is factorized effectively as the summation of a fixed positive definite stiffness matrix $\mathbf{K}$ and a fixed diagonal mass matrix $\mathbf{M}$, according to Equation (6.26). This study however, is beyond the scope of this dissertation due to time constraints. Note that in any case, the solution time of the WSFEM is inversely proportional to the number of available parallel processors, excluding the data transfer time.

Even in the absence of parallel computation facilities, since the presented method is essentially different from the explicit Newmark time integration, no general conclusion can be drawn on the total simulation time without considering all influential solution parameters in the two schemes. For special cases such as structures having frequency-independent proportional damping with $\bar{\beta}_j = 0$, c.f. Equation (6.27), since the mass matrix of SEM is diagonal, the solution at each time step is very efficient in the ETI. In more general cases however, such as frequency dependent damping models in which the damping matrix is a linear combination of the mass and the stiffness matrices, the ETI requires to factorize a matrix being as sparse as the stiffness matrix, at each time step. Since the solution at each step takes exactly the same time in the ETI and the DWG, the latter that needs substantially fewer number of sampling points is preferable even in the absence of parallel computation facilities. Also for structures having a very large number of degrees of freedom, storing the factorized matrices for ETI may not be justified and iterative solutions may have to be employed. In this scenario also, the presented formulation is inherently advantageous.

6.7 Case Study II: A Multilayer Composite Structure

The next case study is devoted to 3D simulation of wave propagation in a thick composite plate. The specimen was a graphite epoxy panel as shown in Figure 6.14, with the ply stacking sequence $[0_4, 90_4, 90_4, 0_4]$ with 0° in the x-direction, and length, width and thickness of 200mm, 200mm, and 4mm, respectively. The material properties were as given in Section 2.2.3. At point M located at the mid-point of the top surface, the plate was subjected to two point loads with the profile shown in Figure 5.4-b, along x- and z-directions. The structure was

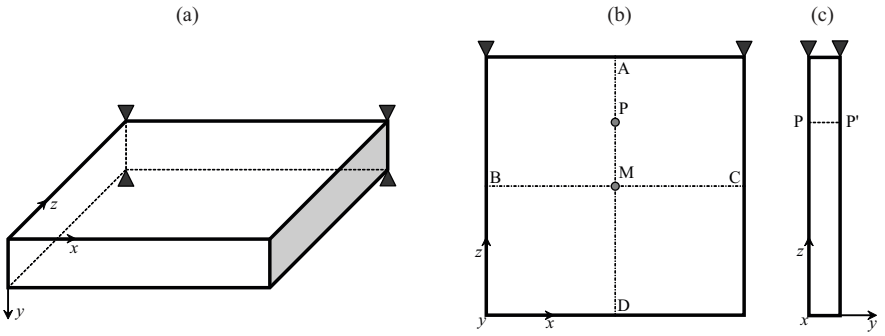

Figure 6.14: The model of the composite plate: (a) the 3D view and the coordinate system, (b) the view of the top surface of the plate, and (c) the left view of the specimen.

constrained at 4 points in all translational degrees of freedom along x, y, and z, respectively denoted by u, v, and w. The total simulation time was 150μs and discretized at 50 points, i.e. $L = 50$. For the temporal discretization, the wavelet-Galerkin method with the Daubechies wavelet order $N = 6$ was utilized.

For the spatial discretization, SEM was employed. The thickness-wise direction y of the plate, which is composed of four homogenous regions of 0 or 90° fibers, was discretized into 4 sub-domains with interpolation order $N_y = 3$. The $x - z$ plane was also discretized into 6×6 subdomains each of which having interpolation order $N_x = N_z = 5$. As a results, the finite element model was constructed with $6 \times 4 \times 6 = 144$ 3D SEM elements each of which had 144 nodes, and each node had 3 DOFs. The selection of the current mesh is based on considering at least 6 nodes per wavelength of the SH0 waves in the waveguide, at 50kHz as the upper limit of the driving frequency[4].

The displacement response components, i.e. u, v, and w, of the structure at points A, B, C, and D, as the mid-points of the edges of the top surface of the plate, is illustrated in Figure 6.15. The components of the displacement u and w appear to be dominated by the fundamental P, i.e. S0, and the fundamental SH waves, i.e. SH0, whereas v takes place mostly as a result of the propagation of the fundamental shear vertical waves, i.e. A0. For example, the displacement components u at point A and w at point B indicate that SH0 waves are the dominant waves received at these points. From the component u at point B and w at point A, dominance of the S0 waves can be observed. Note that the group speed curves for the Lamb wave modes for this analysis can be extracted from the formulation presented in Chapter 2.

The through-the-thickness distribution of the displacement field at the loca-

[4]Although the wavelength of A0 waves is generally smaller than the wavelength of SH0 waves and hence, should be the basis of the calculations for the minimum number of grid points per wavelength, the response to the used wide-banded excitation is dominated by the lower frequency components having larger wavelengths.

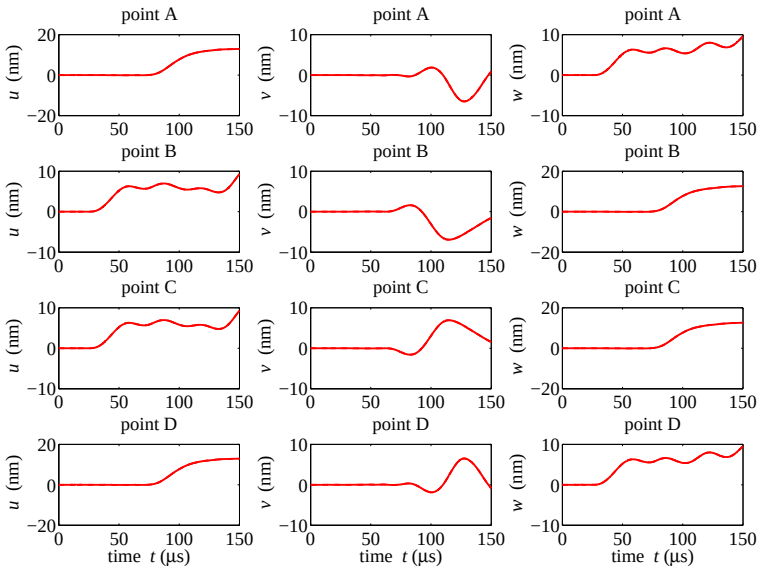

Figure 6.15: The displacement response of the composite plate at points A, B, C, and D as the mid-points of the edges of the top surface of the plate, see Figure 6.14.

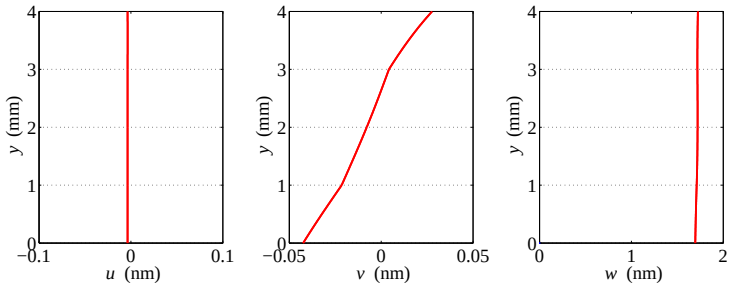

Figure 6.16: Distribution of the displacement components of the composite plate along the trajectory P-P′ (see Figure 6.14) at time 33μs.

tion P-P′ is demonstrated in Figure 6.16. Some facts can be extracted from the shown plots. The symmetry of w at $t = 33\mu$s reveals that the fundamental P waves, i.e. S0, have reached point P before this time. The displacement component u however, was very small, meaning that the SH waves, which have a lower group speed, either did not arrive yet, or just arrived. The antisymmetry of the displacement component v shows that the plate contracts in the thickness-wise direction. This happens since the laminate is relatively thick, which makes the product of the laminate thickness and excitation frequency fairly large and further activates the thickness contraction mode. The discussions in Chapter 4 of this dissertation can facilitate interpretation of identification of these effects from the displacement field obtained.

The resulting stress and strain fields at any arbitrary time can be recovered from the formulations. Once the nodal displacements are obtained at an arbitrary instant, the strain values at the element level denoted by $\boldsymbol{\epsilon}^e$ can be directly computed from:

$$\boldsymbol{\epsilon}\left(\Omega_e\right) = \mathbf{B}^e\left(\Omega_e\right)\mathbf{q}^e, \tag{6.32}$$

where $\mathbf{B}^e$ is given in Equation (6.25). At $t = 33\mu$s, the strain field was computed at point P, as illustrated in Figure 6.17. As a consequence of the C^0 continuity of the through-the-thickness displacement distribution due to inhomogeneity in $y-$direction, some strain components, e.g. ϵ_y, are discontinuous. For further insight into the through-the-thickness effects, the stress field was also obtained as shown in Figure 6.17. The stress field can be readily retrieved from the strain field using the constitutive matrix $\mathbf{C}$.

By looking at the stress distribution, it can be observed that at $t = 33\mu$s, both of the two existing modes passing through the trajectory P-P′ were fundamental symmetric ones, the dominant mode of which was the S0 wave characterized by σ_z. The SH0 waves, which were characterized by σ_{xz}, were not zero, but had small values, thus just arrived.

Similar studies were performed next for $t = 58\mu$s. The displacement field, which is demonstrated in Figure 6.19, showed that at this instant, the SH waves characterized by the displacement component u appear in their fundamental

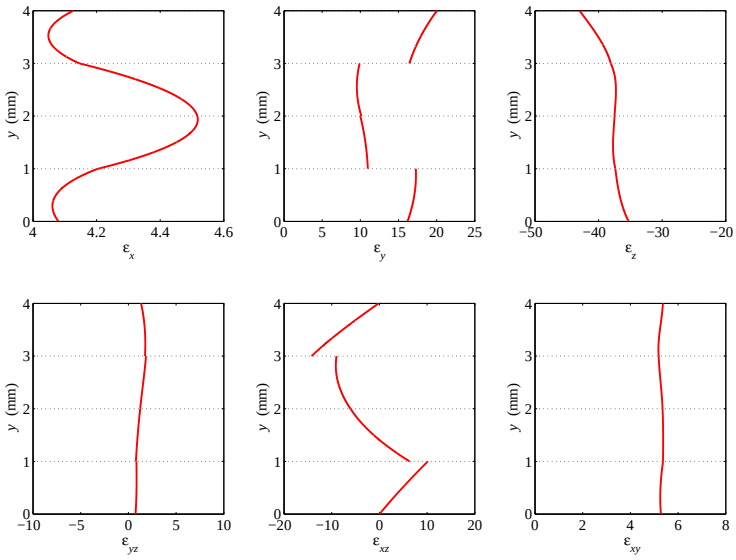

Figure 6.17: Distribution of the strain components of the composite plate along the trajectory P-P′ (see Figure 6.14) at time 33μs. All the units are nm/m.

symmetric mode. The displacement component w however, illuminated a combination of the fundamental symmetric, i.e. S0, and the fundamental antisymmetric, i.e. A0, modes. At time $t = 58\mu$s, no significant contraction effect was observed from the displacement component v.

In the strain field at $t = 58\mu$s shown in Figure 6.20, there were significant changes compared to the strain field at $t = 33\mu$s. The most important ones were the growth of the shear strains ϵ_{xz} and ϵ_{xy}, which lead to increase in the corresponding shear stresses. This can be seen in Figure 6.20, in which the stress distribution at $t = 58\mu$s along P-P′ is demonstrated.

From the distribution of stress at $t = 58\mu$s, it can be observed that the dominant mode was antisymmetric, which was characterized by σ_z. The other propagating antisymmetric mode is a shear horizontal wave, i.e. SH1, associated with σ_{xz}. In addition to these two modes, there are two symmetric modes characterized by the stress components σ_{yz} and σ_{xy}.

Although not studied in this chapter, a delamination changes the stress distribution in a composite structure, which depending on its severity and the type of the diagnostic waves, may act as an obstacle reflecting a part of the incoming wave packet. Study of the behavior of composite materials as waveguides in ultrasonic regimes can improve interpretation of the reflected and refracted waves for identification of the extent, and the through-the-thickness positioning of delaminations.

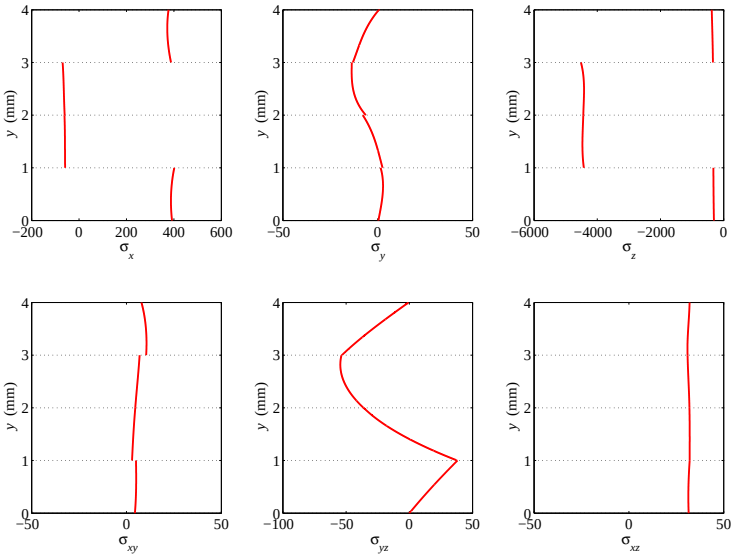

Figure 6.18: Distribution of the stress components of the composite plate along the trajectory P-P′ (see Figure 6.14) at time 33μs. The symmetric and anti-symmetric waves can be distinguished in the figure.

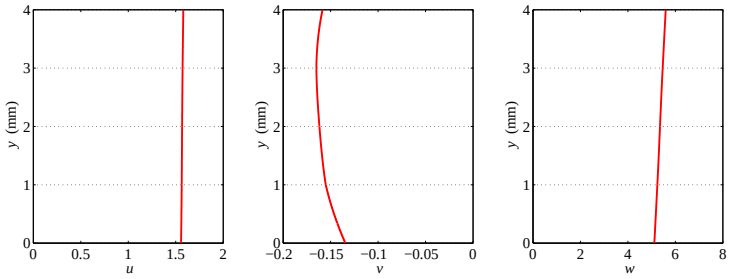

Figure 6.19: Distribution of the displacement components of the composite plate along the trajectory P-P′ (see Figure 6.14) at time 58μs.

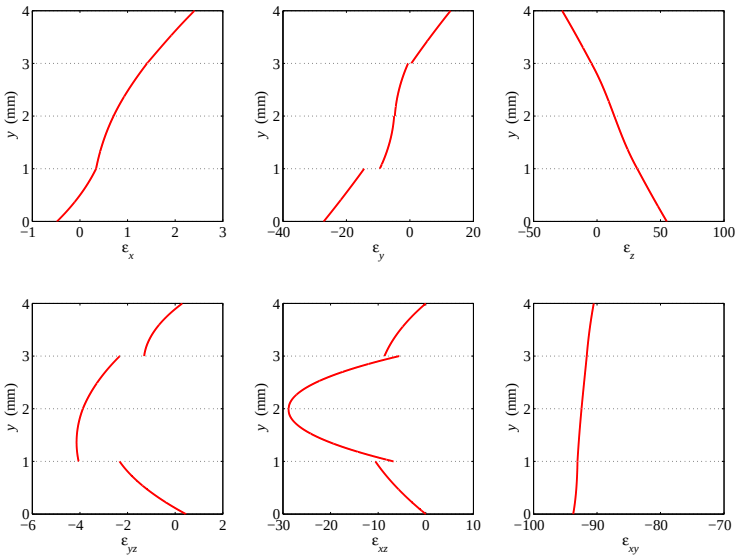

Figure 6.20: Distribution of the strain components of the composite plate along the trajectory P-P′ (see Figure 6.14) at time 58μs. All the units are nm/m.

6.8 Concluding Remarks

The generalization of the wavelet-based spectral formulation of the finite element method for 3D elastic wave propagation problems was demonstrated. The approach combines the standard finite element method for spatial discretization of the governing wave equations, with a wavelet-based spectral analysis for the temporal discretization, on the basis of their complementary merits. By employing the wavelet-Galerkin method, the variational principle of virtual work was temporally discretized and expressed in a transformed domain. The variational problem was further reduced to a set of temporally independent problems, which can be solved in parallel. A higher-order pseudo-spectral finite element method, i.e. spectral element method (SEM), with hp-refinement capabilities was adopted for the spatial discretization to achieve the possibility of dealing with complex 3D geometries, anisotropy, and heterogeneity. The numerical investigations carried out suggest that the approach is stable with respect to the temporal discretization, and the temporal sampling rate is hence, only dependent on the highest frequency of interest to be captured. Through 3D numerical examples, the functionality of the approach was studied. Also the superior convergence properties of the WSFEM were shown. Possible approaches for improving the solution time of the WSFEM were also discussed.

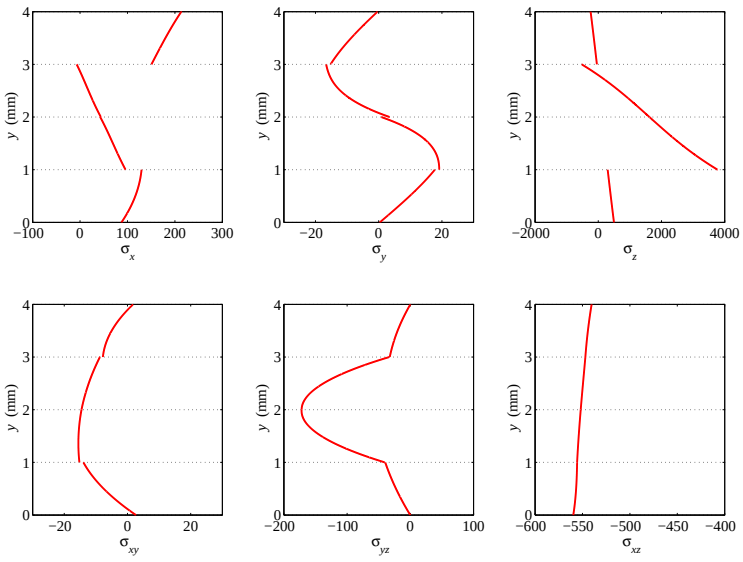

Figure 6.21: Distribution of the stress components of the composite plate along the trajectory P-P′ (see Figure 6.14) at time 58μs. The symmetric and anti-symmetric waves can be distinguished in the figure.

Chapter 7

SHM Based on Guided Ultrasonic Waves

In chapters 2 to 6, some analytical and numerical tools for understanding the underlying physics, and simulation of wave propagation in thin-walled structures were developed. The key question however, has not yet been answered: how can one use this knowledge in an autonomous fashion to monitor structural integrity?

As discussed in Chapter 1, every structural health monitoring (SHM) system is composed of a number of major components including the hardware, signal processing tools, forward modeling, and inverse solution. Intensive research has been carried out on these issues, see for example Inman et al. [2004], Staszewski et al. [2004], Balageas et al. [2006], Giurgiutiu [2008] and Boller et al. [2009]. A concise review of the commonly-employed SHM methods was provided in Chapter 1, and ultrasonic wave propagation-based SHM was selected for the applications of interest. Forward modeling was investigated in detail in chapters 2 to 6, by providing background knowledge about structures as waveguides and propagation of ultrasonic waves in structures, along with improved techniques for simulation of elastic wave propagation in 1D, 2D, and 3D metallic and composite structures.

An exploration of the relation between the above-mentioned components in wave propagation-based SHM approaches, and some of their challenging aspects are discussed in the present chapter. A number of signal processing tools for feature extraction, denoising, and signal windowing, which are generally required for SHM approaches and are used in the subsequent sections of this chapter, are briefly outlined. Next, SHM is discussed as an intrinsically ill-posed problem, and some major challenges in implementation of a SHM system are highlighted. To avoid dealing with SHM as an inverse problem with stability and uniqueness issues, the time reversal (TR) approach developed by Fink [1992] is introduced. The TR approach is a focusing technique for detection of disturbance sources in ultrasonic wave fields. The TR method is implemented in a passive model-

based fashion to construct a baseline-free framework, which is, contrary to most conventional SHM methods as discussed in Chapter 1, robust against changes in the environmental and operational conditions. The passive TR has limitations in dealing with non-local defects, or the damage types which do not cause significant structural discontinuity, e.g. corrosion. Such limitations however, do not apply to most typical damage types in composite materials, e.g. delamination, as they are intrinsically discontinuities in the waveguide and often localized in nature.

Possible applications of the TR in SHM are discussed next, and a roadmap for implementation of a TR-based SHM approach for practical applications is drawn. The chapter ends with two case studies that are used to demonstrate the outlined TR approach and the use of the signal processing tools. The fist case study deals with the load source identification in a real composite plate. The second example is devoted to delamination identification in a composite beam the response of which is simulated using the 3D wavelet-based spectral finite element method (WSFEM) formulated in Chapter 6. The TR-based approach, the concept of which is schematically illustrated in Figure 7.1, performs successfully in both cases, and detects the location of the external load and the defect with an acceptable accuracy.

7.1 Signal Processing for Feature Extraction and Denoising

Before implementing a SHM system, the major components that are not addressed in the previous chapters of this dissertation, need to be introduced. Signal processing, as mentioned earlier in this chapter, is one of the substantial elements of SHM systems. In GUW-based SHM, the diagnostic waves propagating through a structure carry information about the structural integrity. These signals are, when reordered at a specific sensor location, mostly in the form of one-dimensional arrays. One needs somehow to translate these arrays, in order to extract physically-sound information for SHM. In case where damage exists for instance, proper algorithms may be required to remove noise, capture the scattered and reflected wave packets, compute the arrival time, i.e. time of flight (TOF)[1], extract the amplitudes, and find the possible phase shift for detection of the damage fingerprint [Staszewski et al., 2004]. This process is generally

[1]Various techniques exist to calculate the TOF of a wave envelop, such as the signal energy-based onset time picking [Moll et al., 2010], the threshold-based double peak technique [Seydel and Chang, 2001], the cross-correlation between the actuator and the sensor signals [Seale et al., 1998], and time-frequency methods [Staszewski et al., 2004]. Among these methods, the cross-correlation seems to be the most extensively-used technique. The cross-correlation of two 1D arrays f and g is defined as:

$$(f \star g)[n] = \sum_{m=-\infty}^{\infty} f^*[m]g[n+m]$$

where n is the lag, and * denotes the complex conjugate.

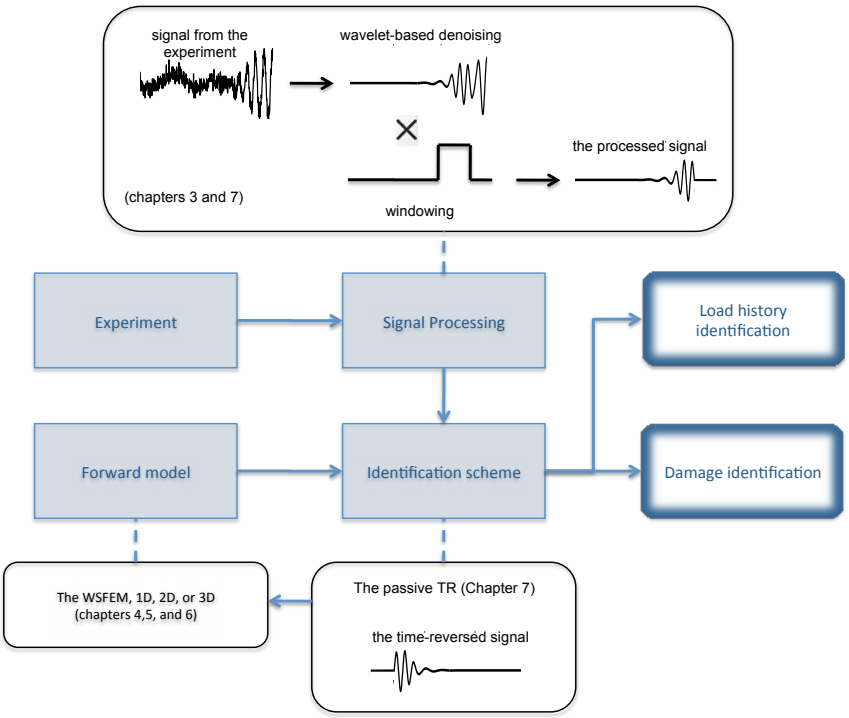

Figure 7.1: The flowchart of the TR-based approach. The signals gathered from the hardware are processed, i.e. denoised and windowed, time-reversed, and fed into a simulation tool. As demonstrated in this chapter, the transmitted time-reversed waves focus on the discontinuity, e.g. damage, location.

referred to as feature extraction. Since the focus of this research is mainly on identifying the location of possible defects, for more information regarding the features used in estimation of the damage type and severity, the reader is refered to Staszewski et al. [2004] and Boller et al. [2009].

To determine the location of localized defects in homogeneous and isotropic waveguides, e.g. fatigue cracks, after removing the unwanted features from the signals, a triangulation scheme is often employed. In the triangulation process, the arrival time of reflected wave packets can be readily mapped onto a distance space by using the dispersion curves of the waveguide, to determine the location of a structural discontinuity. The amplitudes of the wave packet together with the phase shift may provide information about the damage type and severity, when compared to a numerically- or experimentally-constructed damage fingerprint. In anisotropic waveguides, as demonstrated in Chapter 2, the wave-fronts are generally not circular, and the waves are mainly dragged in the direction of the fibers. In an extreme case where the structure is non-homogeneous and anisotropic, e.g. advanced composite structures, the propagation speeds and frontiers may also change throughout the structure, making the traditional triangulation-based methods inefficient in finding the defects.

7.1.1 Multiresolution Wavelet Analysis for Signal Denoising

Another significant application of signal processing in SHM is in signal denoising. Irrespective of the SHM method used, signals gathered from experiments are contaminated with noise. The noise due to the test hardware, environmental conditions, imperfect boundary conditions, not-exactly-known material and structural properties, etc., is usually mingled with the structural integrity information carried by the guided waves. Among several denoising algorithms developed over the past decades, the wavelets multiresolution scheme has garnered significant attention in the SHM community [Rizzo and di Scalea, 2006a, Staszewski et al., 2004, Giurgiutiu, 2008, Abbate et al., 1997]. The wavelets MRA the theory and features of which was presented in Chapter 3, will be used in this dissertation for noise removal purposes.

To eliminate the noise at the desired frequency band, standard operations of thresholding and pruning are utilized in the wavelets multiresolution analysis, [Rizzo et al., 2005]. As explained in Chapter 3, the discrete wavelet transform represents the signal at different frequency bands, see Figure 3.1 and Equation 3.18. Pruning refers to the direct removal of unwanted frequency bands from the signal, by setting the detail coefficients at the corresponding resolution levels, i.e. frequency band, to zero, i.e.:

$$Pr_j\left(f,m\right)=\sum_k c_{j,k}\varphi_{j,k}+\sum_{i=m}\sum_k d_{i,k}\varphi_{i,k}\ \ ;\forall k\in\mathbb{Z}. \tag{7.1}$$

where $c_{j,k}$ and $d_{j,k}$ respectively denote the approximation coefficients and the detail coefficients of the wavelet transform at resolution level j, and m denotes

the pruning level(s). Note that Equation (7.1) has essentially been derived from Equation (3.18) in Chapter 3.

Pruning of a signal requires caution since some significant information may be discarded if it is misinterpreted as noise. Depending on the noise level and frequency, and also the frequencies of interest, different scales of wavelet decomposition may be required. For more elaborate discussions on this matter, the reader is referred to Rizzo and di Scalea [2006a].

Thresholding, as a complementary operation, deals with the elimination of some selected components in the wavelet transformed signal that pertain to noise. The basic assumption in thresholding is that at each wavelet resolution level, which is identified as a main frequency band, the detail coefficients smaller than a prescribed value represent noise, i.e.:

$$Tr\left(d_{j,n}, tr\right) = \begin{cases} 0 & if \quad d_{j,n} < tr \times \max\limits_{k \in Z}\left(d_{j,k}\right) \\ d_{j,n} & if \quad \text{otherwise} \end{cases} \tag{7.2}$$

where tr is the threshold level. The threshold values can be assigned independently to different resolution levels, i.e. frequency bands, to optimize the denoising scheme. In other words, at some frequency ranges of interest only the amplitudes larger than an acceptable signal-to-noise ratio are kept using thresholding while the other frequency bands are removed using pruning. It should be noted that optimization of the pruning and thresholding parameters is, to some extent, an empirical procedure and the optimum values may vary with working conditions, i.e. the type of the noise source(s) and the frequency spectrum of the noise. It is apparent that if the frequency range of the noise is completely unknown, all denosing schemes including the wavelet multiresolution analysis may remove some important information about the system or the possible defect.

7.1.2 Signal Windowing

The signals collected from the actual hardware carry information which may be only partially useful. For example, it is very difficult to interpret the wave packets, after interaction with the structure boundaries. It is therefore important to focus on a specific part of the signal under investigation, and eliminate the rest of the signal. A Gaussian multiplicative window is used in this dissertation, which is defined by:

$$W_g(t) = \begin{cases} 0 & \text{if} \quad t < t_1 - T_g \\ e^{-(t-t_1)^2/2\sigma^2} & \text{if} \quad t_1 - T_g \leq t < t_1 \\ 1 & \text{if} \quad t_1 \leq t < t_2 \\ e^{-(t-t_2)^2/2\sigma^2} & \text{if} \quad t_2 \leq t < t_2 + T_g \\ 0 & \text{if} \quad t > t_2 + T_g \end{cases} \tag{7.3}$$

where t_1 and t_2 are the beginning and the end time of the window, T_g is the length of the window transition, and σ is the coefficient controlling the width of

the Gauss function. Note that although a rectangle function can also be used for windowing, it may bring spike signals with a high frequency content that adversely affect the accuracy of the analysis.

7.2 SHM as an Inverse Problem

Structural health monitoring is intrinsically an inverse problem. Inverse methods in structural integrity evaluation combine a mathematical model of the structure and the measured data to update the model based on certain assumptions for the damage model [Friswell, 2007]. There are often challenges in dealing with inverse problems, since they are ill-posed in a general sense [Uhl, 2007]. In SHM, this issue is intensified by the limited temporal and spatial measurements gathered from the structure under evaluation. In other words, the structural response can, in practice, only be obtained at certain locations in which the sensors are installed, with a certain sampling rate determined by the type of the sensors and the data-acquisition system. Due to the dispersive, multimodal and direction-dependent nature of the GUW in an anisotropic thin-walled structure (discussed in Chapter 2), these signals are often very complicated to analyze and interpret using time-delay techniques.

If the SHM problem is interpreted as identification of a black-box, the response of which is known only to a limited number of inputs, the problem can be ill-posed, i.e. a solution may not exist, may not be unique, or may be unstable due to oversensitivity to noise. Appropriate strategies are required to cope with the ill-posedness in SHM problems. The inverse SHM problem can be treated as an optimization problem in which the structural properties at each spatial point are the design variables, and the discrepancy between the response at the sensor locations and the predicated model is to be minimized. Although employing regularization technique [Busby and Trujillo, 1997] may improve the solution, this is still not feasible within the SHM framework due to the required computation time and power. For a review of the inverse problem approaches exploited for structural damage detection so far, the reader is referred to Inoue et al. [2001].

In addition to the complexity of the optimization problem to be solved, an inverse problem approach makes the SHM scheme highly dependent on the baseline response. An investigation by Sohn [2007] revealed that baseline-dependent SHM cannot be reliably used in practical applications, unless the environmental and operational conditions, e.g. temperature and loading conditions, are explicitly accounted for in the SHM system. Apart from the added uncertainty and complexity, incorporation of these effects, even using low-order approximate models, can substantially increase the costs of making the computations.

Although not presented here, a baseline-dependent approach for identification of fatigue cracks in 1D metallic structures based on minimization of the differential response at the sensor locations was investigated during the present research. The investigations were performed for fixed environmental and loading conditions. Some results are demonstrated in Appendix E. As explained

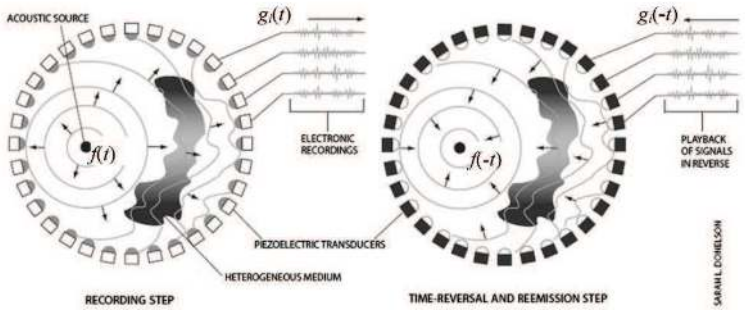

Figure 7.2: The TRM and the two operation steps of the TR scheme [Fink, 1999]. The left figure shows a source which emanates acoustic waves propagating throughout the cavity. The right figure shows that even in the presence of heterogeneity, the time reversed wave field focuses on the source.

above, the limited applications of the procedure to specific damage types, sensitivity to noise, and computational costs, however, led the researcher towards looking for a more efficient baseline-free technique based on the *time reversal* (TR) principle for more complex waveguides, e.g. multi-layered composites. Via this approach, the ill-conditioned nature of the wavefield inversion is converted into a well-conditioned forward problem by removing the determinism of the problem. The theory of TR accompanied by two case studies is explained in the following sections of this chapter.

7.3 Time Reversal of Ultrasonic Fields

The TR method introduced by Fink [1992] is a focusing method for sonic and ultrasonic targets in adiabatic processes[2]. The waves generated by an external disturbance propagate throughout an anisotropic non-homogenous waveguide at a spatially-varying speed. As intuitively shown in Figure 7.2, the TR method reverts the recorded wavefield in time, and the back-propagated field focuses on the disturbance sources. The TR method is capable of retracing multipaths [Fink, 1992, Chen and Yuan, 2010], and is hence appropriate for complex waveguides such as fiber-reinforced polymer structures.

To explain the theory of the TR, consider a linear heterogeneous anisotropic medium characterized by the equation of motion:

$$\mathfrak{L}\mathbf{u} + \mathcal{J}\ddot{\mathbf{u}} = \mathbf{0} \quad \text{in } \Omega \tag{7.4}$$

where $\mathfrak{L}$ is a spatial linear continuous differential operator that reflects the elastic properties of the medium, $\mathcal{J}$ is a matrix containing the inertial properties of

[2]An adiabatic process is a thermodynamic process in which the net heat transfer to or from the working material is zero. Such a process can occur if the system has thermally-insulated boundaries, or the process time is extremely short, so that there is no opportunity for significant heat exchange.

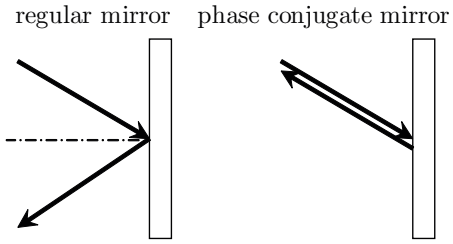

Figure 7.3: Regular mirror versus phase conjugate mirror: contrary to a regular mirror, a phase conjugate mirror only flips the chronological order of events.

the medium, Ω is the physical region of interest, and $\mathbf{u}$ denotes the vector of the dependent variables, e.g. displacements. The spatial operator $\mathfrak{L}$ satisfies the *spatial reciprocity*, meaning that interchanging the source and the receiver does not alter the resulting wavefields.

For the development of the TR theory, Fink [1992] took advantage of the special behavior of the linear lossless wavefields with respect to the temporal variable; the temporal operator contains only the second-order derivatives. The principle of the TR, i.e. *invariance under the time reversal*, states that if the dependent variables $\mathbf{u}(\mathbf{x}, t)$ with $\mathbf{x} \in \Omega$ being the spatial coordinate are the solution to the governing equations of a waveguide, $\mathbf{u}(\mathbf{x}, -t)$ also satisfies the equations.

The TR scheme can be viewed as an extended version of phase conjugate mirrors (PCMs) for monochromatic signals [Fink, 1992], in which the time reversal mirrors (TRMs) are placed at the sensors locations. As shown in Figure 7.3, a PCM, contrary to a regular mirror, only reverts the chronological order of events. When a number of PCMs are considered, based on the time invariance of the TR concept, the back-propagated wavefield converges to the source location, thereby recovering the disturbance.

7.4 Time Reversal-based SHM Systems

Two major approaches can be followed for SHM systems working based on the TR principle; *active time reversal* and the *passive time reversal*, as described below.

7.4.1 Active Time Reversal

The active time reversal approach employs both the time invariance and the spatial reciprocity characteristics of the TR by actually transmitting the time-reversed signals obtained by the sensors from the actuators. If the structure behaves linearly, the TR signals should look exactly the same as the original signal, i.e. the diagnostic wave packet. If damage has occurred however, the structure may start behaving non-linearly and hence, the time reversal principle

no longer holds. The existence of the damage in this scheme may hence be detected by studying the deviation of the output signal from the input signal.

It has to be noted that if one does not use spatial reciprocity, the time-reversed signals have to be transmitted from the sensor locations, instead of the actuator locations. The approach in this case is called *non-reciprocity-based time reversal*. The spatial reciprocity substantially facilitates implementation of the TR in a practical situation, since there is no need to switch the sensors and the actuators.

The active TR presents the advantages of having a straight-forward implementation, and being free from theoretical models; hence, it can be appealing for many practical applications in which the mathematical model of the specimen is difficult to construct. Besides these merits however, the studies by Gangadharan et al. [2009a,b] have shown that, if the damage does not break the time reversibility, e.g. a notch in a metallic plate, the TR-based damage detection deteriorates. The application of the active TR can hence, be limited by the following two major issues.

1. Since the maximum amplitudes in the displacement fields are very small, i.e. orders of magnitude smaller than the waveguide thickness, even the presence of damage may not lead to significant nonlinear behavior in the response.

2. The amplitudes of the signals are not always reliable for detection of possible damage, since the couplings between the sensors/actuators and the structure are never ideal and can change with environmental conditions.

In such cases, the output signal resembles the input signal but only with amplitude loss. In addition, such active TR-based SHM methods do not address the location of the damage, which in some applications, may be a crucial issue.

7.4.2 Passive Time Reversal

This passive TR is a model-based approach, the applications of which are growing rapidly in different areas [Ciampa and Meo, 2012, Wang and Yuan, 2009, Chen and Yuan, 2010, Mota et al., 2011]. In passive time reversal, the time-reversed recorded wavefield is not sent to actual hardware, but is fed to a numerical simulation tool. In accordance with the TR principle, the back-propagated waves focus on the source location(s) in the numerical simulation. The concept can be clearly understood from Figure 7.2. The passive TR, which does not use the spatial reciprocity property, is also regarded as a non-reciprocity-based approach. In comparison with the active TR, the passive TR has the advantage of being applicable to both linear and nonlinear systems. In addition, since the focusing of the time-reversed waves can also be captured by the simulation, a final image can be provided using the passive TR to pinpoint the disturbance sources, either active, i.e. external excitation or passive, i.e. reflective e.g. damage. Implementation of the passive TR however, requires reliable and computationally efficient tools to simulate the propagation of the ultrasonic waves.

Once the challenges of modeling anisotropic heterogeneous layered waveguides are understood, a passive TR can be a promising baseline-free tool for SHM of engineering structures.

The link between the previous chapters and the present chapter of this dissertation can be understood from the description of the passive TR provided above. On the basis of the merits of the passive TR, the methods developed in chapters 4, 5, and 6 for modeling wave propagation will be utilized in a passive TR scheme. The connection between the different processing steps of the approach was presented in Figure 7.1. It should be added that although the theory of the TR is well-established, there are still challenges in the practical implementation of the method, which need to be carefully dealt with. The rest of this chapter is devoted to addressing some of these issues by means of studying the external force localization and damage identification in composite structures.

7.4.3 Considerations in Using the Passive TR

The passive TR method, from a mathematical point of view, requires the wavefield to be recorded on an enclosed area, see Figure 7.2, and fulfil the sampling requirements to avoid aliasing. In many SHM applications, in particular for aerospace structures, fulfilment of this requirement is not feasible due to the associated hardware cost and weight. The consequence of not recording the complete wavefield can be (i) underestimation of the energy released from or reflected by the sources, and (ii) finding multiple solutions, i.e. multiple focusing points. The first issue arises from not incorporating the energy released by the source in all directions in the TR model. This issue however, may be addressed using a correction scheme in another phase subsequent to the source localization, provided that the amplitudes of the recordings are accurate. The correction scheme may find the actual amplitude at the source such that the error at the sensor locations is minimized.

The issue of multiple focusing points is expected to appear due to the presence of other structural discontinuities, accompanied by an inefficient positioning of the sensors. If there are additional structural discontinuities, e.g. free boundaries, the reflections from the discontinuities also interact in the time-reversed model and may lead to additional focusing points, that reflect no actual scattering source. In some applications, such issues may be alleviated to a large extent using an optimized layout for the sensors, and also using signal processing techniques to window out the wave packets bounced off the boundaries.

Another important limitation of the passive TR to note is finding continuous damage types, e.g. corrosion. The passive TR is only efficient in detection of localized effects, i.e. external forces and discontinuities, since it tends to map the recorded field to highly localized regions. This limitation however, is not an obstacle in utilizing the passive TR for SHM of composites as the typical damage types, e.g. delamination, are essentially structural discontinuities.

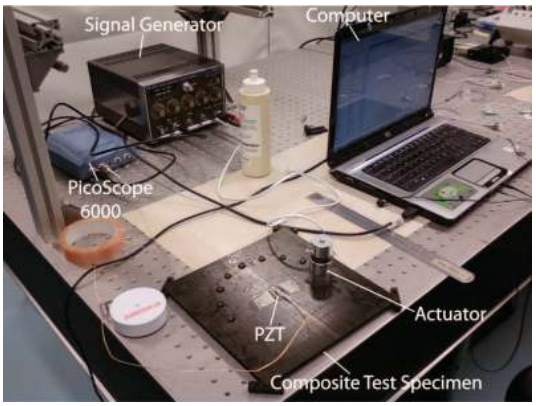

Figure 7.4: The hardware and the test setup [Melo Mota, 2011].

7.4.4 Case Study I: Source Identification Using Passive Time Reversal

In order to demonstrate the concept of the passive TR, and better illustrate the application of the presented components of a GUW-based SHM system in practice, a $200 \times 200 \times 1$ mm^3 graphite-epoxy panel with stacking sequence $[0/90/0/90]_s$ was tested in the lab. The results were subsequently used in the TR-based method, to identify the location of the applied external disturbance on the panel.

The specimen and the test apparatus which are shown in Figure 7.4 were the same as those discussed in Section 2.2.3. The structure was freely placed on four rubber supports at its corners, and thus regarded as not-clamped in the numerical model. One actuator denoted by a1, and three sensors s1, s2, and s3, were placed at the locations shown in Figure 7.5. In this experiment, a1 was a Honda Electronics actuator, and was connected to a signal generator to create a short pulse. The actuation mechanism is exerting a shearing force on the structure surface, hence, it predominantly generates the fundamental symmetric waves, as examined in Section 2.2.3. There was however, no control over the shape of the signal applied by a1 in this test, i.e. the loading history is unknown. Sensors s1, s2 and s3 were PICO HF-1.2 PZTs[3], and were connected to the surface of the plate using ultrasonic gel as couplant. A PicoScope 6000 was also used for data acquisition. More detailed information about the test setup and the verifications performed can be found in Melo Mota [2011].

It is known from chapters 2 and 6 that the wave-fronts in a non-isotropic waveguide are not circular. The unknown external load pulse, i.e. disturbance, generated by a1 in this experiment, thus, propagated at different speeds in different directions, and was recorded by the sensors. The signals gathered however, were contaminated with noise.

[3]Lead zirconate titanate material.

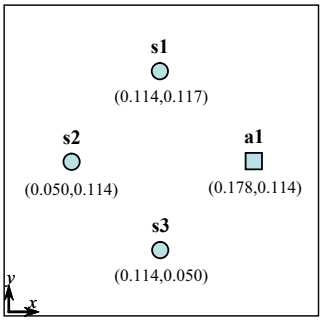

Figure 7.5: Configuration of the sensors and the actuator.

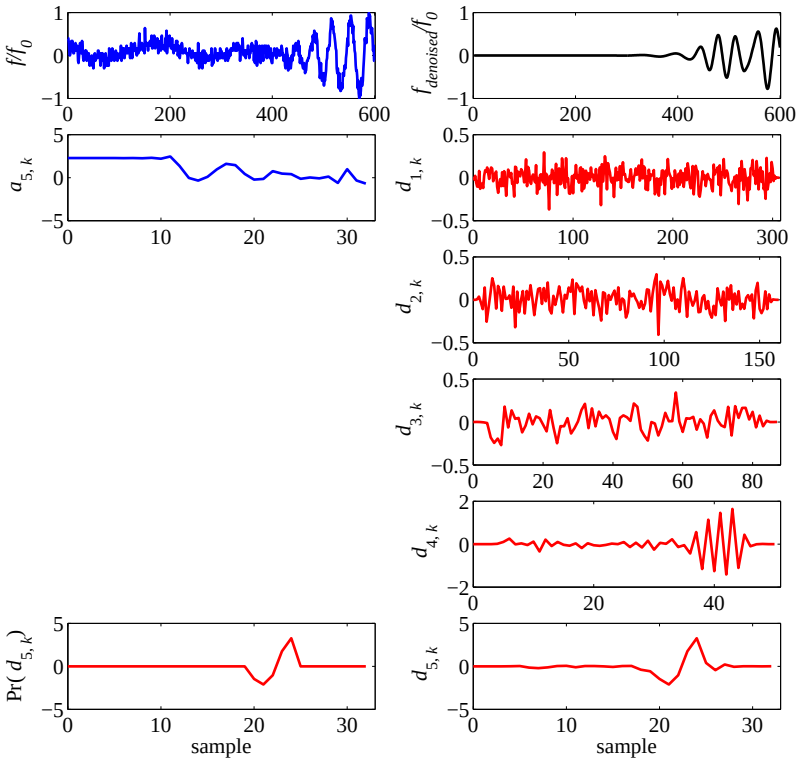

Figure 7.6: MRA for denoising the signal from sensor s1.

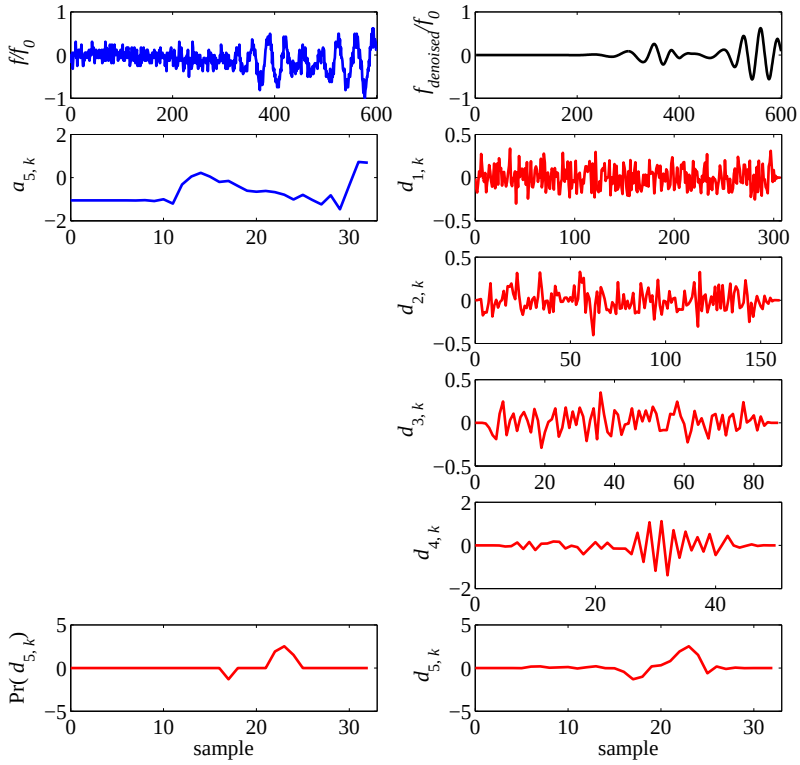

Figure 7.7: MRA for denoising the signal from sensor s2.

Using the wavelet MRA described in Section7.1.1, the normalized signals obtained by sensors s1, s2, and s3, were denoised as shown in figures 7.6, 7.7, and 7.8, respectively. In the denosing scheme, the pruning and the threshold levels are 5 and 0.25. This selection was to filter out very high and very low frequencies in the signals, which present noise and structural vibrations, respectively. Note that since the sensors were attached to the structure surface using ultrasonic gel, the amplitudes obtained by the sensors were not accurate, hence the signals were normalized and only the TOFs were considered.

The detail coefficients of the multiresolution wavelet analysis, i.e. d_k, j for $j = 1$ to 5 are demonstrated in figures 7.6, 7.7, and 7.8. Based on the discussions in Section 7.1.1, only the detail coefficients at the resolution level 5 were kept in this example. From these coefficients, the thresholding discarded the ones which were smaller than 25% of the maximum value of $d_{5,k}$. The signal reconstruction is thus performed using the remaining detail coefficients, i.e. $\Pr(d_{5,k})$, together with the approximation coefficients $a_{5,k}$. In figures 7.6, 7.7, and 7.8,

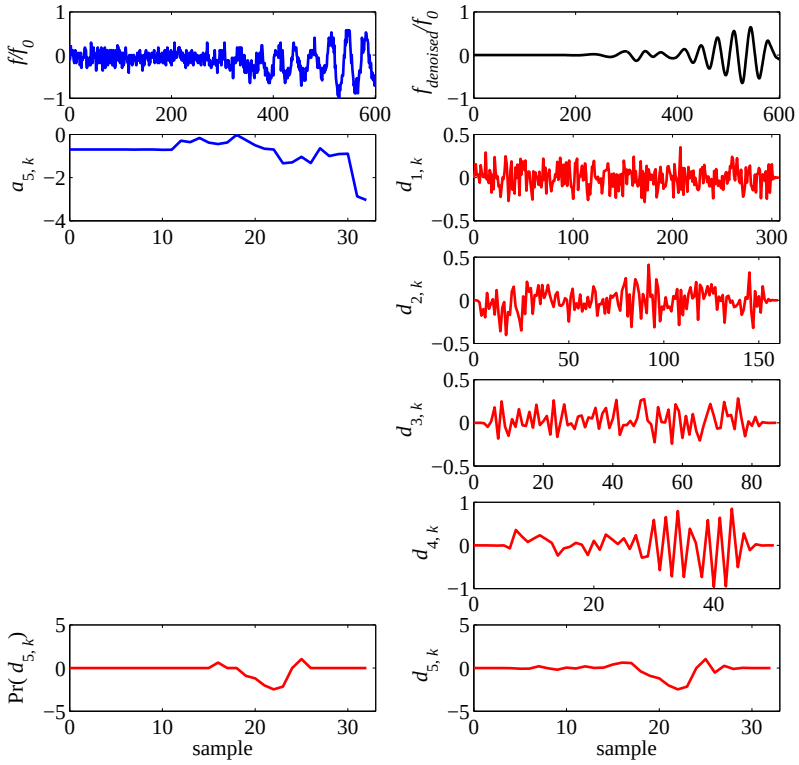

Figure 7.8: MRA for denoising the signal from sensor s3.

the normalized signal is denoted by f/f_0, and the denoised normalized signal is denoted by $f_{denoised}/f_0$.

The signals were expected to be sensed by s1 and s3 at about the same time, according to the geometry of the plate and the placement of the sensors. It appears from Figure 7.8 however, that s3 is influenced by some unknown source of noise such that even after denoising, there is a wave packet around the sampling point 250. This will be effectively dealt with in the windowing process later in this section. The fact that sensor s2, although it is further from the source, receives the signal earlier than s1 and s3 originates from the anisotropy of the laminate. As demonstrated in Section 2.2.3, the largest propagation speed of the fundamental symmetric waves occurs along the direction of the fibers, i.e. 0 or 90° in this case, depending on the ply. This will be seen later in this section when the passive TR scheme is applied.

The denoised signals at each sensor location were subsequently windowed. The beginning of the time window for all three sensors was the same, as it

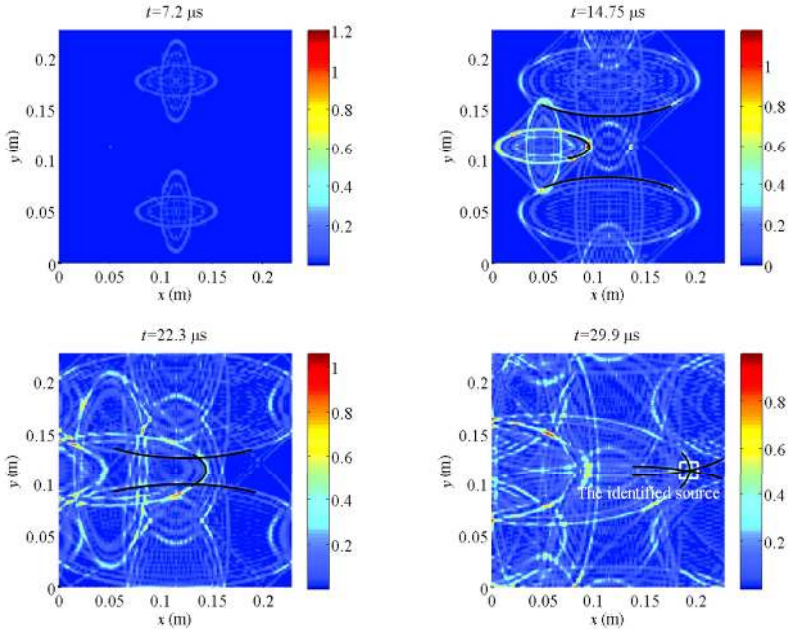

Figure 7.9: The passive TR simulation: the time reversed wave field focuses on the disturbance source.

showed the time origin. The end time of the window however, was different for each measured signal, and was determined based on the amplitude of the incoming waves being 35% of the maximum measured amplitude at that measurement point. This selection was empirical and based on detecting the main wave envelop received at each sensor location, however, slightly higher or lower values may be also used. Consequent to this selection, the sampling numbers corresponding to the end of the window for s1, s2, and s3 are 489, 362, and 488, respectively. Since the signals are time reversed in the TR scheme, the data samples beyond 489 can be discarded in all signals.

In accordance with the roadmap in Figure 7.1, the resulting signals were time-reversed and fed into the 2D wavelet-based spectral finite element method (WSFEM) simulation tool developed in Chapter 5. The mesh pattern in the WSFEM was 32×32, the total simulation time was $30\,\mu$s, the number of temporal sampling points in the wavelet-Galerkin discretization scheme, i.e. L, was 150. The back-propagated waves with non-circular fronts converged to the location (0.190,0.114)m at time $29.9\,\mu$s, shown in Figure 7.9. The indicated location by the TR scheme, when compared to the actual location of the source (0.178,0.114)m, shows a promising deviation of about 6.7%. Note that although less carefully-chosen windowing or denoising parameters may further increase

this error, the source location may be still narrowed down with certain accuracy. Similar analyses, not shown, with different disturbance locations were also performed by Melo Mota [2011] with similar success in identifying the disturbance location.

Some remarks about the example shown above are necessary. As discussed above, although s2 was fired the last, it reaches the disturbance source at the same time as the signals sent from s1 and s3, since the waves propagate faster along the direction of the fibers. It can also be observed from Figure 7.9 that there is another focusing point at about $14\,\mu$s at the location $(0.095, 0.12)$, which may be misinterpreted as a disturbance source. Such issues, as discussed earlier in this chapter, mainly arise from (i) the reflections from the boundaries in the numerical model, and/or (ii) the sensors being placed at non-optimized locations. If for example, there had been a fourth sensor at the right half of the plate, it would have sensed the incoming waves earlier than the other sensors, since it would have been closer to the source. With the TR scheme, the hypothetic sensor would have fired last, even after $14\,\mu$s, resulting in a unique focusing point. This reveals the importance of the appropriate placement of the sensors required for operational SHM systems. To further improve the TR image, absorbing boundaries can be used in the numerical model so that the interactions with the reflected waves are eliminated.

7.5 Extension of the Passive TR to Damage Identification

An external force applied to a structure can be viewed as a disturbance the location and possibly the intensity of which can be determined using a TR-based approach. A defect, when GUW are used, can be interpreted as a secondary, i.e. reflective, disturbance source that only reflects and scatters the incoming waves. Detection of damage using a passive TR approach often needs an extra step to prevent focusing of the back-propagated wavefield on the main source, i.e. the location of the GUW actuator. The mechanism of this prevention is removing the direct waves from the actuator to the sensors, which may be performed in a single step of windowing out some parts of the signal [Wang and Yuan, 2009], or a series of successive sub-steps that keep subtracting the components focusing on the primary source until the secondary source is found [Levine et al., 2011]. The former is more aligned with the objectives and constraints of SHM of composites in this research, due to its superior computational aspects. Note that defining the windowing functions requires determination of the arrival times of the direct waves from the actuator to the sensors before back-propagating the wavefield, which needs to be done only once for a specific structure using a forward model of the structure.

Another important remark about the passive TR in the view of this thesis is on the severity of the damage. In a traditional NDT system for which time is not as crucial as in an on-line SHM system, a number of steps subsequent

to the damage localization may be thought of, to more accurately estimate the extent of the damage. It is believed that in most aerospace applications of SHM systems, in which the processing time, cost, and safety are highly coupled, the extra steps beyond a certain resolution may not be justified. To determine if there are defects larger than a certain size, the frequency content of the diagnostic waves may be tuned such that the waves interact with all the defects larger than half of their wavelength. Any secondary source, which is found by the SHM system can hence, be ascribed to a defect larger than the critical detection size. This approach can provide an adjustable resolution for the SHM system, that depending on the situation, can vary from faster processing-lower sensitivity to slower processing-higher sensitivity, i.e. resolution.

7.5.1 Case Study II: Delamination Identification in a Composite Beam

A numerical example is presented in this section to demonstrate how the passive time reversal may be employed to detect discontinuities, e.g. damage, as reflective targets. The passive TR-based approach is utilized for SHM of a delaminated composite beam, the response of which is simulated using the 3D WSFEM. As the numerical simulation tool required for the passive TR, the 1D WSFEM formulated in Chapter 4, which is fast and computationally efficient, is employed.

Consider a $10\times1\times600$ mm^3 beam-like composite structure made of graphite-epoxy used in Case Study I, and ply stacking sequence of $[0,0,90,90]_s$, where the 0° angle is along the length-wise direction z. As shown in the schematic view of the structure in Figure 7.10, a delamination is assumed between layers 2 and 3 of the laminate, which is located at the area:

$$\{5\text{mm} < x < 10\text{mm},\ 330\text{mm} < z < 360\text{mm}\}.$$

To model the structure, the 3D WSFEM, based on the wavelet-Galerkin discretization of time, and the higher order pseudo-spectral finite element method (SEM) for discretization of space, were employed, the details of which were outlined in Chapter 6. In the 3D SEM elements, $N_x = 5$, $N_y = 3$, and $N_z = 7$, where N_i for $i = x, y, z$, denotes the order of the polynomial basis in the i-direction. Using such elements, the structure was discretized with $n_x = 2$, $n_y = 4$, and $n_z = 20$, where n_i, denotes the number of elements along the i-direction. As a result, the finite element model had 20163 nodes, each of which had three translational displacement degrees of freedom u, v, and w along x, y, and z directions. The model therefore, includes 60489 spatial degrees of freedom.

To generate diagnostic guided waves in the structure, a narrow-banded 3-cycle Hanning windowed sinusoidal pulse, as shown in Figure 7.11, was used to excite the structure. Symmetric waves were chosen for this example for which both the upper and the lower surfaces of the structure should be excited simultaneously. Indeed the tuning techniques for guided waves discussed in

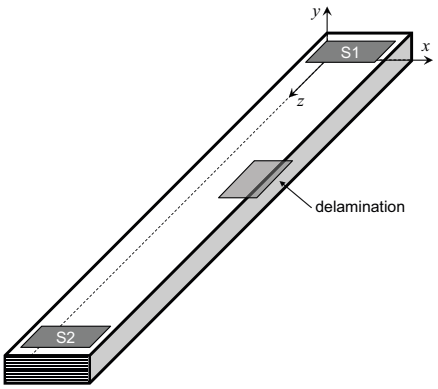

Figure 7.10: The composite beam-like structure with a delamination. The structure is not clamped, i.e. free-free, and sensors s1 and s2 are placed on the top surface of the beam at the two ends.

Chapter 2 can also be used to generate a single wave mode from a single surface. In this case, the signal in Figure 7.11 was applied as a distributed line load on $\{z = 30\text{mm}, y = 0\}$ and $\{z = 30\text{mm}, y = 10\text{mm}\}$ along z-direction.

The displacement response of the structure, in the presence and absence of the delamination, has been obtained for four points on the top surface of the beam, i.e. $y = 1$ mm: A(5,1,30)mm, B(0,1,300)mm, C(10,1,300)mm, and D(5,1,570)mm. The displacement components u, v, w for the undamaged case, i.e. the beam without delamination, and the damaged case can be observed in Figure 7.12 and Figure 7.13, respectively.

In the undamaged case, the displacement field at points A and D had no component along x, i.e. $u = 0$, which happened due to symmetry in the geometry and loading. For the same reasons, at points B and C, these displacements were non-zero and equal in magnitude, i.e. $|u|_B = |u|_C$. The largest wave packet arriving at 50 μs were S0 waves, which were followed by SH0 waves with maximum amplitude at about 75 μs. In the damaged case, the delamination has broken the symmetry with respect to the plane $x = 5$ mm. This effect can be seen at points B and C, with inherently different x-components of the displacement, i.e. u. Also the displacement along x, i.e. u in the damaged case is non-zero. The y-component of the displacement response, i.e. v, appeared to be very sensitive to the presence of the delamination. Substantial difference in v at points B and C can be observed in the figures. The most important change due to the delamination however, is the additional wave packet at point D, which appeared about 80 μs after excitation. The incoming symmetric waves passing through the delaminated area experienced a mode conversion as a part of the diagnostic wave packet turned into antisymmetric waves dominated by an out-of-plane displacement. This mode conversion will be used later in this example, to identify the delamination location. Finally, the z-component of the displacement response, i.e. w, was influenced the least by the delamination.

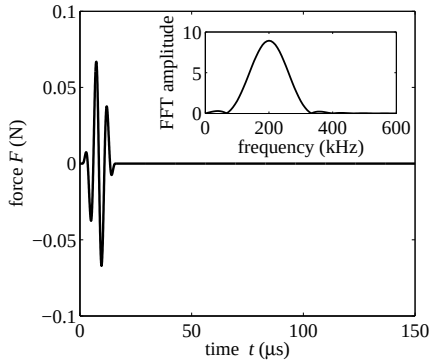

Figure 7.11: The narrow-banded excitation pulse with a central frequency of 200kHz.

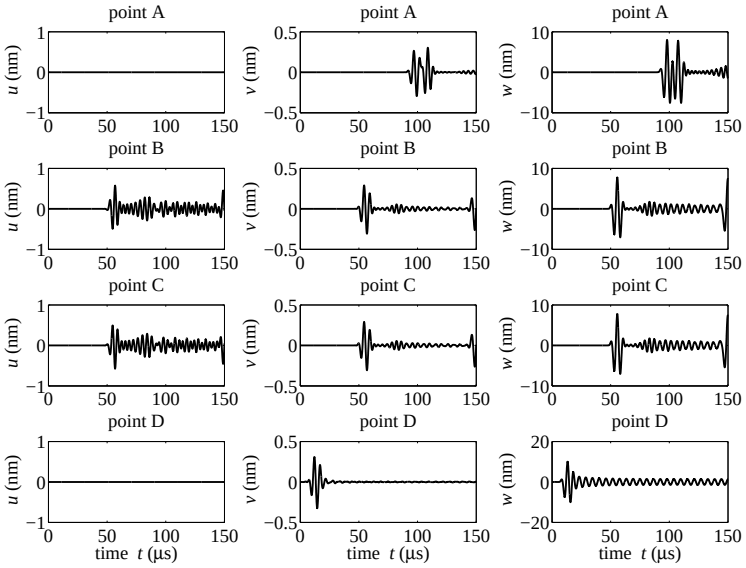

Figure 7.12: The displacement response of the undamaged beam-like structure: the displacement components u, v, and w are shown at four points A(5,1,30)mm, B(0,1,300)mm, C(10,1,300)mm, and D(5,1,570)mm.

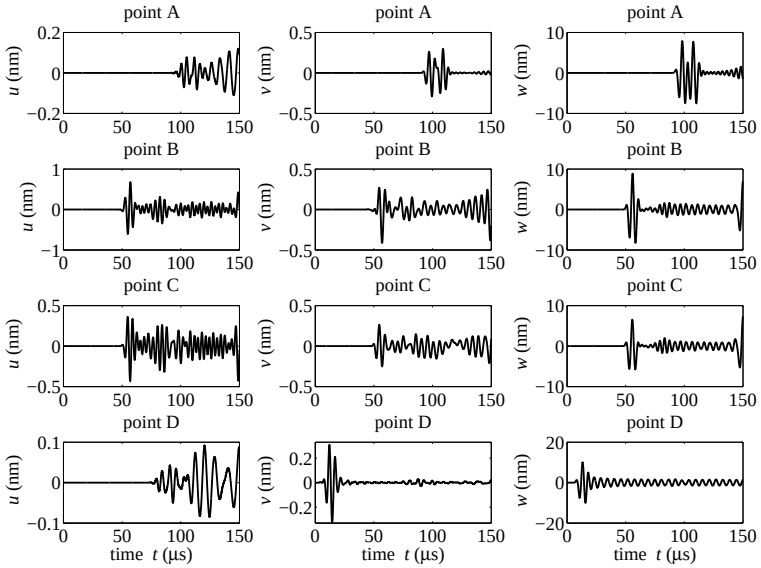

Figure 7.13: The displacement response of the delaminated beam-like structure: the displacement components u, v, and w are shown at four points A(5,1,30)mm, B(0,1,300)mm, C(10,1,300)mm, and D(5,1,570)mm.

The waveguide, which is split into two sub-waveguides by the delamination did not significantly affect the fundamental symmetric waves dominated by w.

The y-component of the response of the delaminated beam to the high-frequency load pulse, i.e. v, at points A(5,1,30)mm and D(5,1,570)mm as the assumed measurement points was stored in a file and used in the passive-TR scheme for SHM. It should be noted that for this illustrative example, one may be able to use more basic time-delay techniques for finding the delamination location. As mentioned before however, such techniques are not readily applicable to anisotropic or heterogeneous structures in general.

In order to identify the location of the delamination using the simulated data and the passive TR method, the parts of the response signals which contain unnecessary information for the damage identification scheme and are thus distracting should be truncated out of the signals. Windowing, as the mechanism for this task in this dissertation, was applied to the normalized response signals at points A and D, as shown in Figure 7.14 and Figure 7.15. The windowing process was performed based on removing the boundary reflections, and the wave packets travelling slower than the fastest waves recognized at the measurement points. Although there is some freedom in selection of the windowing function, an inappropriate choice of the window, as discussed in Section 7.1.2, may result in deviation from the actual delamination location, or in the worst

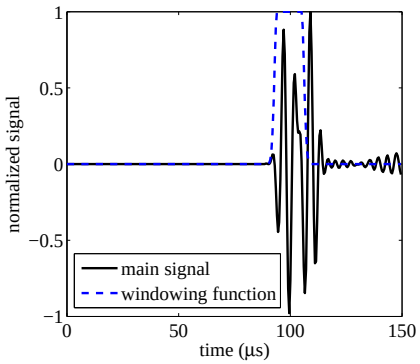

Figure 7.14: Windowing of the normalized signal obtained at the location of sensor s1.

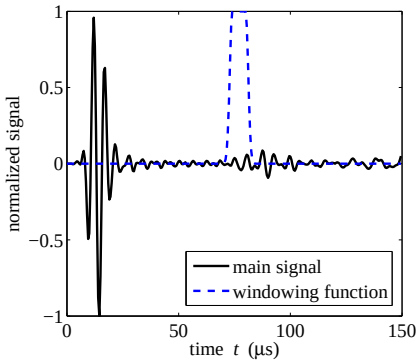

Figure 7.15: Windowing of the normalized signal obtained at the location of sensor s2.

case scenario, resulting in false indication of the damage.

The normalized windowed signals are next, in accordance with the passive-TR method, time-reversed and fed in form of nodal forces into the 1D WSFEM developed in Chapter 4. Note that although the 1D WSFEM, as concluded in Chapter 4, may not be as accurate as the 3D model at high frequencies, it requires the minimum possible number of elements to capture the structural response and is computationally efficient. In this example, only one finite element was used for the spatial discretization. The temporal discretization was performed with 500 temporal sampling points, i.e. $L = 500$, and the time step size of $\Delta t = 0.5\,\mu$s. The total simulation time $L \times \Delta t = 250\,\mu$s is increased for $100\,\mu$s with respect to the forward simulations to ensure that the back-propagated waves cover the entire spatial domain, as will be seen later in this section.

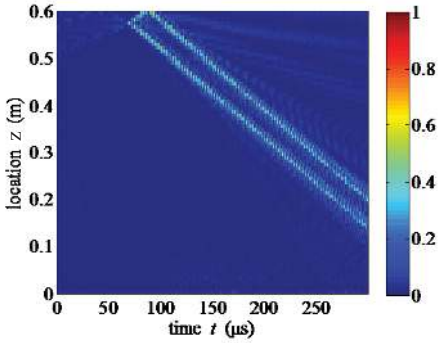

Figure 7.16: The normalized displacement response of the structure to the time-reversed windowed signals applied from the location of sensor s1.

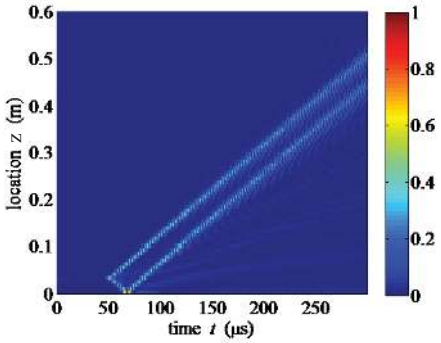

Figure 7.17: The normalized displacement response of the structure to the time-reversed windowed signals applied from the location of sensor s2.

The response of the structure to the time-reversed windowed signals exerted from the locations of s1 and s2, cf. Figure 7.10, were obtained separately as the resulting wavefield is demonstrated in Figure 7.17 and Figure 7.18, respectively. The windowed signal which has arrived first, after the time reversal process, is sent back the last. In addition, the sensor locations were chosen to be 3 cm distant from the beam ends to illustrate one of the challenges that one may encounter in a real SHM system: there are second branches starting at $z = 0$ and $z = 0.6$ m with the same slope as the main wave packet which start at $z = 0.03$ m and $z = 0.57$ mm in Figure 7.17 and Figure 7.18, which are the reflections of the main packets from the left and the right ends of the beam. Note also from the figures that the selected 250 μs time window allows each time reversed wave packet to reach almost the opposite end of the beam.

Superposition of the responses shown in Figure 7.17 and Figure 7.18 is shown in Figure 7.18. It demonstrates how the passive time reversal scheme converged

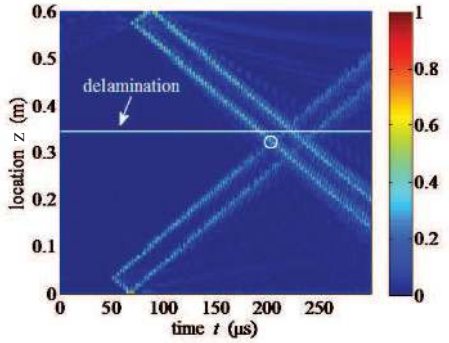

Figure 7.18: Superposition of the time reversal responses shown in Figure 7.17 and Figure 7.18. The center-point of actual delamination is located at $z = 0.345$m and shown by the white solid line.

and pin-pointed the delamination location at the point $z = 0.325$m and $t = 200\,\mu$s, which deviates only 5.8% from the center-point of the delamination. There are however, more intersection points in the figure due to the reflected waves by the beam ends, as discussed above. Using absorbing boundaries which prevent the secondary reflected wave packets, one can remove these incorrect intersection points. Dealing with this issue however, may be required for some practical SHM systems, and is not within the scope of the present dissertation.

7.6 A Remark on Using the Passive TR for Complex Structures

It is worthwhile here to discuss the performance of the approach when applied to more complex structures. As shown in the previous section, anisotropy can be readily dealt with using the presented passive TR approach. Heterogeneity also, when the variation of the structural and material properties is smooth, does not require extra caution. Local heterogeneity however, e.g. discontinuities, may require more attention. When for example, a structure with a cut-out or a panel with a number of rivets or bolts is investigated, there will be an extra step in the damage or impact load identification. Similar to the approach employed for a damaged structure in this section, such discontinuities do not need to be modeled in the numerical simulator used in the passive TR scheme. As a consequence of this simplified modeling, when damaged regions exist, the passive TR scheme focuses on multiple points some of which are the structural discontinuities, e.g. rivets, and the rest are the damaged areas. Interpretation of the TR image for extraction of the damaged areas in this case, thus requires a prior knowledge about all structural entities and their general characteristics.

Note again that this TR-based approach only detects the existence and the location of disturbance sources and provides no explicit information about the type of the defect.

7.7 Concluding Remarks

The passive time reversal scheme, as a model-based SHM methodology, was presented in this chapter, which allows identification of the external load on, and damage in heterogeneous and anisotropic structures. Having briefly presented a number of major required mathematical tools to develop a SHM system, they were combined with the WSFEM formulated in chapters 4 and 5 for 1D and 2D waveguides. The implemented passive TR method was successfully used for load source identification in a graphite-epoxy laminate based on its experimentally obtained response. The methodology was also applied to identification of delamination location in a composite beam-like structure, the response of which was simulated using the 3D WSFEM formulated in Chapter 6.

Chapter 8

Conclusion and Recommendations for Future Research

In the present dissertation, it was attempted to contribute to the research field structural health monitoring (SHM) of thin-walled composite structures, by improving on certain aspects of analysis and modeling guided ultrasonic waves (GUWs). The motivation of using GUWs, as discussed in Chapter 1, mainly came from some of their important features, e.g. low implementation costs, repeatability, ability to inspect a large structure in a short time, sensitivity to small damage, low energy consumption, and ability to detect both surface and internal damage.

Some background information on GUWs-based SHM, which was necessary for description of the consequent chapters, was presented in Chapter 2. A higher-order shell theory was also implemented in this chapter, which can be used for extraction of the dispersion properties and wave curves of GUWs in flat and cylindrical shells. Having reviewed some of most commonly-used simulation tools for GUWs, and discussing their merits and limitations, the WSFEM was introduced in chapters 3 to 6. Addressing the mathematical foundation of wavelets and the wavelet-Galerkin method in Chapter 3, the 1D, 2D, and 3D formulations of the WSFEM were presented in chapters 4, 5, and 6, respectively. A model-based SHM technique for detection of load/damage location with the minimum number of measurement points was finally introduced in Chapter 7.

8.1 Conclusions

The following conclusions can be made from this work.

1. The wavelet-Galerkin method (WGM) can be effectively used for temporal discretization of linear initial-boundary-value problems (chapters 3 to 6).

2. The edge effects of the wavelet transform can be completely eliminated for zero initial conditions, if a finite interval equal to the time window of the problem of interest is considered for computation of the connection coefficients of wavelets (Chapter 3).

3. Using the edge effect removal scheme proposed by this dissertation, about 50% reduction in the number of sampling points in time was achieved compared to the conventional method based on wavelet-extrapolation technique (Chapter 3).

4. The WGM can be implemented such that the equations at different solution steps become independent. This makes the scheme suitable for parallel implementation (Chapter 3).

5. In formulation of the decoupled wavelet-Galerkin method (DWG), complex-valued wavelet frequencies were introduced at which the system responses are computed independently, and superposed in a way that the final response in time is constructed (Chapter 3).

6. Using the decoupled wavelet-Galerkin scheme, one-dimensional problems can be solved exactly in the spatial domain. Accordingly, if the finite element shape functions are constructed based on the exact free-space solution of the wave equation, the minimum number of elements is required to model wave propagation (Chapter 4).

7. The accuracy of the one-dimensional problems is associated with the wave modes which can be captured by the model at the frequency range of excitation. At higher frequencies, a 1D model becomes less accurate, and the frequency range at which a 1D model is sufficiently accurate can be expanded by incorporating more wave modes in the assumed displacement field and the interpolation functions. An improved 1D wavelet-based spectral finite element model was formulated in Chapter 4.

8. A novel formulation of 2D wavelet-based spectral finite element method (WSFEM) was developed, which utilizes the waveguide characteristics of structures in derivation of the shape functions of the finite element spatial discretization (Chapter 5).

9. The 2D WSFEM can save up to 50% in spatial degrees of freedom for the same accuracy as the FEM with quadratic basis functions equipped with an explicit time integration scheme (Chapter 5).

10. A substantial reduction in the number of temporal sampling points can be achieved using the WSFEM compared to the explicit Newmark time integration scheme. The solution times however, cannot be explicitly compared as the two methods are essentially different. One of the most influential parameters in solution time of the WSFEM is the number of CPUs available (chapters 5 and 6).

11. A novel formulation of the WSFEM for 3D waveguides was presented. It was demonstrated that standard FEM discretization schemes can be adopted in the WSFEM formulation to cope with complex problems (Chapter 6).

12. The so-called spectral element method, i.e. FEM with higher-order polynomial basis functions on the Gauss-Lobatto-Legendre grid, which has superior convergence properties and the ability of more accurately capturing complex geometries compared to conventional FEM, can be combined with the DWG to achieve spectral convergence in both temporal and spatial discretization (Chapter 6).

13. A computational time saving scheme can be utilized to reduce the number of equations in the DWG. Using the procedure suggested in Chapter 6, a substantial savings can be achieved by neglecting the response of the system at the wavelet frequencies which do not significantly contribute to the dynamic response of the structure.

14. The developed WSFEM can be employed in a model-based SHM system for detection of load and damage location. For this purpose, the passive time reversal (TR) approach was formulated in Chapter 7, which operates based on time invariance of linear elastodynamic equations. Using the passive TR scheme, the problem of load and damage detection, which is essentially an inverse problem, may be solved in form of a forward problem, without encountering uniqueness and stability issues (Chapter 7).

15. The location of the external applied load on a graphite epoxy panel was successfully detected using the TR-based SHM system with less than 7% relative error. The loading location, which was found by the SHM system, matched very well with the actual location of the actuator in the experiments (Chapter 7).

16. The extension of the TR-based system for impact location to delamination detection in composites was demonstrated using a numerical example, in which the response of the delaminated composite beam was simulated using the 3D WSFEM. The SHM system was equipped with the 1D WSFEM to accurately and quickly process the input data (Chapter 7).

8.2 Recommendations for Future Research

Some recommendations for continuation of this research are listed below.

1. The developed WSFEM can be employed for modeling sensors and actuators in SHM systems. In case of piezoelectric sensors and actuators for example, the decoupling of the equations in the transformed domain can be advantageous, since the governing equations of the piezoelectric material and the wave motion appear uncoupled in the same space.

2. For simulation of wave propagation in geometrically complex waveguides, the WSFEM can be combined with an isogeometric spatial discretization to take advantage of both an accurate representation of the geometry and a parallelized solution.

3. More experiments can be conducted to evaluate the performance of the passive TR-based SHM system.

4. In the structural design process of composite structures, an optimized performance of the GUWs-based SHM system can be considered: a waveguide may be designed to improve the information transmission for possible damage, carried out by ultrasonic diagnostic waves.

5. The passive TR-based scheme can be used to identify damage in non-conventional composite structures, e.g. variable-stiffness composites, APPPLY composites.

Appendix A

Continuous and Discrete Fourier Transform

The Fourier transform is the most extensively used transform method in signal processing due to its computational superiority and the ease of implementation of its direct and inverse algorithms. In this appendix, the continuous Fourier transform (CFT) and discrete Fourier transform (DFT) are presented in brief.

The continuous Fourier transform pair of the absolutely integrable function $f(t)$ on $(-\infty, +\infty)$ can be expressed by the following relations.

$$\hat{f}(\omega) = \int_{-\infty}^{+\infty} f(t) e^{-i\omega t} dt \tag{A.1}$$

$$f(t) = \frac{1}{2\pi} \int_{-\infty}^{+\infty} \bar{f}(\omega) e^{+i\omega t} d\omega \tag{A.2}$$

Since the CFT requires the signals to be known analytically, the discrete form, i.e. DFT, is predominantly used in engineering applications.

The DFT of a signal assumes periodicity in the time domain T. For non-periodic signals, the approximation error may be minimized under certain circumstances, mainly if the signal has a large duration of zero amplitude and the analysis assumes it repeats itself on a period which is very large compared to the time of interest. By uniformly discretizing the time domain into M intervals with length ΔT and the frequency domain into N constant segments, there exist $\omega_n = \frac{2n\pi}{T}$ and $t_m = m\Delta T$, where $n = 0, \cdots, N-1$ and $m = 0, \cdots, M-1$. The DFT and its inverse read,

$$\hat{f}_n = \hat{f}(\omega_n) = \Delta T \sum_{m=0}^{N-1} f_m e^{-i\omega_n t_m} = \Delta T \sum_{m=0}^{N-1} f_m e^{-i2\pi nm/N} \tag{A.3}$$

$$f_m = f(t_m) = \frac{1}{T} \sum_{n=0}^{N-1} \hat{f}_n e^{+i\omega_n t_m} = \frac{1}{T} \sum_{n=0}^{N-1} \hat{f}_n e^{+i2\pi nm/N} \tag{A.4}$$

The above equations are the foundation of the DFT and the fast Fourier transform (FFT) algorithm, the details of which can be found in [Strang, 2007].

Appendix B

Computation of the Derivatives and Integrals of Daubechies Wavelets

A brief description of the algorithms required for exact evaluation of finite integrals, whose integrands involve products of Daubechies compactly supported wavelets, is provided in this appendix. The method outlined here has minor modifications to the work done by Chen and Hwang [1996].

B.1 Evaluation of the Scaling Function and Its Derivatives

Evaluation of the scaling function of an arbitrary-order Daubechies wavelet is not only necessary for calculation of the approximation coefficients, but also needed, together with its derivatives, for computation of the exact values of connection coefficients. The same algorithm for calculation of derivatives at integer points can be used for evaluation of the scaling function values as well, when the differentiation order is zero.

The derivatives of the scaling function up to order $N/2-1$ exist [Beylkin, 1992]. Taking the nth derivative of both sides of the two-scale relation 3.19 gives

$$\varphi^{(n)}(\tau) = 2^n \sum_{k=0}^{N-1} a_k \varphi^{(n)}(2\tau - k). \tag{B.1}$$

In order to obtain the values of $\varphi^{(n)}(\tau)$ at integer points, $\tau = 1, 2, \cdots, N-2$ are substituted in the above two-scale relation. Points 0 and $N-1$ are not required to be calculated, since their values are zero for Daubechies wavelets.

Therefore,

$$2^{-n}\chi = \mathbf{P}\chi; \chi = [\ \varphi^{(n)}(1) \quad \varphi^{(n)}(2) \quad \cdots \quad \varphi^{(n)}(N-2)\ ]^T \tag{B.2}$$

where $\mathbf{P}$ is the matrix of the filter coefficients. To determine the vector χ, a normalizing equation is required [Chen and Hwang, 1996]:

$$\sum_{k=1}^{N-2} (-k)^n \varphi^{(n)}(k) = n!. \tag{B.3}$$

B.2 Calculation of Multiple Integrals of the Scaling Function

The n-tuple integrals of the scaling function are defined as:

$$\theta_n(\tau) = \int_0^\tau \int_0^{\xi_n} \cdots \int_0^{\xi_2} \varphi(\xi_1)\, d\xi_1 \cdots d\xi_{n-1} d\xi_n = \int_0^\tau \theta_{n-1}(\xi)\, d\xi. \tag{B.4}$$

Note that the above integral is not explicitly used in computation of the scaling or connection coefficients. In the coming sections however, it will be used in calculation of moments of the scaling function required for evaluation of connection coefficients of Daubechies wavelets. Application of the two-scale relation (B.1) to Equation (B.4) results in another two-scale relation, but with respect to θ_n:

$$\theta_n(\tau) = 2^{-n} \sum_{k=0}^{N-1} a_k \theta_n(2\tau - k). \tag{B.5}$$

Since the values of $\theta_n(\tau)$ for $\tau \geq N-1$ do not vanish, the procedure of computing these values is different than what presented before for φ. The details of these calculations can be found in [Chen and Hwang, 1996]. For the completeness sake, only the key equations are shown here. As the first step, consider the following relation for $\tau \geq N-1$,

$$\theta_n(\tau) = \sum_{k=0}^{N-1} \frac{(\tau - N + 1)^k}{k!} \theta_{n-k}(N-1) \tag{B.6}$$

where $\theta_n(N-1) = 1$. Utilization of this equation requires the values of $\theta_{n-k}(N-1); \forall k = 0, 1, \cdots, n-2$ to be determined. From the two-scale relation (B.1), the following recursive formula for $n = 2, 3, \cdots$ can be extracted [Chen and Hwang, 1996].

$$\theta_n(N-1) = \frac{1}{2^n - 2} \sum_{j=1}^{n-1} \left(\sum_{k=0}^{N-1} \frac{(N-1-k)^j}{j!} \right) \theta_{n-j}(N-1). \tag{B.7}$$

Having obtained $\theta_n(\tau)$ for $\tau \geq N-1$, the values of $\theta_n(\tau)$ for $\tau = 1, 2, \cdots, N-2$ can be computed via Equation (B.5). Matrix representation of the equations facilitates the computation procedure.

B.3 Moments of the Scaling Function

The moments of a wavelet scaling function over a bounded interval are given by:

$$M_k^m(\tau) = \int_0^\tau \xi^m \varphi(\xi - k)\, d\xi. \tag{B.8}$$

Performing integration by parts of the above integral successively m times results in [Chen and Hwang, 1996]:

$$\begin{aligned} & M_k^m(\tau) = \tau^m \theta_1(\tau - k) - m \textstyle\int_{-k}^{\tau-k} (\xi + k)^{m-1} \varphi(\xi)\, d\xi \\ & \vdots \\ & = \textstyle\sum_{l=0}^{m} (-1)^j \frac{m!}{(m-i)!} \tau^{m-i} \theta_{i+1}(\tau - k) + (-1)^{m+1} m! \theta_{m+1}(-k). \end{aligned} \tag{B.9}$$

The integral (B.8) can therefore, be computed exactly over a bounded interval. The reason for the exact evaluation of the integral is that the compactly-supported wavelets are highly oscillatory, hence, it is difficult and unstable to numerically compute these coefficients [Chen and Hwang, 1996].

B.4 Evaluation of the Connection Coefficients

The inner product of the scaling function and its nth order derivative are denoted by:

$$\Gamma_k^n(\tau) = \int_0^\tau \varphi^{(n)}(\xi - k)\varphi(\xi) d\xi, \tag{B.10}$$

whose exact evaluation is a key element of the wavelet-Galerkin method. The following properties of the connection coefficients were presented by Chen and Hwang [1996]:

$$\Gamma_k^n(\tau) = \Gamma_k^n(N-1); \forall \tau \geq N-1 \tag{B.11}$$

$$\Gamma_k^n(\tau) = 0; \forall\, |k| \geq N-1, \text{or}, \tau \leq 0, \text{or}, \tau \leq k \tag{B.12}$$

$$\Gamma_{-k}^n(N-1) = (-1)^{\text{n}} \Gamma_k^n(N-1); \forall k \geq 0 \tag{B.13}$$

$$\Gamma_{-k}^n(\tau) = (-1)^{\text{n}} \Gamma_k^n(N-1); \forall \tau + k \geq N-1. \tag{B.14}$$

Relations (B.11) and (B.12) are extracted from the fact that the support of $\varphi(\xi)$ is $[0, N-1]$, which does not overlap with that of $\varphi^n(\xi - k)$ for $|k| > N-1$. Properties (B.13) and (B.14) are derived from Equation (B.10) by performing integration by parts n times. Applying the two-scale relation (B.1) to (B.10) results in

$$\Gamma_k^n(\tau) = 2^{n-1} \sum_{i=0}^{N-1} \sum_{j=0}^{N-1} a_i a_j \Gamma_{2k+i-j}^n(2\tau - j). \tag{B.15}$$

For evaluation of $\Gamma_k^n(\tau)$ at $\tau = 1, 2, , N-1$, the values of $\Gamma_k^n(N-1)$ need to be predetermined. Using equations (B.11) and (B.15), it can be extracted that

$$\Gamma_k^n(N-1) = 2^{n-1} \sum_{i=0}^{N-1} \sum_{j=0}^{N-1} a_i a_j \Gamma_{2k+i-j}^n(N-1). \tag{B.16}$$

The introduced relation for calculation of $\Gamma_k^n(N-1)$ can be then arranged in a matrix-vector form. To derive the additionally-imposed constraint for normalizing the resulting vector of $\Gamma_k^n(N-1)$ for $k = 0, 1, \cdots, N-2$, Chen and Hwang [1996] utilized the following relation:

$$\sum_{k=-\infty}^{+\infty} k^n \varphi^{(n)}(\tau - k) = n!. \tag{B.17}$$

Considering properties (B.12) and (B.13), multiplication of both sides of the above equation by φ and integrating over $(-\infty, \infty)$ reads

$$\sum_{k=1}^{N-2} k^n \Gamma_k^{(n)}(N-1) = \frac{n!}{2}. \tag{B.18}$$

Once the values of $\Gamma_k^n(N-1)$ are determined, the values of $\Gamma_k^n(\tau)$ for $\tau = 0, 1, , N-2$ and $|\tau| \geq N-2$ can be obtained via Equation (B.15). For this purpose, only $(N-2)^2$ independent components in the following set are needed:

$$\left\{\Gamma_k^n(\tau); \tau = 1, 2, \ldots, N-2; \tau - N + 2 \leq k \leq \tau - 1\right\}. \tag{B.19}$$

In matrix-vector notation, it can be written as

$$\left(2^{1-n}\mathbf{I} - \mathbf{H}\right)\mathbf{G} = \mathbf{d} \tag{B.20}$$

where $\mathbf{G}$ is the vector of all independent members. The system above does not require any normalization for $n = 0$. For $n > 0$ however, the matrix $\left(2^{1-n}\mathbf{I} - \mathbf{H}\right)$ is singular with the rank deficiency n. The procedure for removing the rank deficiency is outlined in Chen and Hwang [1996]. Finally, the values of $\Gamma_k^n(\tau)$ can be determined for integer values of n, k, and τ.

From the formulation presented, the connection coefficients in Equation (3.37), i.e. $\left\langle \varphi_k^{(n)}, \varphi_j \right\rangle$, being equivalent to:

$$\int_0^\tau \varphi^{(n)}(\xi - k)\varphi(\xi - j)d\xi, \tag{B.21}$$

can be readily computed by the change of variables $z = \xi - j$. This results in:

$$\int_{-j}^{\tau-j} \varphi^{(n)}(z - [k-j])\varphi(z)dz = \Gamma_{k-j}^n(\tau). \tag{B.22}$$

Equation (B.22), in which the integral bounds are updated according to the new variable z, can be split into two parts by subdividing the integration domain as follows.

$$\Gamma^n_{k-j}(\tau) = -\int_0^{-j} \varphi^{(n)}(z-[k-j])\varphi(z)dz + \int_0^{\tau-j} \varphi^{(n)}(z-[k-j])\varphi(z)dz. \tag{B.23}$$

The first term in the equation above is zero in accordance with Equation (B.12), hence,

$$\Gamma^n_{k-j}(\tau) = \int_0^{\tau-j} \varphi^{(n)}(z-[k-j])\varphi(z)dz, \tag{B.24}$$

which can be calculated using the procedure outlined above.

Appendix C

Numerical Dispersion of the WSFEM

As mentioned in Chapter 6 Section 6.3, the spectral nature of the formulated wavelet-based spectral finite element method (WSFEM) circumvents numerical dispersion issues in the approach. This feature of spectral methods is also reported in the literature, see for example Gazdag [1981], Fornberg [1987]. To demonstrate this with a numerical example, a 2D aluminium plate under the plane-stress condition is considered in this section. The plate dimensions were considered to be $2000 \times 1000 \times 1\text{mm}^3$, to be large enough to avoid reflections in the time window of interest. For the spatial discretization, the order of SEM was 5 in both directions. The source, which was a 5-cycle Hanning-windowed sinusoidal pulse, was placed 800 mm from the receiver. In Figure C.1, L shows the number of sampling points in time, the horizontal axis shows the spatial discretization, i.e. the number of nodes in SEM per wavelength of P waves at the central frequency of excitation, and the vertical axis is the normalized wave speed. Very little numerical dispersion was observed: the arrival time of the simulated waves is hardly influenced by the spatial discretization. Although not shown here, similar analyses were also performed for shear-horizontal and Rayleigh waves, which all resulted similarly.

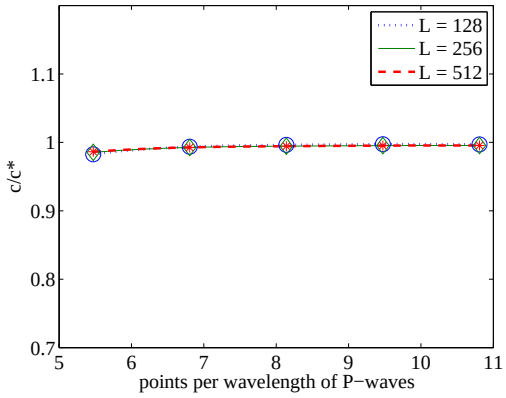

Figure C.1: Numerical dispersion of the WSFEM.

Appendix D

Parallelization Scalability of the WSFEM

The straight-forward parallelization of the wavelet-based spectral finite element method (WSFEM) can be advantageous in many computationally-intensive applications. As discussed earlier Chapter 6, the solution at different wavelet points can be done independently using different processors or CPU cores. For the 2D problem in Appendix C, the relation between the solution time and the number of available CPU cores was investigated on two systems: one a desktop with 16 GB internal memory and an Intel i5-2400 CPU, and the other one, i.e. System 2, a Dell Precision T7500 workstation with 96 GB internal memory, which, at the time of this study, was in use by some other simulation programs as well. As can be observed in Figure D.1, the solution time-number of cores relation is almost linear up to 2 cores, i.e. the solution time when using two cores is nearly half of the base case solution which uses a single core. As the number of cores increases, however, the efficiency of parallelization drops. The nonlinear relation of the number of cores and the solution time is attributed to the memory bandwidth as mentioned in Chapter 6. It can be seen that the parallelization of the same problem works more efficiently on the machine with a higher memory and CPU cache. When using 4 cores for example, System 2 exhibits about 22% improvement compared to System 1, as the normalized solution time for systems 1 and 2 are respectively 0.26 and 0.33.

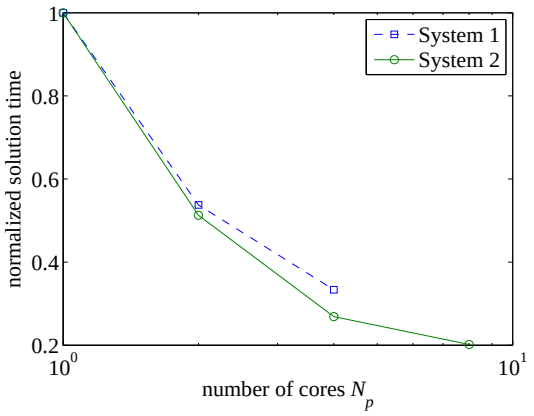

Figure D.1: Scalability of the WSFEM in Parallelization.

Appendix E

Inverse Problem of Crack Identification in Beam Structures

To identify cracks in beam structures exhibiting the characteristics of a 1D waveguide, an inverse solution approach based on the wavelet-based spectral finite element method (WSFEM) was employed. In order to reduce the computational cost of of the inverse problem, fracture mechanics formulas were used with which the damage was parametrized and translated into the numerical solution parameters. Such an approach was formulated in the present research for 1D structures with non-propagating open-edge cracks. In this model, which has been used formerly in Krawczuk et al. [2006] and Ostachowicz [2008], the crack model is considered as a dimensionless massless elastic hinge as depicted in Figure E.1. The crack flexibility is calculated using the Castiglianos theorem, the stress intensity factor for the first mode of the crack formation, and the equations of motion, see Krawczuk et al. [2006] for the details. If the crack type is as considered, the flexibility coefficient of the crack and its location are adequate to describe the defect.

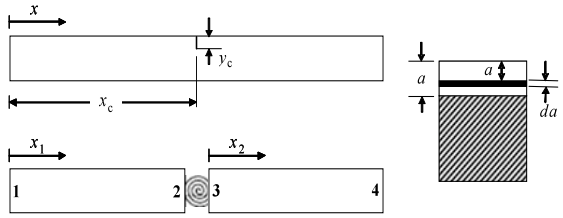

Figure E.1: The model of a rod member with a transverse open and non-propagating crack.

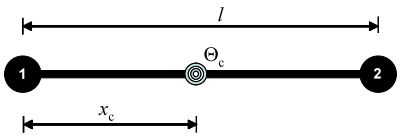

Figure E.2: The condensed wavelet-based finite element with an open-edge crack.

The forward model of the waveguide can be constructed by using two undamaged wavelet-based finite elements as presented in Chapter 4 of this dissertation, connected using a dimensionless spring representing the crack. To further improve the computational efficiency, a node-condensation scheme was applied by imposition of the compatibility conditions at the crack location. This was essentially developing a two-noded cracked element as shown in Figure E.2.

This forward model was used as the kernel of the inverse problem of crack identification. Given the excitation and the properties of the undamaged structure, i.e. geometry and material properties, the inverse solver attempts to find the crack parameters such that the error of the weak-form of the governing equations in the wavelet-transformed domain is minimized.

As demonstrated in chapters 3 to 6, the WSFEM decomposes the solution into the responses at different frequencies. For each of these frequencies, the inverse problem results in some new values of the crack location and flexibility.

To evaluate the accuracy and the stability of the scheme, a number of problems were solved including single and multiple cracks, in the presence of different random noise levels. As an example, the results of an aluminium bar with dimensions $500\times25\times6\text{mm}^3$ is illustrated in this appendix. The bar has two cracks at $x = 100$mm and $x = 300$mm with depth of 4mm and 3mm, respectively. For convenience, a crack index is defined the relation of which with the crack depth is shown in Figure E.3. At the left end, i.e. $x = 0$, the bar is subjected to a 5-cycle Hanning-windowed sinusoidal pulse with the central frequency of 100kHz. The results were simulated with a time domain finite element scheme and stored locally. The results of the inverse solution for 0, 1%, and 10 % random noise are shown in Figure E.4, Figure E.5, and Figure E.6, respectively.

Since the number of sampling points in the inverse WSFEM was 400, the total number of results sets are also 400. The sensitivity of the scheme to the crack location is significantly higher than to the crack index, hence, a stronger convergence can be observed for the crack index estimation. From the figures shown, when the amount of noise increases, less solutions converge to the actual location and index of the cracks. At 1% noise, the identification was still successful. At 10% noise however, the inverse scheme did not identify the cracks.

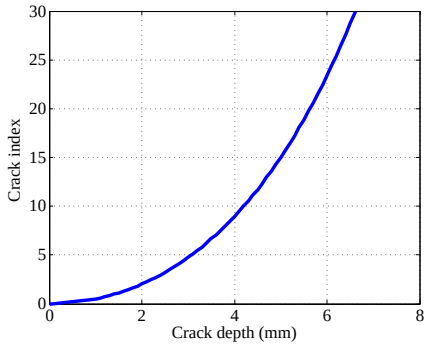

Figure E.3: The condensed wavelet-based finite element with an open-edge crack.

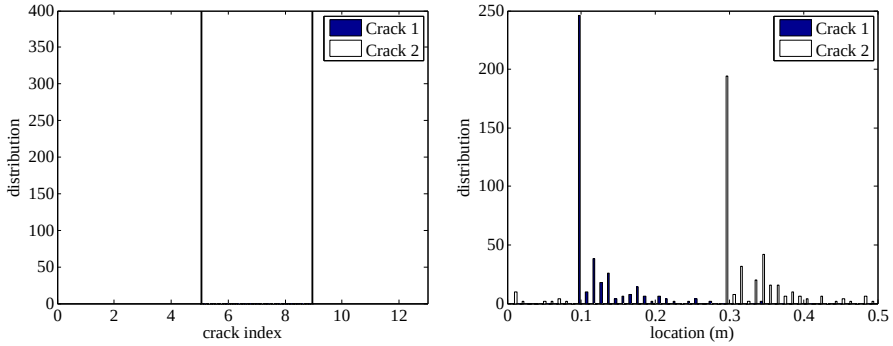

Figure E.4: The histogram of the solution for the indices and the locations of the cracks in the absence of random noise.

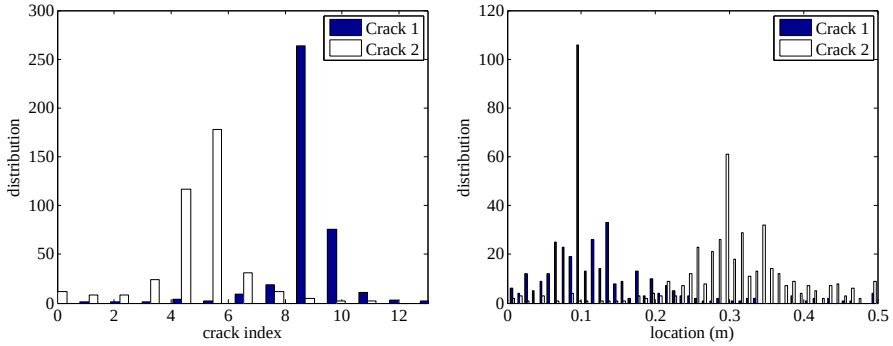

Figure E.5: The histogram of the solution for the indices and the locations of the cracks at 1% random noise.

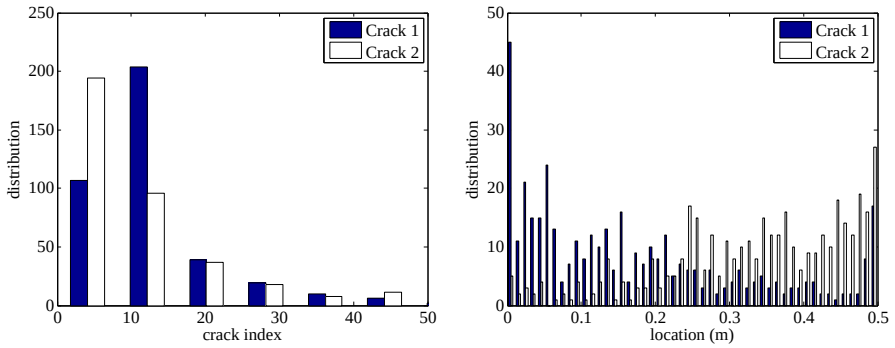

Figure E.6: The histogram of the solution for the indices and the locations of the cracks at 10% random noise.

Bibliography

A. Abbate, J. Koay, J. Frankel, S. C. Schroeder, and P. Das. Signal detection and noise suppression using a wavelet transform signal processor: application to ultrasonic flaw detection. *IEEE Transactions on Ultrasonics, Ferroelectrics, and Frequency Control*, 44(1):14–26, 1997.

J. Achenbach. *Wave propagation in elastic solids, 7th edition.* Elsevier Science Publishers B.V., Amsterdam, 1993.

R. D. Adams, P. Cawley, and C. C. H. Guyott. Non-destructive testing of adhesive joints. In *Adhesion (Barking, England)*, pages 96–112, 1986.

K. Amaratunga and R. Sudarshan. Multiresolution modeling with operator-customized wavelets derived from finite elements. *Computer Methods in Applied Mechanics and Engineering*, 195(19-22):2509–2532, 2006.

K. Amaratunga and J. R. Williams. Wavelet-galerkin solution of boundary value problems. *Archives of Computational Methods in Engineering*, 4(3):243–285, 1997.

K. Amaratunga, J. R. Williams, S. Qian, and J. Weiss. Wavelet-galerkin solutions for one-dimensional partial differential equations. *International Journal for Numerical Methods in Engineering*, 37(16):2703–2716, 1994.

G. Amdahl. Validity of the single processor approach to achieving large scale computing capabilities. In *Proceeding AFIPS '67, spring joint computer conference*, 1967.

D. Balageas, C. Fritzen, and A. Güemes. *Structural Health Monitoring.* Wiley-ISTE, London, UK, 2006.

I. Bartoli, A. Marzani, F. L. d. Scalea, and E. Viola. Modeling wave propagation in damped waveguides of arbitrary cross-section. *Journal of Sound and Vibration*, 295:685–707, 2006.

T. Belytschko and T. J. R. Hughes. *Computational Methods for Transient Analysis.* NorthHolland, Amsterdam, 1983.

A. Bergamini and F. Biondini. Finite strip modeling for optimal design of prestressed folded plate structures. *Engineering Structures*, 26(8):1043–1054, 2004.

G. Beylkin. On the representation of operators in bases of compactly supported wavelets. *SIAM Journal on Numerical Analysis*, 29(6):1716–1740, 1992.

J. Blitz and G. Simpson. *Ultrasonic methods of non-destructive testing*. Chapman and Hall, 1996.

J. G. P. Bloom, F. H. Dijkstra, and A. W. F. Volker. Model-based ultrasonic inspection technique development and evaluation. In *AIP Conference Proceedings*, volume 975, pages 1716–1723, 2008.

C. Boller. Next generation structural health monitoring and its integration into aircraft design. *International Journal of Systems Science*, 31(11):1333–1349, 2000.

C. Boller, F.-K. Chang, and Y. Fujino. *Encyclopedia of Structural Health Monitoring*. Wiley, Chichester, UK, 2009.

J. Bradley, C. Brislawn, and T. Hopper. The fbi wavelet/scalar quantization standard for gray-scale fingerprint image compression. Technical report, Los Alamos National Lab, 1993.

L. J. Breon, J. K. Van Velsor, and J. L. Rose. Guided wave damage detection tomography for structural health monitoring in critical zones of pipelines. *Materials Evaluation*, 65(12):1215–1219, 2007.

H. R. Busby and D. M. Trujillo. Optimal regularization of an inverse dynamics problem. *Computers andamp; Structures*, 63(2):243–248, 1997.

C. Canuto. *Spectral methods: evolution to complex geometries and applications to fluid dynamics*. Springer, 2007.

P. Cawley. The operation of ndt instruments based on the impedance method. *Composite Structures*, 3(3-4):215–228, 1985.

P. Cawley, M. J. S. Lowe, D. N. Alleyne, B. Pavlakovic, and P. Wilcox. Practical long range guided wave testing: Applications to pipes and rail. *Materials Evaluation*, 61(1):66–74, 2003.

A. Chakraborty and S. Gopalakrishnan. A spectrally formulated finite element for wave propagation analysis in layered composite media. *International Journal of Solids and Structures*, 41(18-19):5155–5183, 2004.

A. Chakraborty and S. Gopalakrishnan. A spectral finite element model for wave propagation analysis in laminated composite plate. *Journal of Vibration and Acoustics-Transactions of the Asme*, 128(4):477–488, 2006.

C. L. Chen and F. G. Yuan. Impact source identification in finite isotropic plates using a time-reversal method: theoretical study. *Smart Materials and Structures*, 19(10):–, 2010.

M. Q. Chen and C. Hwang. The computation of wavelet-galerkin approximation on a bounded interval. *International Journal for Numerical Methods in Engineering*, 39(17):2921–2944, 1996.

M. Q. Chen, C. Hwang, and Y. P. Shih. A wavelet-galerkin method for solving population balance equations. *Computers and Chemical Engineering*, 20(2): 131–145, 1996.

M. R. Chitnis, Y. M. Desai, and T. Kant. Wave propagation in laminated composite plates using higher order theory. *Journal of Applied Mechanics, Transactions ASME*, 68(3):503–505, 2001.

Y. H. Cho and J. L. Rose. A boundary element solution for a mode conversion study oil the edge reflection of lamb waves. *Journal of the Acoustical Society of America*, 99(4):2097–2109, 1996.

F. Ciampa and M. Meo. Impact detection in anisotropic materials using a time reversal approach. *Structural Health Monitoring*, 11(1):43–49, 2012.

R. P. Dalton, P. Cawley, and M. J. S. Lowe. The potential of guided waves for monitoring large areas of metallic aircraft fuselage structure. *Journal of Nondestructive Evaluation*, 20(1):29–46, 2001.

I. Daubechies. Orthonormal bases of compactly supported wavelets. *Communication in Pure and Applied Mathematics*, 41(7):909–996, 1988.

I. Daubechies. *Ten lectures on wavelets*. Society for Industrial and Applied Mathematics, Philadelphia, 1992.

D. J. Dawe. Use of the finite strip method in predicting the behaviour of composite laminated structures. *Composite Structures*, 57(1-4):11–36, 2002.

P. P. Delsanto, T. Whitcombe, H. H. Chaskelis, and R. B. Mignogna. Connection machine simulation of ultrasonic wave-propagation in materials .1. the one-dimensional case. *Wave Motion*, 16(1):65–80, 1992.

A. Demma, P. Cawley, M. Lowe, A. G. Roosenbrand, and B. Pavlakovic. The reflection of guided waves from notches in pipes: A guide for interpreting corrosion measurements. *NDT and E International*, 37(3):167–180, 2004.

F. L. di Scalea and J. McNamara. Ultrasonic nde of railroad tracks: air-coupled cross-sectional inspection and long-range inspection. *Insight*, 45 (6)::394–401, 2003.

F. L. di Scalea, P. Rizzo, S. Coccia, I. Bartoli, M. Fateh, E. Viola, and G. Pascale. Non-contact ultrasonic inspection of rails and signal processing for automatic defect detection and classification. *Insight: Non-Destructive Testing and Condition Monitoring*, 47(6):346–353, 2005.

S. B. Dong and R. B. Nelson. Natural vibrations and waves in laminated orthotropic plates. *Journal of Applied Mechanics*, 39(3):739–and, 1972.

J. F. Doyle. *Wave propagation in structures: an FFT-based spectral analysis methodology*. Springer-Verlag, New York, 1989.

E. Faccioli, F. Maggio, R. Paolucci, and A. Quarteroni. 2d and 3d elastic wave propagation by a pseudo-spectral domain decomposition method. *Journal of Seismology*, 1(3):237–251, 1997.

T. N. Farris and J. F. Doyle. Wave propagation in a split timoshenko beam. *Journal of Sound and Vibration*, 130(1):137–147, 1989.

Z. Feng, W. Wang, W. Tong, K. Yuan, Z. Han, and Y. Chen. Storage tank floor and wall defect in-situ inspection with ultrasonic guided wave technique. In *Proceedings of the Biennial International Pipeline Conference, IPC*, volume 3, pages 229–232, 2010.

M. Fink. Time-reversal of ultrasonic fields .1. basic principles. *Ieee Transactions on Ultrasonics Ferroelectrics and Frequency Control*, 39(5):555–566, 1992.

M. Fink. Time-reversed acoustics. *Scientific American*, 281(5)::91–97, 1999.

B. Fornberg. The pseudospectral method: comparisons with finite differences for the elastic wave equation. *Geophysics*, 52:483–501, 1987.

M. I. Friswell. Damage identification using inverse methods. *Philosophical Transactions of the Royal Society a-Mathematical Physical and Engineering Sciences*, 365(1851):393–410, 2007.

M. Fujii and W. J. R. Hoefer. Interpolating wavelet collocation method of time dependent maxwell's equations: characterization of electrically large optical waveguide discontinuities. *Journal of Computational Physics*, 186 (2)::666–689, 2003.

R. Gangadharan, D. R. Mahapatra, S. Gopalakrishnan, C. R. L. Murthy, and M. R. Bhat. On the sensitivity of elastic waves due to structural damages: Time-frequency based indexing method. *Journal of Sound and Vibration*, 320 (4-5):915–941, 2009a.

R. Gangadharan, C. R. L. Murthy, S. Gopalakrishnan, and M. R. Bhat. Time reversal technique for health monitoring of metallic structure using lamb waves. *Ultrasonics*, 49(8):696–705, 2009b.

H. Gao and J. L. Rose. Ice detection and classification on an aircraft wing with ultrasonic shear horizontal guided waves. *IEEE Transactions on Ultrasonics, Ferroelectrics, and Frequency Control*, 56(2):334–344, 2009.

L. Gaul, M. Kögl, and M. Wagner. *Boundary Element Methods for Engineers and Scientists*. Springer, Berlin, 2003.

J. Gazdag. Modeling of the acoustic wave equation with transform methods, 1981.

V. Giurgiutiu. *Structural health monitoring with piezoelectric wafer active sensors*. Academic Press an Imprint of Elsevier, Burlington, MA, 2008.

S. Gopalakrishnan and M. Mitra. *Wavelet Methods for Dynamical Problems: With Application to Metallic, Composite, and Nano-Composite Structures*. Taylor and Francis, Boca Raton, 2010.

S. Gopalakrishnan, M. Martin, and J. F. Doyle. A matrix methodology for spectral analysis of wave propagation in multiple connected timoshenko beams. *Journal of Sound and Vibration*, 158(1):11–24, 1992.

S. Gopalakrishnan, A. Chakraborty, and D. R. Mahapatra. *Spectral Finite Element Method: Wave Propagation, Diagnostics and Control in Anisotropic and Inhomogeneous Structures*. Springer-Verlag, London, England, 2008.

J. C. Goswami, A. K. Chan, and C. K. Chui. On solving first-kind integral equations using wavelets on a bounded interval. *IEEE Transactions on Antennas and propagation*, 43(6):614–622, 1995.

P. Goupillaud, A. Grossman, and J. Morlet. Cycle-octave and related transforms in seismic signal analysis. *Geoexploration*, 23:85–102, 1984.

J. Grabowska, M. Palacz, and M. Krawczuk. Damage identification by wavelet analysis. *Mechanical Systems and Signal Processing*, 22(7):1623–1635, 2008.

K. Graff. *Wave Motion in Elastic Solids*. Dover Publications, New York, 1975.

D. Gsell, T. Leutenegger, and J. Dual. Modeling three-dimensional elastic wave propagation in circular cylindrical structures using a finite-difference approach. *Journal of the Acoustical Society of America*, 116(6):3284–3293, 2004.

S. Ha and F. K. Chang. Optimizing a spectral element for modeling pzt-induced lamb wave propagation in thin plates. *Smart Materials and Structures*, 19(1): –, 2010.

S. Ha, K. Lonkar, A. Mittal, and F. K. Chang. Adhesive layer effects on pzt-induced lamb waves at elevated temperatures. *Structural Health Monitoring*, 9(3):247–256, 2010.

A. Haar. Zur theorie der orthogonalen funktionensysteme. *Mathematische Annalen*, 69:331–371, 1910.

J.-G. Han, W.-X. Ren, and Y. Huang. A spline wavelet finite-element method in structural mechanics. *International Journal for Numerical Methods in Engineering*, 66(1):166–190, 2006.

A. Harten. Adaptive multiresolution schemes for shock computations. *Journal of Computational Physics*, 115(2):319–338, 1994.

T. Hayashi, C. Tamayama, and M. Murase. Wave structure analysis of guided waves in a bar with an arbitrary cross-section. *Ultrasonics*, 44(1):17–24, 2006.

T. K. Hong and B. L. N. Kennett. On a wavelet-based method for the numerical simulation of wave propagation. *Journal of Computational Physics*, 183(2): 577–622, 2002a.

T. K. Hong and B. L. N. Kennett. A wavelet-based method for simulation of two-dimensional elastic wave propagation. *Geophysical Journal International*, 150(3):610–638, 2002b.

T. J. R. Hughes. *The Finite Element Method: Linear Static and Dynamic Finite Element Analysis*. Prentice Hall, Englewood Cliffs, NJ, 1987.

T. J. R. Hughes, A. Reali, and G. Sangalli. Duality and unified analysis of discrete approximations in structural dynamics and wave propagation: Comparison of p-method finite elements with k-method nurbs. *Computer Methods in Applied Mechanics and Engineering*, 197(49-50):4104–4124, 2008.

D. J. Inman, C. R. Farrar, V. L. Junior, and V. S. Junior. *Damage Prognosis: For Aerospace, Civil and Mechanical Systems*. Wiley, New York, 2004.

H. Inoue, J. J. Harrigan, and S. R. Reid. Review of inverse analysis for indirect measurement of impact force. *Applied Mechanics Reviews*, 54(6):503–524, 2001.

Y. Jiangong, W. Bin, H. Hongli, and H. Cunfu. Characteristics of guided waves in anisotropic spherical curved plates. *Wave Motion*, 44(4):271–281, 2007.

M. Karumpholz and L. P. B. Katehi. Mrtd: new time-domain schemes based on multiresolution analysis. *IEEE Trans. Microwave Theory Tech.*, 44(4): 555–571, 1996.

Y. Kim and F. K. Chang. Computational tool for the design of structures with built-in piezoelectric-based sensor networks. In *Proceedings of SPIE - The International Society for Optical Engineering*, volume 5765, pages 1–18, 2005.

Y. Kim, S. Ha, and F. K. Chang. Time-domain spectral element method for built-in piezoelectric-actuator- induced lamb wave propagation analysis. *AIAA Journal*, 46(3):591–600, 2008.

J. Ko, A. Kurdila, and M. Pilant. A class of finite element methods based on orthonormal, compactly supported wavelets. *Computational Mechanics*, 16: 235–244, 1995.

D. Komatitsch and J. Tromp. Introduction to the spectral element method for three-dimensional seismic wave propagation. *Geophysical Journal International*, 139(3):806–822, 1999.

D. Komatitsch and J. Tromp. Spectral-element simulations of global seismic wave propagation - i. validation. *Geophysical Journal International*, 149(2): 390–412, 2002a.

D. Komatitsch and J. Tromp. Spectral-element simulations of global seismic wave propagation - ii. three-dimensional models, oceans, rotation and self-gravitation. *Geophysical Journal International*, 150(1):303–318, 2002b.

D. Komatitsch and J. P. Vilotte. The spectral element method: An efficient tool to simulate the seismic response of 2d and 3d geological structures. *Bulletin of the Seismological Society of America*, 88(2):368–392, 1998.

D. Komatitsch, C. Barnes, and J. Tromp. Simulation of anisotropic wave propagation based upon a spectral element method. *Geophysics*, 65(4):1251–1260, 2000.

M. Koshiba, S. Karakida, and M. Suzuki. Finite element analysis of lamb waves scattering in an elastic plate waveguide. *IEEE Transactions in Sonics and Ultrasonics*, 31:18–25, 1984.

M. Krawczuk. Application of spectral beam finite element with a crack and iterative search technique for damage detection. *Finite Elements in Analysis and Design*, 38(6):537–548, 2002.

M. Krawczuk, M. Palacz, and W. Ostachowicz. The dynamic analysis of a cracked timoshenko beam by the spectral element method. *Journal of Sound and Vibration*, 264(5):1139–1153, 2003.

M. Krawczuk, J. Grabowska, and M. Palacz. Longitudinal wave propagation. part i–comparison of rod theories. *Journal of Sound and Vibration*, 295(3-5): 461–478, 2006.

P. Kudela, A. Zak, M. Krawczuk, and W. Ostachowicz. Modelling of wave propagation in composite plates using the time domain spectral element method. *Journal of Sound and Vibration*, 302(4-5):728–745, 2007.

T. Kundu. *Ultrasonic nondestructive evaluation: engineering and biological material characterization*. CRC Press, 2004.

A. Latto, H. L. Resnikoff, and E. Tenenbaum. The evaluation of connection coefficients of compactly supported wavelets. In *Proceedings of the French-USA Workshop on Wavelets and Turbulence*, Princeton, 1991.

V. M. N. Ledesma, E. P. Baruch, A. Demma, and M. J. S. Lowe. Guided wave testing of an immersed gas pipeline. *Materials Evaluation*, 67(2):102–115, 2009.

B. C. Lee and W. J. Staszewski. Lamb wave propagation modelling for damage detection: I. two-dimensional analysis. *Smart Materials and Structures*, 16 (2):249–259, 2007.

R. Levine, J. Michaels, and S. Lee. Boundary reflection compensation in guided wave baseline-free imaging. volume 1335, pages 113–120, 2011.

J. X. Ma, J. J. Xue, S. J. Yang, and Z. J. He. A study of the construction and application of a daubechies wavelet-based beam element. *Finite Elements in Analysis and Design*, 39 (10)::965–975, 2003.

D. R. Mahapatra and S. Gopalakrishnan. A spectral finite element model for analysis of axial-flexural-shear coupled wave propagation in laminated composite beams. *Composite Structures*, 59(1):67–88, 2003.

D. R. Mahapatra and S. Gopalakrishnan. Spectral finite element analysis of coupled wave propagation in composite beams with multiple delaminations and strip inclusions. *International Journal of Solids and Structures*, 41 (5-6):: 1173–1208, 2004.

D. R. Mahapatra, S. Gopalakrishnan, and T. S. Sankar. Spectral-element-based solutions for wave propagation analysis of multiply connected unsymmetric laminated composite beams. *Journal of Sound and Vibration*, 237(5):819–836, 2000.

D. R. Mahapatra, A. Singhal, and S. Gopalakrishnan. A higher-order finite waveguide model for spectral analysis of composite structures. *Computer Methods in Applied Mechanics and Engineering*, 195(9-12):1116–1135, 2006.

S. Mallat. A theory for multiresolution signal decomposition: The wavelet representation. *IEEE Transactions on PAMI*, 11(7):674–693, 1989.

A. Marzani, E. Viola, I. Bartoli, F. L. di Scalea, and P. Rizzo. A semi-analytical finite element formulation for modeling stress wave propagation in axisymmetric damped waveguides. *Journal of Sound and Vibration*, 318 (3)::488–505, 2008.

J. McNamara and F. Lanza di Scalea. Advances in health monitoring of railroad tracks. In *Proceedings of SPIE - The International Society for Optical Engineering*, volume 4702, pages 250–261, 2002.

M. Melo Mota. Experimental evaluation of a structural health monitoring methodology. Master's thesis, 2011.

Y. Meyer. Wavelets: Algorithms and applications, philadelphia. *Society for Industrial and Applied Mathematics*, pages 13–31, 1993.

M. Mitra and S. Gopalakrishnan. Spectrally formulated wavelet finite element for wave propagation and impact force identification in connected 1-d waveguides. *International Journal of Solids and Structures*, 42(16-17):4695–4721, 2005.

M. Mitra and S. Gopalakrishnan. Extraction of wave characteristics from wavelet-based spectral finite element formulation. *Mechanical Systems and Signal Processing*, 20(8):2046–2079, 2006a.

M. Mitra and S. Gopalakrishnan. Wavelet based spectral finite element for analysis of coupled wave propagation in higher order composite beams. *Composite Structures*, 73(3):263–277, 2006b.

M. Mitra and S. Gopalakrishnan. Wavelet based spectral finite element modelling and detection of de-lamination in composite beams. *Proceedings of the Royal Society A: Mathematical, Physical and Engineering Sciences*, 462 (2070):1721–1740, 2006c.

M. Mitra and S. Gopalakrishnan. Wavelet based 2-d spectral finite element formulation for wave propagation analysis in isotropic plates. *CMES - Computer Modeling in Engineering and Sciences*, 15(1):49–67, 2006d.

M. Mitra and S. Gopalakrishnan. Wavelet spectral element for wave propagation studies in pressure loaded axisymmetric cylinders. *Journal of Mechanics of Materials and Structures*, 2(4):753–772, 2007.

M. Mitra and S. Gopalakrishnan. Wave propagation analysis in anisotropic plate using wavelet spectral element approach. *Journal of Applied Mechanics, Transactions ASME*, 75(1):0145041–0145046, 2008.

J. Moll, R. T. Schulte, B. Hartmann, C. P. Fritzen, and O. Nelles. Multi-site damage localization in anisotropic plate-like structures using an active guided wave structural health monitoring system. *Smart Materials and Structures*, 19(4), 2010.

M. Mota, L. Pahlavan, and C. Kassapoglou. Experimental evaluation of a wavelet-based fem and its application to load history identification., 2011.

W. B. Na and T. Kundu. Underwater pipeline inspection using guided waves. *Journal of Pressure Vessel Technology, Transactions of the ASME*, 124(2): 196–200, 2002.

K. S. Nadella and C. E. S. Cesnik. Local interaction simulation of guided-wave propagation in composite plates. In *Proceedings of SPIE - The International Society for Optical Engineering*, volume 7984, 2011.

A. Nag, D. R. Mahapatra, S. Gopalakrishnan, and T. S. Sankar. A spectral finite element with embedded delamination for modeling of wave scattering in composite beams. *Composites Science and Technology*, 63 (15)::2187–2200, 2003.

A. H. Nayfeh. The general problem of elastic wave propagation in multilayered anisotropic media. *Journal of the Acoustical Society of America*, 89(4 I): 1521–1531, 1991.

A. H. Nayfeh and D. E. Chimenti. Free wave propagation in plates of general anisotropic media. *Journal of Applied Mechanics-Transactions of the Asme*, 56(4):881–886, 1989.

R. B. Nelson, S. B. Dong, and R. D. Kalra. Vibrations and waves in laminated orthotropic circular cylinders. *Journal of Sound and Vibration*, 18(3):429–and, 1971.

J. Oden and J. Reddy. *A Mathematical Theory of Finite Elements*. John Wiley and Sons, New York, 1976.

W. M. Ostachowicz. Damage detection of structures using spectral finite element method. *Computers and Structures*, 86(3-5):454–462, 2008.

L. Pahlavan. Wave propagation in composite cylindrical shells. In *Fourteenth Engineering Mechanics Symposium*, Lunteren, The Netherlands, 2011.

L. Pahlavan, C. Kassapoglou, and G. Z. Wavelet-based finite element method for modeling wave propagation in composite rings. In *The 5th European Workshop on Structural Health Monitoring*, Naples, Italy, 2010.

L. Pahlavan, C. Kassapoglou, and G. Z. A wavelet-based spectral finite element method for simulating elastic wave propagation. In *The 8th International Workshop on SHM*, Stanford, CA, 2011.

L. Pahlavan, C. Kassapoglou, A. Suiker, and G. Z. A 2d wavelet-based spectral finite element method for elastic wave propagation. *Philosophical Magazine*, 92:28-30:3699–3722, 2012a.

L. Pahlavan, C. Kassapoglou, and G. Z. Spectral formulation of finite element methods using daubechies compactly-supported wavelets for elastic wave propagation problems. *Wave Motion*, accepted for publication, 2012b.

M. Palacz and M. Krawczuk. Analysis of longitudinal wave propagation in a cracked rod by the spectral element method. *Computers and Structures*, 80 (24):1809–1816, 2002.

M. Palacz, M. Krawczuk, and W. Ostachowicz. The spectral finite element model for analysis of flexural-shear coupled wave propagation.: Part 1: Laminated multilayer composite beam. *Composite Structures*, 68(1):37–44, 2005a.

M. Palacz, M. Krawczuk, and W. Ostachowicz. The spectral finite element model for analysis of flexural-shear coupled wave propagation. part 2: Delaminated multilayer composite beam. *Composite Structures*, 68(1):45–51, 2005b.

E. Pan, J. Rogers, S. K. Datta, and A. H. Shah. Mode selection of guided waves for ultrasonic inspection of gas pipelines with thick coating. *Mechanics of Materials*, 31(3):165–174, 1999.

A. T. Patera. A spectral element method for fluid dynamics: Laminar flow in a channel expansion. *Journal of Computational Physics*, 54(3):468–488, 1984.

R. D. Patton and P. C. Marks. One-dimensional finite elements based on the daubechies family of wavelets. *Aiaa Journal*, 34(8):1696–1698, 1996.

H. K. Peng, G. Meng, and F. C. Li. Modeling of wave propagation in plate structures using three-dimensional spectral element method for damage detection. *Journal of Sound and Vibration*, 320(4-5):942–954, 2009.

E. Priolo, J. M. Carcione, and G. Seriani. Numerical simulation of interface waves by high-order spectral modeling techniques. *Journal of the Acoustical Society of America*, 95(2):681–693, 1994.

P. Puthillath and J. L. Rose. Ultrasonic guided wave inspection of a titanium repair patch bonded to an aluminum aircraft skin. *International Journal of Adhesion and Adhesives*, 30(7):566–573, 2010.

S. Qian and J. Weiss. Wavelets and the numerical solution of partial differential equations. *Journal of Computational Physics*, 106:155–175, 1993.

N. Rattanawangcharoen, A. H. Shah, and S. K. Datta. Wave-propagation in laminated composite circular-cylinders. *International Journal of Solids and Structures*, 29(6):767–781, 1992.

J. N. Reddy. *Mechanics of Laminated Composite Plates*. CRC, USA, 2nd edition, 1997.

J. N. Reddy. *An Introduction to the Finite Element Method*. McGraw-Hill, New York, 3rd edition, 2005.

J. N. Reddy. *Theory and analysis of elastic plates and shells*. CRC, Boca Raton, Fla., 2nd edition, 2007.

S. A. Rizzi and J. F. Doyle. A spectral element approach to wave motion in layered solids. *Journal of Vibration and Acoustics-Transactions of the Asme*, 114(4):569–577, 1992.

P. Rizzo and F. L. di Scalea. Feature extraction for defect detection in strands by guided ultrasonic waves. *Structural Health Monitoring-an International Journal*, 5 (3)::297–308, 2006a.

P. Rizzo and F. L. di Scalea. Wavelet-based feature extraction for automatic defect classification in strands by ultrasonic structural monitoring. *Smart Structures and Systems*, 2 (3)::253–274, 2006b.

P. Rizzo, I. Bartoli, A. Marzani, and F. L. di Scalea. Defect classification in pipes by neural networks using multiple guided ultrasonic wave features extracted after wavelet processing. *Journal of Pressure Vessel Technology-Transactions of the Asme*, 127 (3)::294–303, 2005.

J. L. Rose and L. E. Soley. Ultrasonic guided waves for anomaly detection in aircraft components. *Materials Evaluation*, 58(9):1080–1086, 2000.

J. L. Rose, K. M. Rajana, and F. T. Carr. Ultrasonic guided wave inspection concepts for steam generator tubing. *Materials Evaluation*, 52(2):307–311, 1994.

J. L. Rose, M. J. Avioli, and W. J. Song. Application and potential of guided wave rail inspection. *Insight: Non-Destructive Testing and Condition Monitoring*, 44(6):353–358, 2002.

S. Salamone, I. Bartoli, F. Lanza Di Scalea, and S. Coccia. Guided-wave health monitoring of aircraft composite panels under changing temperature. *Journal of Intelligent Material Systems and Structures*, 20(9):1079–1090, 2009.

M. D. Seale, B. T. Smith, and W. H. Prosser. Lamb wave assessment of fatigue and thermal damage in composites. *Journal of the Acoustical Society of America*, 103(5):2416–2424, 1998.

G. Seriani. 3-d large-scale wave propagation modeling by spectral element method on cray t3e multiprocessor. *Computer Methods in Applied Mechanics and Engineering*, 164(1-2):235–247, 1998.

G. Seriani and S. P. Oliveira. Dispersion analysis of spectral element methods for elastic wave propagation. *Wave Motion*, 45(6):729–744, 2008.

G. Seriani and E. Priolo. Spectral element method for acoustic wave simulation in heterogeneous media. *Finite Elements in Analysis and Design*, 16(3-4): 337–348, 1994.

R. Seydel and F. K. Chang. Impact identification of stiffened composite panels: I. system development. *Smart Materials and Structures*, 10(2):354–369, 2001.

M. H. S. Siqueira, C. E. N. Gatts, R. R. Da Silva, and J. M. A. Rebello. The use of ultrasonic guided waves and wavelets analysis in pipe inspection. *Ultrasonics*, 41(10):785–797, 2004.

H. Sohn. Effects of environmental and operational variability on structural health monitoring. *Philosophical Transactions of the Royal Society A-Mathematical Physical and Engineering Sciences*, 365(1851):539–560, 2007.

W. Staszewski, C. Boller, and G. Tomlinson. *Health Monitoring of Aerospace Structures*. Wiley, West Sussex, England, 2004.

G. Strang. *Computational Science and Engineering*. Wellesley-Cambridge, Wellesley, MA, 2007.

Z. Su and L. Ye. *Identification of Damage Using Lamb Waves*. Springer-Verlag, Berlin Heidelberg, Germany, 2009.

R. Sudarshan, K. Amaratunga, and T. Grätsch. A combined approach for goal-oriented error estimation and adaptivity using operator-customized finite element wavelets. *International Journal for Numerical Methods in Engineering*, 66(6):1002–1035, 2006.

A. S. J. Suiker, A. V. Metrikine, and R. de Borst. Comparison of wave propagation characteristics of the cosserat continuum model and corresponding discrete lattice models. *International Journal of Solids and Structures*, 38(9): 1563–1583, 2001.

J. Summerscales. *Non-destructive testing of fibre-reinforced plastics composites*. Elsevier Applied Science, 1990.

T. Uhl. The inverse identification problem and its technical application. *Archive of Applied Mechanics*, 77(5):325–337, 2007.

I. A. Viktorov. *Rayleigh and Lamb Waves: Physical Theory and Applications*. Plenum Press, New York, 1967.

J. Virieux. P- sv wave propagation in heterogeneous media: velocity- stress finite-difference method. *Geophysics*, 51(4):889–901, 1986.

A. Volker and J. Bloom. Guided wave travel time tomography for bends. In *AIP Conference Proceedings*, volume 1335, pages 223–230, 2011.

C. Y. Wang and J. D. Achenbach. 2-d time-domain bem for scattering of elastic-waves in anisotropic solids. *Boundary Element Technology Ix*, pages 157–163, 1994.

L. Wang and F. G. Yua. Lamb wave propagation in composite laminates using a higher-order plate theory, 2007.

L. Wang and F. G. Yuan. Group velocity and characteristic wave curves of lamb waves in composites: Modeling and experiments. *Composites Science and Technology*, 67(7-8):1370–1384, 2007.

Q. Wang and S. F. Yuan. Baseline-free imaging method based on new pzt sensor arrangements. *Journal of Intelligent Material Systems and Structures*, 20(14): 1663–1673, 2009.

J. M. Whitney and C. T. Sun. Higher-order theory for extensional motion of laminated composites. *Journal of Sound and Vibration*, 30(1):85–97, 1973.

P. Wilcox, M. Evans, B. Pavlakovic, D. Alleyne, K. Vine, P. Cawley, and M. Lowe. Guided wave testing of rail. *Insight: Non-Destructive Testing and Condition Monitoring*, 45(6):413–420, 2003.

J. R. Williams and K. Amaratunga. A discrete wavelet transform without edge effects using wavelet extrapolation. *Journal of Fourier Analysis and Applications*, 3(4):435–449, 1997.

B. L. Xu and V. Giurgiutiu. Single mode tuning effects on lamb wave time reversal with piezoelectric wafer active sensors for structural health monitoring. *Journal of Nondestructive Evaluation*, 26(2-4):123–134, 2007.

F. G. Yuan and C. C. Hsieh. Three-dimensional wave propagation in composite cylindrical shells. *Composite Structures*, 42(2):153–167, 1998.

L. Zhang, R. Tezaur, and C. Farhat. The discontinuous enrichment method for elastic wave propagation in the medium-frequency regime. *International Journal for Numerical Methods in Engineering*, 66(13):2086–2114, 2006.

O. Zienkiewicz and Y. Cheung. *The Finite Element Method in Structural and Continuum Mechanics*. McGraw-Hill, London, 1967.

G. Zweig, R. Lipes, and J. R. Pierce. The cochlear compromise. *Journal of Acoustical Society of America*, 59(4):975–982, 1976.